Deriving the Thermophysical Properties of Planetary Surfaces Using Off-Axis Thermal Emission Spectroscopy

by

Benjamin E. McKeeby

Bachelor of Science, Stony Brook University, 2014

Master of Art, Wesleyan University, 2017

Submitted to the Graduate Faculty of the

Dietrich School of Arts and Sciences in partial fulfillment

of the requirements for the degree of

Doctor of Philosophy

University of Pittsburgh

2022

UNIVERSITY OF PITTSBURGH

DIETRICH SCHOOL OF ARTS AND SCIENCES

This dissertation was presented

by

Benjamin E. McKeeby

It was defended on

July 19, 2022

and approved by

Michael S. Ramsey, Professor, Geology and Environmental Science

William Harbert, Professor, Geology and Environmental Science

Eitan Shelef, Assistant Professor, Geology and Environmental Science

Daniel Bain, Associate Professor, Geology and Environmental Science

Victoria Hamilton, Institute Scientist, Southwest Research Institute

Dissertation Director: Michael S. Ramsey, Professor, Geology and Environmental Science

Deriving the Thermophysical Properties of Planetary Surfaces Using Off-Axis Thermal Infrared Spectroscopy

Benjamin Edward McKeeby, PhD

University of Pittsburgh, 2022

Thermal mixing below the spatial resolution of thermal infrared (TIR) instruments can produce negatively sloped emissivity spectra at longer wavelengths that may inhibit accurate compositional analysis. Sloped spectra result either from an incorrect assumption of a uniform pixel integrated surface temperature or a maximum emissivity during the temperature-emissivity separation of radiance data. Where viewed at high solar incident angles or emission angles, rough surfaces and those containing mixtures of surface units (e.g., rock and sand, rock and dust) below the pixel resolution of the instrument display varied amounts of sub-pixel anisothermality due to the viewing geometry and may result in sloped emission spectra. Under these conditions, spectral slopes are distinct, with magnitudes proportional to the degree of anisothermality. Combining TIR spectral analysis with a thermophysical model allows the simulation of emissivity spectral slopes and a derivation of the surface's anisothermal properties.

This research utilizes hyperspectral TIR spectroscopy and high-definition 3D photogrammetry to explore the effects of micro and macro surface roughness on the TIR spectrum. Micron-scale roughness results in a reduction in spectral contrast due to multiple surface reflections by emitted radiant energy. Micron-scale surface roughness does not result in negative spectral slopes. However, rough surfaces are also prone to differential heating due to shelf shadowing. Where this is the case, anisothermality manifests at the sub-pixel scale, and spectral

slopes can develop. With the combination of hyperspectral emission spectroscopy with statistics-based surface topographic analysis, I investigate these two thermophysical effects in natural basaltic surfaces at viewing conditions analogous to the Thermal Emission Imaging Spectrometer (THEMIS) routine off-nadir targeted observations (ROTO).

ROTO data from the THEMIS instrument on board Mars Odyssey are used to validate prior surface roughness modeling that previously employed nadir-only THEMIS data. Two regions within Apollinaris Mons and two regions within Arsia Mons are studied using THEMIS ROTO data acquired at or just after local sunset. Spectral slope and brightness temperature modeling using the KRC thermal model predicts the lateral distribution of rock and dust and the vertical thickness of dust layering. Ultimately, this method allows for particle size, rock abundance, and dust mantling determinations. Additionally, it may assist with the separability of spectral signatures necessary to perform a rigorous compositional analysis of lava flows within the Daedalia Planum flow field.

Table of Contents

List of Tables

List of Figures

Acknowledgements

First and foremost, I wish to express my sincerest gratitude and appreciation to my advisor Mike Ramsey. His guidance, depth of knowledge, attention to detail, and mentoring have been invaluable to me as I have progressed as a student, researcher, and geologist. I also want to thank my committee members Vicky Hamilton, Bill Harbert, Eitan Shelef, and Dan Bain, whose time and efforts have provided direction and insightful advice. Other invaluable assistance and insights have been provided by Christopher Edwards and Christian Tai Udovicic at NAU, Deanne Rogers at Stony Brook University, Jonathan Hill at ASU, and my office and lab mates Ian Flynn, Daniel Williams, and James Thompson. I would also like to recognize and thank my family, whose unwavering support, love, and guidance have shaped me into the person, professional, and researcher I am today. To my partner Diana, you've been my rock these last four years, keeping me grounded and focused. I can't thank you enough for all the encouragement, support, and love you have shown. To the Tsoy family, Elina and Sergey, thank you for being my second home and all your love and encouragement.

I would also like to acknowledge the pioneering work of the late Josh Bandfield on the THEMIS calibration and modeling of surface roughness on Mars that laid much of the basis for the research presented here. Lastly, this research was supported through continuing funding of an original Mars Odyssey Participating Scientist Program project.

1.0 Preface

How is a planet formed? What processes are present on its surface? Is there water? Volcanos? Life? These are just a few questions we ask, and planetary scientists look to answer. Optical remote sensing provides the ability for remote detection and characterization of planetary surfaces in a non-destructive manner. It is more efficient than in-situ exploration, offers repeat coverage for temporal datasets, and can prove effective in hard-to-reach locations. However, successfully assessing a planetary surface's features is restricted by the spatial resolution of the instrument employed. Perhaps the most famous example is Giovanni Schiaparelli and his Martian "Canali." We, as planetary scientists, must strive to improve our methods, whether through more advanced instrumentation or the development of better models and techniques.

Understanding the surface at the sub-pixel scales is essential for understanding a number of geologic processes such as dust deposition and mantling, volcanic eruptive conditions, rock abundance, and the mixing of geologic materials (Christensen, 1982; Mushkin and Gillespie, 2005; Bandfield and Edwards, 2008; Bandfield, 2009). The variation in surface characteristics commonly occurs at spatial scales smaller than those available from orbital instrumentation, which typically ranges from meters to hundreds of meters. Techniques have been developed to derive such surface characteristics, including temperature measurements and spectral analysis from instruments like the Thermal Emission Spectrometer (TES) and Thermal Emission Imaging System (THEMIS). For Martian science, studies of this nature aid in the geologic interpretation of a planetary surface and assist in the selection of future landing sites.

Cumulatively, my work investigates the effects of a surface's thermophysical properties on its TIR emission spectrum and uses that knowledge to derive surface characteristics. In doing so, I look to answer fundamental questions about surface processes and landscape evolution on Mars today, such as the role aeolian transport has played. Chapter 2 provides an in-depth examination of the spectroscopic theory concerning the thermal infrared spectrum. This chapter covers the fundamental absorption features commonly examined in geologic studies and particle size and surface roughness effects. It then discusses the relationship between radiance, temperature, and thermal inertia and describes the impact of particle size mixing below an instrument's spatial resolution. Finally, chapter 2 discusses the use of ROTOs acquired by the THEMIS instrument and made possible by the off-axis rotation of the Mars Odyssey spacecraft. ROTOs will be addressed extensively throughout the remaining chapters of this dissertation.

Chapter 3 documents a laboratory study that examines the effects of micron-scale surface roughness on hyperspectral TIR emission data. This work utilizes several basaltic samples of varying morphology; collected during field campaigns in Mauna Ula, Hawaii. TIR emission spectra measured at nadir and off-nadir emission angles examine the changes in spectral features due to surface roughness and directional heating. Photogrammetry and rigorous statistical analysis of the sample's topography document variations in micron-scale surface features. This work allows for a quantification of micron-scale surface roughness and the associated spectral effects. Furthermore, it demonstrates the applicability of consumer-grade off-the-shelf hardware and open-source software to perform rigorous fine-scale surface analysis.

Chapters 4 and 5 deal with orbital data collected from the THEMIS ROTO campaigns. Chapter 4 details a new set of eight observations collected over Apollinaris Mons in March 2020.

Two study sites are examined to determine the effects of a changing emission angle on THEMIS brightness temperature and emissivity. TIR emission spectroscopy and the KRC thermophysical model (Kieffer, 2013) are combined to characterize the horizontal mixing of thermally distinct surface units at each ROTO viewing geometry. Changing the surface's emission angle relative to the spacecraft provides a novel approach to deriving the surface's thermophysical properties and improves the sensitivity of rock abundance approximations. Lastly, chapter 5 applies the methods outlined previously (chapter 4) to investigate lava outcropping and dust mantling on two basaltic lava flows in Arsia Mons. Using a 2017 ROTO dataset paired with the KRC thermophysical model (Kieffer, 2013), horizontal and vertical mixing of dust, lava outcrop, and sand is investigated and quantified. Furthermore, TIR spectral modeling demonstrates that the spectral signature of basalt is present in regions with observable lava outcrops and minimal dust mantling. The separation of dust and rock spectral components suggests the possibility for future compositional work on these lava flows, which were previously considered too dust-covered.

This work aims to understand how the surface roughness of natural samples impacts TIR emission spectra. It also looks to quantify the effects of thermally mixed pixels composed of various particle sizes and thermal inertias on nadir and off-nadir emission spectra by combining thermophysical and spectral modeling to derive the percentage of distinct sub-pixel surface units. The research presented here provides a novel approach combining planetary remote sensing and thermophysical modeling to improve our knowledge of planetary surfaces.

2.0 Theory and Background

2.1 Introduction

Infrared spectroscopic data acquired by remote sensing are essential to support planetary exploration. These investigations are vital in determining surface composition, temperature, and thermophysical properties. The physical properties of sediments (e.g., their particle size, sorting, and induration) and of rocks (e.g., their porosity, cementation, vesicularity) reflect the evolution of the surface and the processes that formed them (Christensen, 1986; Smith et al., 1999; Carr, 2007; Grotzinger, 2009, Grotzinger, 2011). Providing constraints to these processes is therefore essential to understand the geologic history. TIR reflectance and emittance spectroscopy provide helpful information about planetary surfaces for geologic study (Schueler and Silverman, 1997; Hamilton, 2010; Bishop et al., 2019). As aptly named, TIR emittance spectroscopy measures the radiant energy emitted from an object and compares it to that of a perfect emitter (blackbody) at the same temperature.

The purpose of this chapter is to present the theoretical and foundational background needed for the subsequent chapters. Part 1 briefly discusses the absorption signatures central to the identification of mineralogy. Following, part 2 is a focused discussion on radiative transfer theory as it pertains to particle size and roughness, optical constants, thermal inertia, and emissivity. Part 3 discusses the thermal behavior of a surface where temperature mixing occurs below the pixel resolution of TIR instruments and the subsequent effects on spectral emissivity and brightness temperature. Finally, part 4 summarizes the ROTO campaign, including the novel nature of ROTO viewing geometry and a brief discussion of the various imaging and spectral instruments used in this study.

2.2 Radiance, Temperature, and Thermal Inertia

TIR emission spectroscopy measures a surface's spectral radiance (watts per unit area). Spectral radiance is the radiant energy emitted from an object in a given direction over a specific angle, time interval, unit surface area, and wavelength range (Howell and Siegel, 1971). The Planck equation defines this:

$$B_{\lambda}(\tau) = \frac{2hc^2/\lambda^5}{e^{hc/\lambda k\tau} - 1}$$

Equation 1

Where B is spectral radiance at a specific wavelength (λ) and as a function of temperature (t), k is the Stefan-Boltzman constant ($5.67 \times 10^{-8}\ W \cdot m^{-2} \cdot K^{-4}$), h is the Planck constant ($6.62607015 \times 10^{-34}\ kg \cdot m^2 \cdot s^{-2}$), and c is the speed of light (3.00×10^8 m/s). Radiance is specific to an object's temperature; for instance, a mineral at a defined temperature will emit a different radiance than that at a different temperature. Therefore, the temperature effects must be removed to compare the radiance of two objects at different temperatures. Temperature-emissivity separation is achieved by dividing the emitted radiance by that of a blackbody at the same temperature and wavelength and under the same viewing conditions. A blackbody is an object or surface acting as a perfect emitter at all wavelengths as defined by the Planck equation and therefore has an emissivity (ε) of unity (Figure 1).

Temperature estimates are made from the radiance data using the Stefan-Boltzman equation if the object is assumed to be a blackbody radiator. The Stefan-Boltzman equation is defined as:

$$P=\varepsilon\sigma AT^4 \qquad \textbf{Equation 2}$$

Where P is the power radiated (Watts), ε is emissivity, σ is the Stefan-Boltzman constant (5.67×10^{-8} $W\cdot m^{-2}\cdot K^{-4}$), A is surface area ($m^2$), and T is the temperature (K). Brightness temperature (BT) is the temperature of a blackbody that emits an identical amount of radiance as the object in question at a specific wavelength (λ) or in a spectral band. The surface temperature obtained from TIR observations of real materials is a function of the component mixture of the different surface units within the instrument's field of view (FOV). Commonly, this may constitute several materials of varying compositions, particle sizes, and slope facets. Due to the relationship between spectral radiance, emissivity, and temperature, TIR investigations are ideal for these analyses. The TIR spectrum is sensitive to an object's composition, temperature, and thermophysical properties. Where combined with a thermal model, the thermophysical properties of the surface can be extracted from the radiance data.

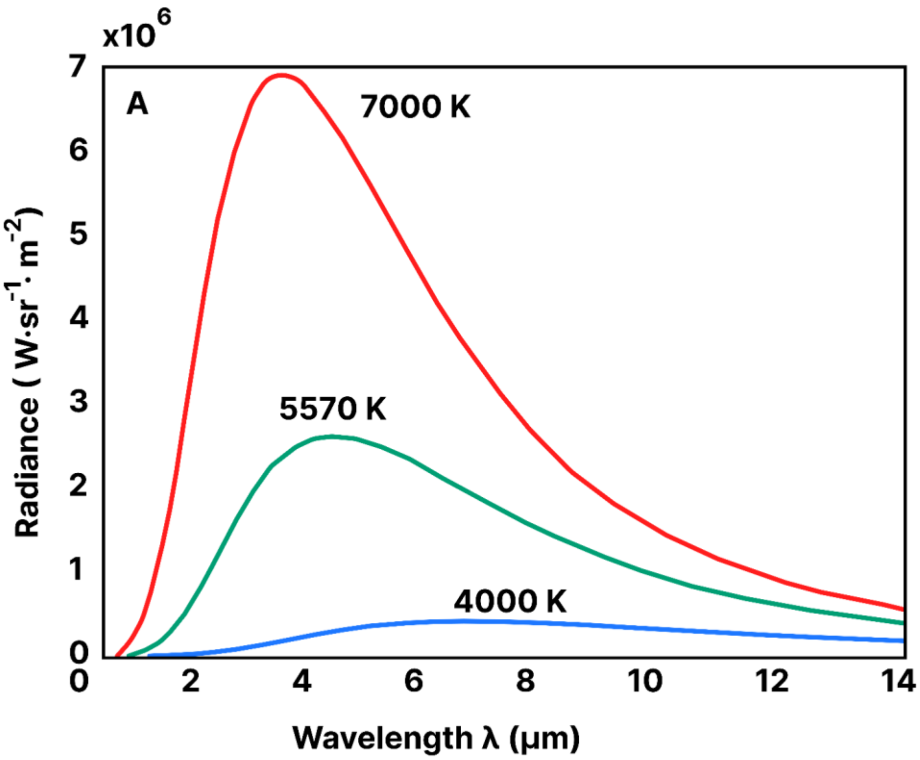

Figure 1. A) Blackbody spectra at various temperatures.

2.2.1 Emissivity and Temperature

Planetary surfaces radiate energy proportional to their temperature and emissivity. This is known as Kirchoff's law of thermal radiation. The Planck equation describes the emitted energy from a surface, and perfectly emitting surfaces are absent of wavelength-dependent absorptions. However, most natural surfaces exhibit distinct absorptions at wavelengths specific to the vibrational frequencies of their chemical bonds (Figure 2). This property, known as emissivity, is intrinsic and defined as the ratio of emitted energy from a sample to that of a blackbody at an identical temperature. Unlike emissivity, temperature is not inherent to the surface. Instead, it is controlled by the thermal inertia, roughness, and incident solar radiation that a planetary surface receives and reemits. The composition of the surface determines the shape of the thermal infrared (TIR) emissivity spectrum emitted from it, as a function of wavelength, but also viewing geometry and surface roughness. Surface temperatures are independent of emissivity and can be recovered from a single band of radiance data if corrections for the atmosphere are made and emissivity is known.

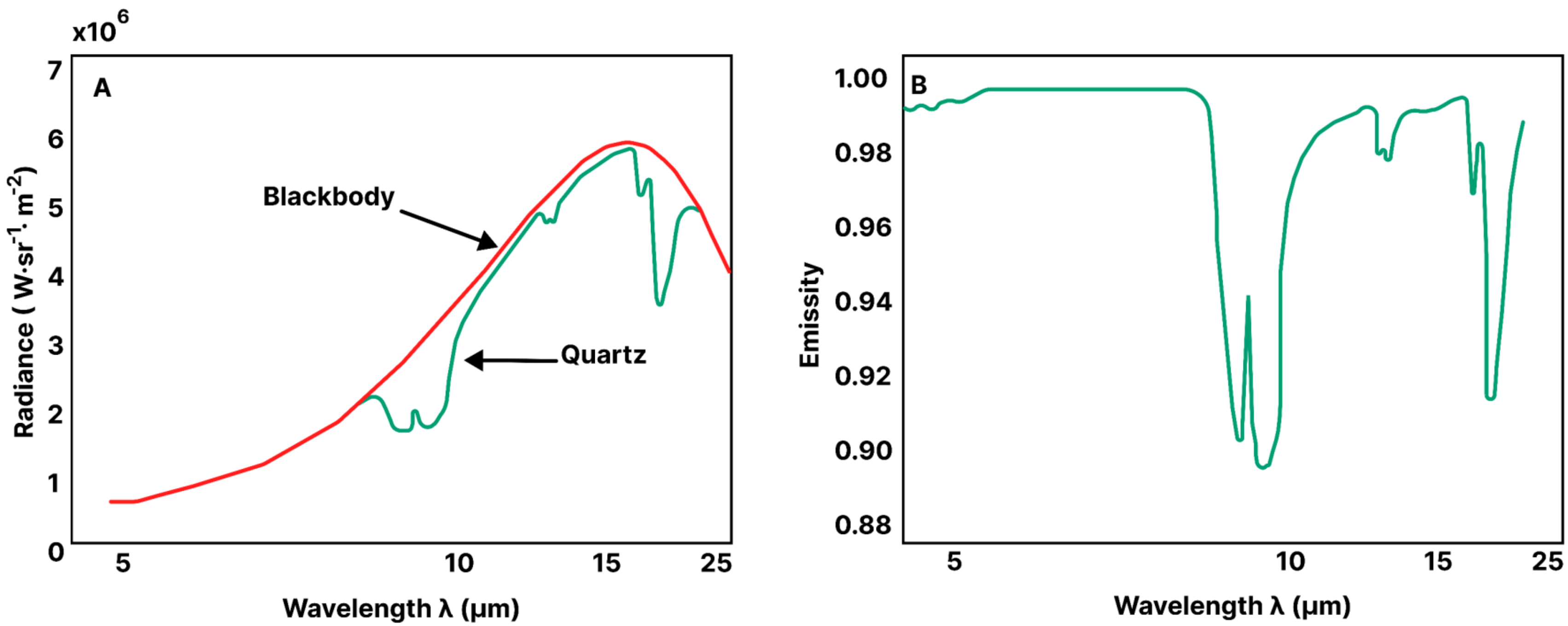

Figure 2. A) Radiance spectra of quartz and a blackbody at the same temperature. B) Quartz emission spectrum.

2.2.2 Thermal Inertia

Thermal inertia (TI) describes an object's response to temperature change by way of storing and losing heat and is controlled by the material's physical properties. Expressed in J m^{-2} K^{-1} $s^{-1/2}$ or Thermal Inertia Units (TIU), TI is defined as a composite surface property equal to the square root of the product of conductivity (k), density (ρ), and specific heat capacity (c).

$$TI \cong \sqrt{kpc} \qquad \textbf{Equation 3}$$

On a planetary surface, TI solely depends on the material itself and is not affected by the latitude, local time, or season. Derived from TIR observations combined with thermophysical models (Kieffer, 2013; Mellon et al., 2000; Bandfield et al., 2012), TI is extensively used to investigate the surface properties of planetary bodies, including Mars, the Moon, Mercury, and asteroids (Chase et al. 1978; Christensen and Kieffer, 1979; Palluconi and Kieffer, 1981; N. M. Smith et al., 1981; Christensen, 1982; Jakosky and Christensen; 1986; Christensen. 1986; Fergason et al., 2006; Christensen and Kieffer; 2006; Putzig and Mellon; 2007; Edwards et al., 2018; Ahern et al., 2021).

However, interpretation of TI can prove complicated due to the complexity of various mixing scenarios (homogenous surface, lateral mixing, and vertical layering). Where material mixtures are horizontally and vertically heterogeneous at the scale of the thermal skin depth (i.e., the maximum penetration depth of a diurnal or annual temperature cycle), the object’s apparent thermal inertia will fundamentally differ from either component. Under these conditions, the surface will behave as one homogenous unit (Jakosky, 1986; Putzig, 2006; Putzig and Mellon, 2007). However, as seen in in-situ surface investigations, more than one material is commonly exposed at the surface (Price, 1977; Kahle and Gillespie, 1976; Palluconi and Kieffer; 1981; Nowicki and Christensen, 2007). A material's diurnal temperature curve is commonly asymmetrical as its temperature tends to peak in the early afternoon and dissipate at night. Where that curve represents mixtures of different TI units, the shape and amplitude of the curve are impacted depending on the relative proportions of those units, their vertical or lateral mixing, and their individual thermophysical properties (Kieffer et al., 1972; Byrne and Davis, 1980; Palluconi and Kieffer; 1981; Nowicki and Christensen, 2007; Putzig and Mellon, 2007; Ahern et al., 2021) (Figure 3). For heterogeneous mixtures where the material properties vary at scales above the thermal skin depth, the different temperatures of components become mixed, and the radiance observed by an orbital instrument is a composite of the radiances emitted by each element.

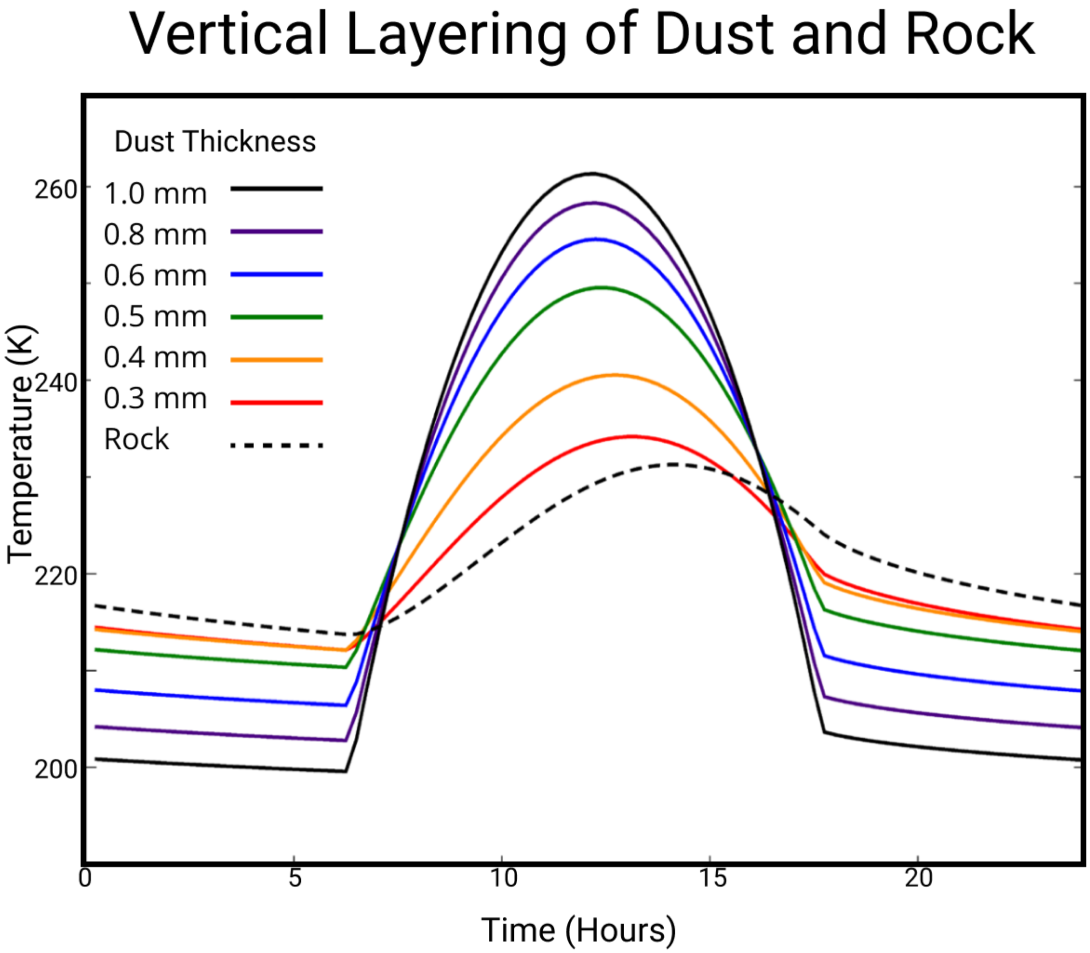

Figure 3. Dirunal curve demonstrating the asymmetrical nature of peak temperature due to composition.

Separation of mixed component surfaces with different TIU is possible using TIR spectral emission and temperature data, but only if the temperature contrast between the units is significant (Ahern et al., 2020; Cowart and Rogers, 2021). Where surface temperatures between components converge, the elements are inseparable. Under these conditions, the surface behaves isothermally. The resulting emission spectrum and band-dependent BT do not exhibit enough leverage in the data to model or quantify the distribution and relative abundance of individual components.

2.2.2.1 KRC: A Thermal Model for Analysis of Mars Infrared Mapping

KRC is a thermophysical model designed to calculate the global surface and subsurface temperatures of Mars, as well as apparent TI values, under a complete set of seasonal and diurnal conditions (Figure 4). KRC has been extensively used to model complex Martian surface conditions from orbital and in-situ observations (Fergason et al., 2006a, Fergason et al., 2006b; Edwards et al., 2009; Kieffer, 2013, Hamilton et al., 2014; Edwards et al., 2018; Ahern et al., 2021; Cowart and Rogers, 2021; Singh and Uttman, 2022; McKeeby et al., 2022). The model assumes a one-layer spectrally gray atmosphere at solar wavelengths and accounts for condensation and atmospheric pressure variations. Surface and atmospheric temperatures are considered to be radiatively coupled. Surface temperatures are calculated by solving the heat conduction equation using explicit forward-finite differences. Upwelling from surface emission, downwelling radiation, an insulating bottom layer, direct and diffuse insolation, and the latent heat of CO_2 are all considered in the model (Kieffer, 2013).

KRC covers various model inputs accounting for latitude, longitude, local time, and solar longitude (Ls), albedo, elevation, slope, dust albedo, and visible dust opacity at the time of observation. Albedo input values were obtained from a 2 pixel per degree (ppd) TES global albedo map, and dust opacity was extracted from the dust climatology database (Montabone et al., 2020) using the latitude, longitude, L_s, and Mars year.

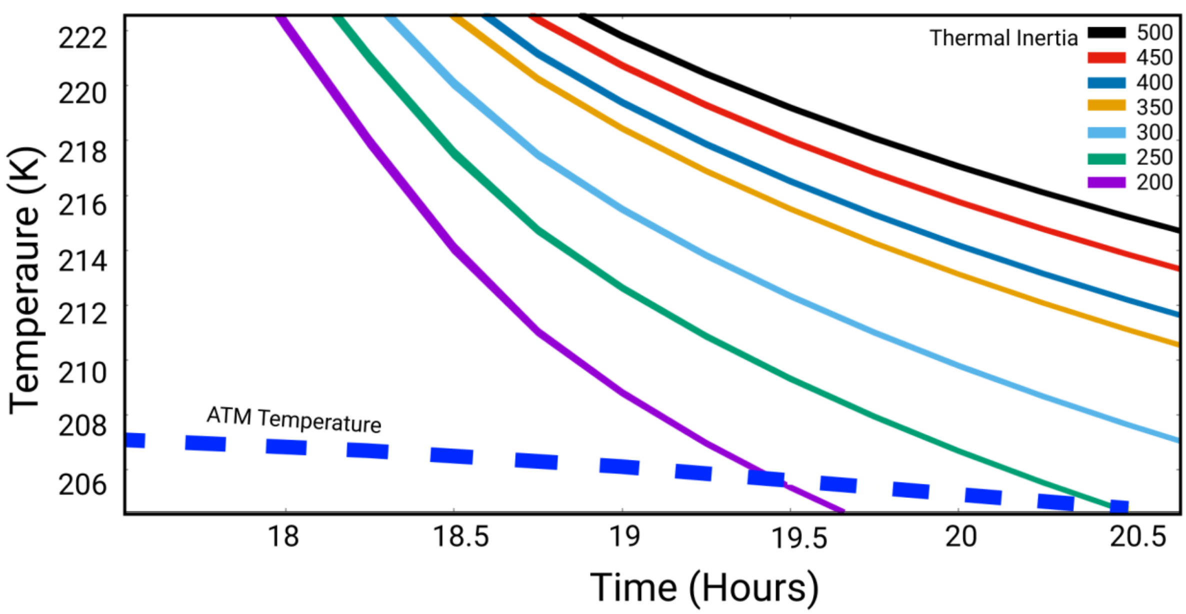

Figure 4. KRC model output showing predicted surface and atmospheric temperatures for a range of thermal inertia values over local times of 17.5 to 20.5 hours.

2.2.3 Albedo effects

Along with thermal inertia, the second dominant parameter affecting temperature is albedo. Whereas thermal inertia predominantly affects the amplitude of diurnal variation, albedo primarily affects the diurnal average temperature (Kieffer et al., 1972, 1973; Jakosky et al., 2000). Albedo is defined as the amount of solar energy absorbed by the surface. As such, lower albedo surfaces typically exhibit greater surface temperatures on average than high albedo surfaces. Albedo can also vary with time, both seasonally and from year-to-year. These variations can result from compositional changes at the surface or active surface processes (i.e., active aeolian transport, deposition, erosion, space weathering, etc.) (Kieffer et al., 1972; Pleskot and Miner, 1981; Christensen, 1988; Mellon et al., 2000). On Mars, early work by Palluconi and Kieffer (1981) found a bimodal anticorrelation between albedo and thermal inertia with low thermal inertia regions limited to high albedo and high thermal inertia regions limited to low albedo. However, this is not exclusively the case, as higher-resolution TES data (~2 km/pixel) revealed a third mode of moderate-to-high thermal inertia and intermediate albedo (Mellon et al., 2000). Additionally, using THEMIS data (~ 100 m/pixel), Edwards et al. (2009) demonstrated that high-thermal inertia surfaces do not exclusively occur in low-albedo, dust-free regions, with a significant fraction of bedrock occurring in moderate to high-albedo areas (>0.2).

Surface thermal emission is also strongly correlated to surface albedo. Emissivity exhibits a nearly linear increase or decreases as albedo increases or decreases (Christensen, 1982). This correlation has been linked to composition differences between high and low albedo endmembers. High albedo surfaces (albedo > 0.18) are typically interpreted as fine-grained, oxidized, and dust-covered with spectral shapes distinctive of fine particulate silicate materials (Ruff and Christensen, 2002; Bandfield and Smith, 2003). High albedo surfaces are typically spectrally grey and exhibit near-unity emissivity values between 200 and 1300 cm^{-1}. In contrast, low albedo (≤0.18) surfaces are considered spatially heterogeneous in composition and temperature as well as commonly exhibit spectral features of the major rock-forming minerals (i.e., plagioclase feldspar, pyroxenes, olivine, sheet silicates, and volcanic glass) (Rogers et al., 2007).

2.3 Thermal Infrared Spectroscopy

Thermal infrared spectroscopy measures the vibrational properties of a material or surface to describe its composition or physical characteristics. Where deriving composition, the Christiansen feature, transparency features, and Reststrahlen bands constitute the major diagnostic features commonly observed in most TIR spectra. These features' size and position depend on each material's refractive index (n) and absorption coefficient (k). The Christiansen feature (CF) is an emissivity maximum where n is equal or nearly equal to the surrounding medium and k is low (<0.1) so that absorption is minimized (Conel, 1969; Ruff and Christensen, 2002). Generally, it is considered an indicator of the degree of silicate polymerization within a mineral and has been used to identify and quantify silicate compositions (Conel, 1969; Logan et al., 1973; Salisbury and Wald, 1992; Hamilton, 2000; Hamilton and Christensen, 2000; Cooper et al., 2002; Hamilton, 2010; Greenhaagen et al., 2010). For silicate compositions, longer wavelength CF positions indicate more mafic materials (silica-poor chain silicates), and shorter wavelength CF indicate more felsic materials (silica-rich framework silicates) (Logan et al., 1973; Hamilton, 2010).

Other major spectral features are Reststrahlen bands and transparency features. Reststrahlen bands arise from surface scattering where the extinction coefficient is high, and light cannot propagate through a material. In silicate minerals, this typically occurs between 8-25 μm and results in an emissivity minimum (McCarthy, 1963; Vincent and Hunt, 1968; Conel, 1969; Hapke, 1981, 1984; Arnold and Wagner, 1988; Salisbury and Walter, 1989; Salisbury & Wald, 1992, Mustard and Hays; 1997). Lastly, transparency features are present in fine particulate silicate materials where the extinction coefficient (k) is low and manifest as a steady decrease in emissivity with decreasing particle size or increased transmission and scattering in low k regions. At wavelengths shorter than the CF, transparency features occur between Reststrahlen bands. Volume scattering refers to the processes where k is very small (<<1.0), and n is greater than 1 (Mustard and Hays, 1997). In this situation, the photons experience multiple surface interactions over a large number of interfaces. Photons cannot escape, resulting in a decreased spectral contrast in the Reststrahlen bands and increased transparency bands (Salisbury and Wald, 1992, Hamilton, 2010). Understanding these effects is vital to distinguish compositional features from scattering, especially on planetary surfaces containing dusty or fine particle-size material (Christensen and Moore, 1992; Pieters et al., 1993; Hamilton, 2010).

2.3.1 Particle size and Roughness Effects

The physical properties of a material, such as particle size, packing, and roughness, can also produce strong effects on the TIR emission spectrum and must be considered. This is especially true regarding the non-uniform nature of planetary surfaces. Most notably, particle size effects due to multiple surface scattering result in a stark decrease in spectral contrast in the Reststrahlen bands. As particles become very fine, volume scattering plays an increased role over surface scattering, where grains become optically thin at Reststrahlen band wavelengths (Salisbury and Wald, 1992). The combined and competing effects of volume and surface scattering can result in a nonuniform spectral reduction, thereby affecting the spectral shape. This has been extensively studied in TIR spectra of lunar soils taken by the Diviner Lunar Radiometer Experiment onboard NASA’s Lunar Reconnaissance Orbiter and on other airless bodies (Aronson et al., 1966; Perry et al., 1972; Salisbury et al., 1997; Greenhagen, 2010; Bandfield et al., 2011; Donaldson Hanna et al., 2016; Lucey, 2017, Shirley, 2018; Donaldson Hanna et al., 2019)

TIR spectra are sensitive to surface roughness from the micrometer to meter scale, including at or below the spatial resolution of current orbital instruments. However, scale-dependent roughness effects the TIR spectrum in various ways. At the micrometer scale, surface scattering of emitted energy decreases the intensity of TIR absorption (Reststrahlen) bands where rough features are thin enough to be transmissive and allow for volume scattering (Kirkland, 2003) or where the rough surfaces contain cavities resulting in multiple surface reflections (Ramsey and Fink 1999; Carter et al., 2009; Berger et al., 2020). In the second case, photon trapping results in multiple surface reflections before the photons are absorbed. Due to the relationship between reflectance and emissivity (equation 4), any addition of reflected energy will increase the emissivity of absorption bands and an overall decrease in spectral contrast, mimicking the effects of a blackbody addition to the spectrum (Williams, 1961; Ramsey and Fink, 1999).

$$R = 1 - \varepsilon \qquad \textbf{Equation 4}$$

Where R is reflectance and ε is emissivity. This has been demonstrated in remote sensing of highly vesiculated igneous targets (Ramsey and Fink, 1999; Carter et al., 2009) and manufactured silica glasses of varying roughness (Berger et al., 2020).

Further work by Osterloo et al. (2012) demonstrated that not all rock surfaces exhibit cavity effects and photon trapping. Instead, spectral contrast decreases with surface roughness until a roughness threshold is achieved, after which further reductions in spectral contrast do not occur, or spectral contrast may begin to increase. This threshold may indicate the transition from cavity effects to fewer surface reflections. Regardless, the reduction in spectral contrast is non-uniform across all wavelengths of the spectrum, and spectral features no not significantly change shape or position.

On planetary surfaces, macro-scale roughness (millimeter to meter scale) results in varying degrees of sunlit and shadowed local slopes (Bandfield and Edwards, 2008; Banfield et al., 2015; McKeeby and Ramsey, 2020; McKeeby and Ramsey, 2021). If this occurs below the spatial resolution of the instrument, anisothermal effects directly proportional to the degree and distribution of these macro-scale slopes occur in each pixel's spectrum. After temperature-emissivity separation, these anisothermal effects can result in a negative spectral slope proportional to the degree of anisothermality. Surfaces with greater degrees of topographic roughness produce more shadows and reflections and exhibit a greater magnitude of negative spectral slopes than those with lower roughness.

On rough surfaces, the relative proportions of sunlit and shadowed surfaces within an instrument FOV change based on the viewing angle. Multiple emission angle measurements provide a direct measure of these surfaces by tracking the change in illumination with the ROTO angle. For instance, rough surfaces exhibit warmer apparent temperatures where the spacecraft's azimuth angle approaches that of the sun's angle. Secondly, where observed from a single viewing geometry, both sub-pixel sunlit and shaded surfaces are observed. This creates an anisothermal pixel area that does not behave in a Planck-like manner. Surface roughness can be derived by comparing the emitted radiance from an anisothermal surface with predicted radiance from a radiative equilibrium thermal model and Gaussian based slope distribution model (Bandfield et al., 2015).

Derivation of surface roughness using TIR data has been demonstrated for the Moon, Mars, and other airless bodies (Jakosky et al., 1990; Bandfield and Edwards, 2008; Bandfield, 2009; Bandfield et al., 2015; Davidsson et al., 2015; Rozitis, 2017; Glotch et al., 2019; Rozitis et al., 2020; Fornasier et al., 2020). The derivation of surface roughness on sub-pixel scales reveals vital information about regolith properties, characterization of crater ejecta, surface slope distributions, and volcanic processes. For example, the roughness of a lava flow during emplacement and its subsequent alteration manifests in cm-m scale topographic variation (e.g., lava flow morphologies indicative of effusion rate and effusion volume). Other applications of sub-meter surface roughness include, but are not limited to, insight into sedimentary deposition and surface evolution, dust mantling and transport, duricrust formation, and rock abundance (Shepard et al., 2001; Nowicki et al., 2007; Bandfield and Edwards, 2008; Edwards et al., 2009).

2.4 Thermal Behavior of Mixed Surfaces

TIR spectra are sensitive to thermal mixing on a broad range of scales, including those at or below the spatial resolution of current orbital instruments. The thermal inertia, albedo, and roughness at scales from micrometers to centimeters, combined with the incident solar radiation, determine the kinetic temperature of the surface, independent of its composition. However, the derived pixel-integrated brightness temperature varies as a function of wavelength and degree of sub-pixel temperature mixing. For example, the viewing geometry combined with a mixed temperature surface will result in a different pixel-integrated temperature compared to the same surface viewed at nadir (Bandfield et al., 2015). Surfaces containing sub-pixel mixtures of materials of differing thermal inertia typically show variable (anisothermal) surface temperatures, and the combined radiance from objects of different temperatures no longer matches that of a single blackbody radiance spectrum (Jakosky, 1978; Nowicki and Christensen, 2007; Ahern et al., 2021; Cowart and Rogers, 2021). Here I refer to this as sub-pixel anisothermality.

Changes in the measured emitted radiance from varying emission angles can accentuate this sub-pixel anisothermality, as opposed to other potential causes such as an incorrect assumption of the maximum emissivity (e.g., Bandfield and Edwards, 2008; Osterloo et al., 2008; Bandfield et al., 2015). For example, although nearly all silicate phases exhibit near-unit emissivity at some point in the THEMIS wavelength range, however, some chloride salts have emissivity values much less than 1.0 (Lane and Christensen, 1998; Osterloo et al., 2008). Where this occurs and an assumption of 1.0 is used to separate the temperature and emissivity, the target temperature is underestimated, and a negatively sloped emission spectrum results (Ruff et al., 1997; Osterloo et al., 2008; Bandfield, 2009). However, variations in viewing geometry or observing conditions of these "graybody" surfaces do not change the magnitude of spectral slopes, unlike in an anisothermal surface, where the spectral slope variability is a function of temperature mixing at a particular viewing geometry (Bandfield, 2009).

Where sub-pixel anisothermality occurs within an instrument's field of view, the surface no longer behaves in a Planck-like manner with respect to wavelength and temperature. Instead, the Planck radiance function can only match the measured radiance at a single wavelength. Therefore, standard temperature/emissivity separation analysis is flawed, as it relies on the assumption of a homogenous pixel temperature. This results in an emission spectrum with negatively trending slopes at longer wavelengths that may complicate subsequent compositional analysis (Bandfield, 2009; Rose et al., 2014; Bandfield et al., 2015). Our work utilizes specialized instrument pointing angles acquired close in time to maximize off-nadir viewing. At off-nadir emission angles, surface anisothermality varies as THEMIS observes different surface units at differing relative proportions. To replicate the various solar illumination conditions achieved by off-nadir viewing would require multiple nadir observations collected at various seasonal and local solar times (Bandfield and Edwards, 2008; Bandfield, 2009). However, this alternative method comes with the added complication of surface and atmospheric changes that may occur between nadir observations.

2.4.1 Thermal Mixing and Brightness Temperature

Depending on the target's season, time of day, and latitudinal location, the surface can be colder than the atmosphere. Where this occurs, atmospheric emission is more significant relative to surface emission (Cowart and Rogers, 2021). This limits the usability of emissivity due to the inability to perform a complete atmospheric radiance correction (Bandfield et al., 2004). This is the case with most THEMIS data acquisitions acquired after 2015, which are collected at or near local sunset due to the current Odyssey orbit. In lieu of emissivity, pixel-integrated brightness temperature (BT), derived at wavelengths least affected by the atmosphere, can be used as a proxy to assess the degree of surface thermal mixing. Like emissivity, BT is controlled by surface roughness, local true solar times (LTST), solar longitude (Ls), thermal inertia, and albedo. Additionally, it assumes a wavelength-dependent Planck-like emission . Therefore, if plotted as a spectrum (temperature vs emissivity) it exhibits a negative slope for anisothermal surfaces for the same reasons as the sloped emissivity spectra. However, wavelength depended BT measurements face the same limitations on surface and atmospheric temperature that emissivity do. Where atmospheric correction cannot be successfully performed, only temperatures acquired from atmospherically transparent spectral regions can be used. In the case of THEMIS this is at ~12.5 µm.

2.5 Instrument descriptions

2.5.1 Thermal Emission Imaging System (THEMIS)

THEMIS has been orbiting Mars onboard the Mars Odyssey spacecraft for over 20 years following a sun-synchronous orbit. As of 2015, the spacecraft has followed the terminator allowing for sunrise and sunset viewing of the surface. The THEMIS instrument consists of two multispectral cameras, a 10-band infrared camera with 100 m/pixel spatial resolution, and a 5-band visible/near-infrared (VIS/NIR) imager with 18 m/pixel spatial resolution (Christensen et al., 2004). The IR system consists of a 320 by 240 element uncooled microbolometer array with ten bands centered at nine different wavelengths, each with an average bandwidth of ~1 µm. Bands 1 and 2 are designed to have identical filters centered at ~6.8 µm to improve the signal-to-noise at the shorter wavelength region. The remaining bands are centered at ~7.9, 8.6, 9.4, 10.2, 11.0, 11.8, 12.6, and 14.9 µm. The visible camera bands cover the wavelength range of 0.425–0.860 µm. A full description of the instrument and calibration is given by (Christensen et al., 2004).

Briefly, THEMIS data are atmospherically and radiometrically corrected by assuming uniform atmospheric conditions over the scene. Atmospheric emission and scattering are then removed using a surface of assumed uniform composition and variable temperature. Thermal Emission Spectrometer (TES) data with a lower spatial resolution and higher spectral resolution are used to determine surface emissivity (e.g., Smith et al., 2000, Bandfield and Smith, 2003, Bandfield et al., 2004; Bandfield, 2008) over a relatively uniform training region to characterize atmospheric properties. The atmospheric properties are then subtracted and divided out of the

THEMIS data resulting in surface emissivity. The specifics of the atmospheric correction processes are discussed in more detail in Chapter 4, Section 2, and Chapter 5, Section 3.

2.5.1.1 ROTO description

Historically, ROTOs by the Mars Odyssey spacecraft have been used to provide off-nadir viewing of the Martian surface. This reorientation of the spacecraft has allowed for TIR data acquisition of hard-to-image targets (i.e., polar regions), as well as studies into atmospheric properties using limb measurements and imaging of the Martian moons, Phobos, and Deimos (Smith, 2009; Bandfield et al., 2018; Edwards et al., 2019, Montabone et al., 2020). Where applied to surface investigations, ROTO data provide a unique view and measure of TIR radiance at varying emission angles within a relatively short acquisition period. For thermophysical studies, ROTO data are typically collected over two weeks allowing near-identical surface footprints to be imaged at differing emission angles and under similar Local True similar Local True Solar Time (LTST), Ls, and atmospheric conditions (Figure 5). This provides an excellent opportunity for the analysis and modeling of anisothermal spectral effects. Solar Time (LTST), Ls, and atmospheric conditions (Figure 5). This provides an excellent opportunity to analyze and model anisothermal spectral effects.

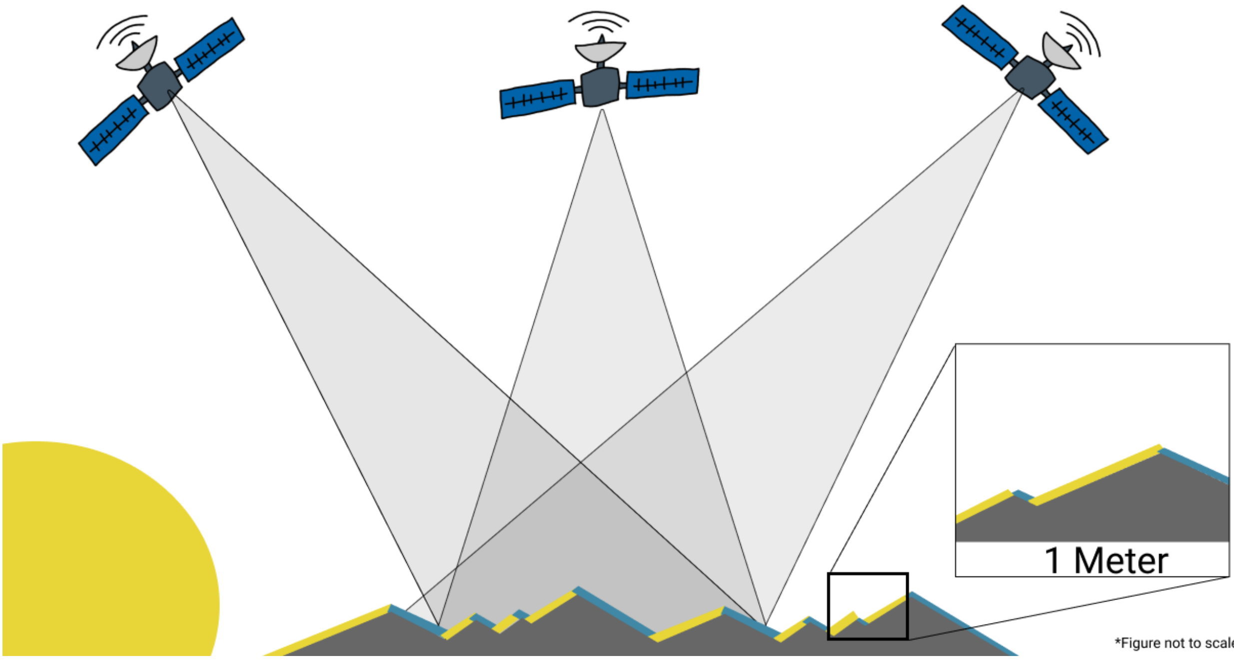

Figure 5. Schematic showing the concept of ROTO observations to collect TIR image data from varying emission angles.

The first ROTO sequence explicitly designed to investigate surface roughness was performed in September 2017 and covered a region within Daedalia Planum centered at 237.62°E and -23.26°N. This area contains a unique set of lava flows that display atypical THEMIS thermophysical properties recorded during daytime and nighttime overpasses (Crown and Ramsey, 2017; Simurda et al., 2019). In March of 2020, a series of eight new ROTO observations were collected from 18:00h to 19:00h LTST, 38° to 47° L_s, 93° to 102° solar incidence, and surface emission angles from -31° to +33°. Images are centered around 174.26° E, -6.40°N and cover an area that includes Apollinaris Mons caldera, extends north into the lower Medusae Fossae formation, and south towards Gusev Crater. This ROTO campaign was specifically designed to investigate the surfaces' thermophysical properties. Apollinaris Mons was chosen due to the documented presence of rough surface features (Bandfield, 2009; Zimbelman et al., 2010) as well as the contested formation hypothesis of the Medusae Fossae Formation (MFF; Edgett et al., 1997; Tanaka, 2000; Bradley et al., 2002; Hynek et al., 2003; Mandt et al., 2008). The findings of this roto acquisition will be discussed extensively in chapter 4.

2.5.2 Thermal Emission Spectrometer (TES)

TES consists of three instruments, a Michelson interferometer, a broad band radiance sensor, and a solar reflectance sensor, packaged together to measure radiant infrared and visible energy. The interferometer covers a wavelength range from 6 to 50 µm (~1650-200 cm^{-1}) with a 5 and 10 cm^{-1} spectral resolution. The broadband sensor consists of a single band, measuring radiance from 5.5 to 100 µm and the solar reflectance sensor views the planet in the 0.3 to 2.7-micron range. Each sensor has six detectors arranged in a 3×2 array with a field of view of 8.3-mrad, giving TES a spatial resolution of ~3 km from orbit (Christensen et al., 1992, 2001).

2.5.3 High Resolution Imaging System Experiment (HiRISE)

The High-Resolution Imaging Science Experiment (HiRISE) is a visible camera onboard the Mars Reconnaissance Orbiter (MRO). HiRISE consists of a 0.5m diameter primary mirror with a 12 m effective focal length and 14 charge-coupled devices (CCD) detectors, each with two output channels. The instrument has a spatial resolution of 0.25-1.3 m/pixel and is capable of stereo imaging and topographic measurements with a ≥25cm vertical precision. Typically, swath widths of image acquisition are ~6 km wide through the broad bandpass red filter with the central 1.2 km of that swatch imaged through blue-green and a near-infrared (NIR) filter. This allows for a 3-band false color image to be collected over the central ~20% of the image (McEwen et al., 2007).

2.5.4 The Context Camera (CTX)

The context camera (CTX) is an imaging system on board the MRO designed to provide a big-picture background view of terrains around other targets imaged by other instruments on the MRO. The instrument consists of a 350mm telescope with an aperture of f/3.25 and a 5.7° field of view. This results in a ~30 km swath width from a ~290 km altitude. The camera onboard consists of a 5000-element CCD with a bandpass of 500-700nm and a ~6 m/pixel spatial resolution. The camera is designed to acquire images simultaneously with HiRISE and the Compact Reconnaissance Imaging Spectrometer for Mars (CRISM) to provide a broader context for the data collected by those two instruments (Malin et al., 2007).

2.5.5 Mars Orbiter Laser Altimeter (MOLA)

MOLA,-one of five instruments onboard the Mars Global Surveyor (MGS), was designed to-provide topographic mapping capabilities of the Martian surface using an infrared pulsed laser. MOLA has a spatial resolution of 4 km, a shot spacing track of 0.3 km, and a fire rate of 10× per second. This resulted in precise global topographic mapping that can be used to investigate km scale surface roughness, surface slopes, and other topographic characteristics of the surface.

3.0 Deriving planetary surface roughness: Combining digital photogrammetry and thermal infrared spectroscopy

3.1 Introduction

Surface roughness impacts TIR spectra at both the micron and macro scales. At the micron scale, surface roughness results in scattering and multiple reflections that decrease the TIR absorption band intensity relative to a specular surface (Bennett and Porteus, 1961; Osterloo et al., 2012; Berger et al., 2020). A roughness to wavelength ratio <0.2 has been shown to cause the most significant effect (Bennett and Porteus, 1961; Porteus, 1963, Berger et al., 2020). Additionally, where a rough surface is composed of optically thin particulates, transmission features due to volume scattering can arise, which may impart transparency features to the spectrum (Salisbury and Wald, 1992; Kirkland et al., 2003).

In settings where rough surfaces contain cavities (i.e., vesicular igneous lithologies), emitted radiation can undergo multiple surface reflections. The resulting emission spectra will contain shallow absorption bands where the photon path is complicated due to multiple reflections (Ramsey and Fink, 1999). Ultimately, this decreases the spectral contrast without causing significant changes in spectral band shape or position (Ramsey and Fink, 1999; Carter et al., 2009; Berger et al., 2020). Adding a blackbody to the TIR emissivity spectrum simulates these effects in spectral deconvolution modeling and can allow for an estimate of vesicularity (Ramsey and Fink, 1999; Carter et al., 2009). Similar results were observed by Osterloo et al. (2012) and Rost et al.

(2018) of rough igneous, metamorphic, and sedimentary rock faces which were either manually roughened (Osterloo) or split/cut (Rost). In both cases, a wavelength-dependent decrease in spectral contrast was observed, with Rost et al. (2018) noting spectral changes due to transparency features and crystallinity effects.

Here, I use a combination of TIR emission spectroscopy and digital stereo photogrammetry to investigate the fine-scale topography of natural basaltic surfaces and derive surface roughness. I also utilize directional emissivity to simulate off-nadir emission data similar to those acquired by THEMIS ROTOs. Directional emissivity describes how the emissivity of the surface changes with viewing angle. For isothermal surfaces, previous studies have demonstrated that emissivity decreases as emission angle increases in much the same way as micron-scale roughness (Wald and Salisbury, 1995; Warren et al., 2019). This change in emissivity is attributed to Fresnel-related effects and not anisothermality. According to the Fresnel equations, the directional emissivity is dependent on the material's refractive index (η). Therefore, the directional emissivity of a conducting surface is isotropic for all emission angles where n is unity. Where η is large, the directional emissivity is isotropic for emission angles $\leq$ 60°. At emission angles $\geq$60°, the emissivity of absorption features decreases with increasing emission angle (Figure 6). In this chapter, I examine the combined effects of surface roughness and directional emissivity on the TIR spectrum in a controlled laboratory setting.

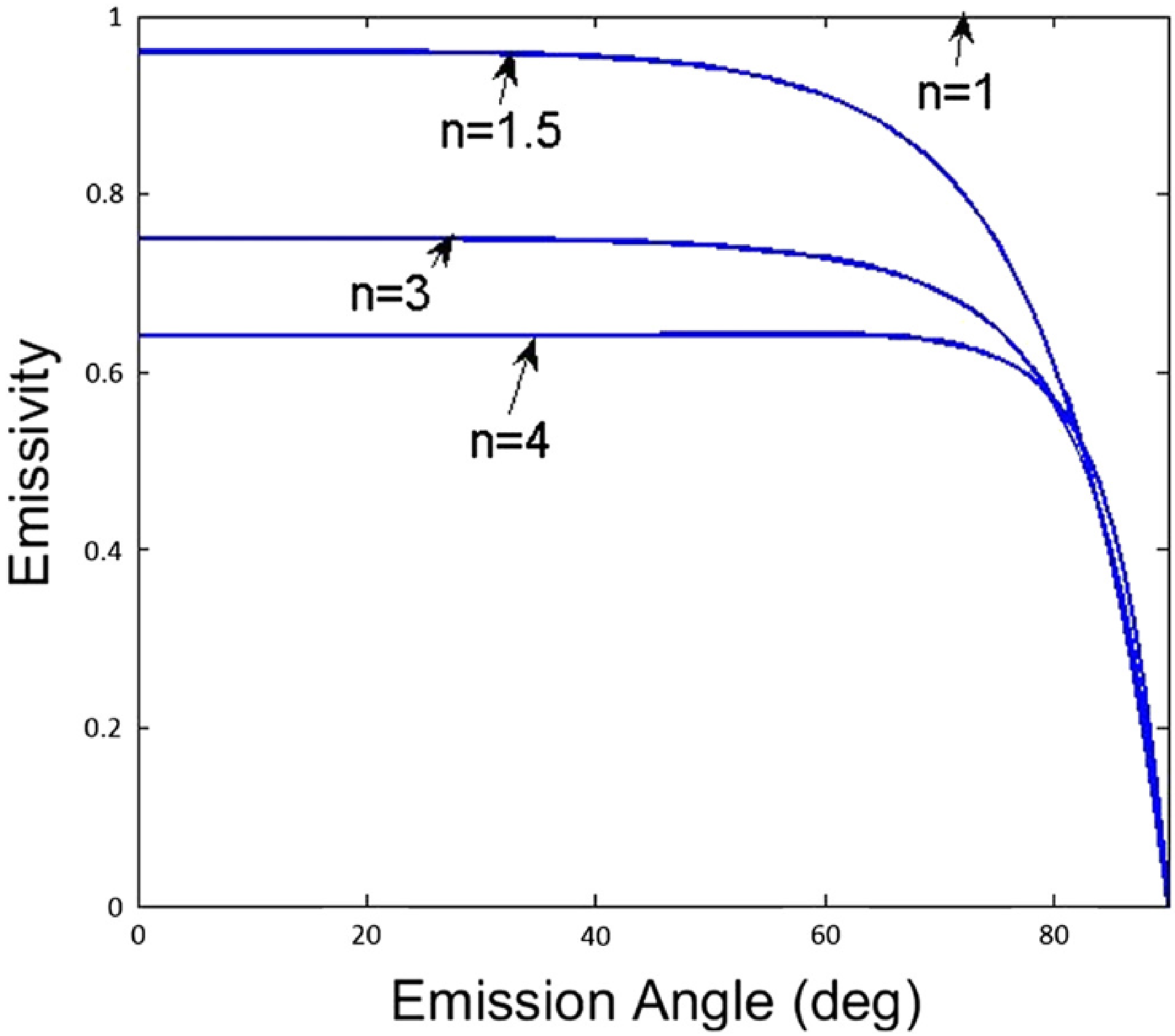

Figure 6. Directional emissivity curves for a conducting material with different indices of refraction (η). Figure adapted from Warren et al. (2019).

Preliminary analysis of ROTO data demonstrates observable changes to TIR emissivity spectra, such as negatively sloped emission spectra and variations in spectral contrast with emission angle (McKeeby et al., 2019; McKeeby and Ramsey, 2020; McKeeby and Ramsey, 2021, McKeeby et al., 2022). Additionally, laboratory studies show a non-linear trend of decreasing emissivity with increasing emission angle, particularly in the Reststrahlen bands (Wald and Salisbury, 1995; Bandfield and Edwards, 2008; Warren at al., 2019; McKeeby and Ramsey, 2020). The multiple scattering and shadowing caused by surface roughness produce complexity beyond the capabilities of simple linear spectral modeling (Warren et al., 2019). This work provides the foundation for studies described in chapters 4 and 5 using ROTOs which are also acquired at varying emission angles.

3.2 Methods

3.2.1 TIR Emission Spectroscopy

A ropy pahoehoe and a'ā sample previously collected from field campaigns in Mauna Ulu flow field, Hawaii, was used for this study (Figure 7). Sample preparation and emission spectra were collected at the Image Visualization and Infrared Spectroscopy (IVIS) Laboratory at the University of Pittsburgh. Before spectral analysis, samples were cut, washed with acetone to remove clinging fines, and mounted on an adhesive surface. Samples were then placed into an oven set at 80°C to remove any adsorbed liquids. Prior to directional heating and analysis, samples were allowed to cool fully to room temperature over 24 hours.

A Thermo-Nicolet Nexus 670 Fourier Transform Infrared (FTIR) Spectrometer paired with a cooled, wide-band mercury cadmium telluride (MCT-B) photovoltaic detector and potassium bromide (XT-KBr) beam splitter is used. This combination allows for a spectral range of 5 - 25µm, a spectral resolution, and an integration time of 0.5 seconds. A custom-built sample stage allows for rotationally variable viewing (McKeeby et al., 2019, McKeeby and Ramsey, 2020). Samples were rotated at 3° increments around the central axis resulting in the same surface being imaged with incremental viewing geometries at a 1.5 cm spot size (Figure 8).

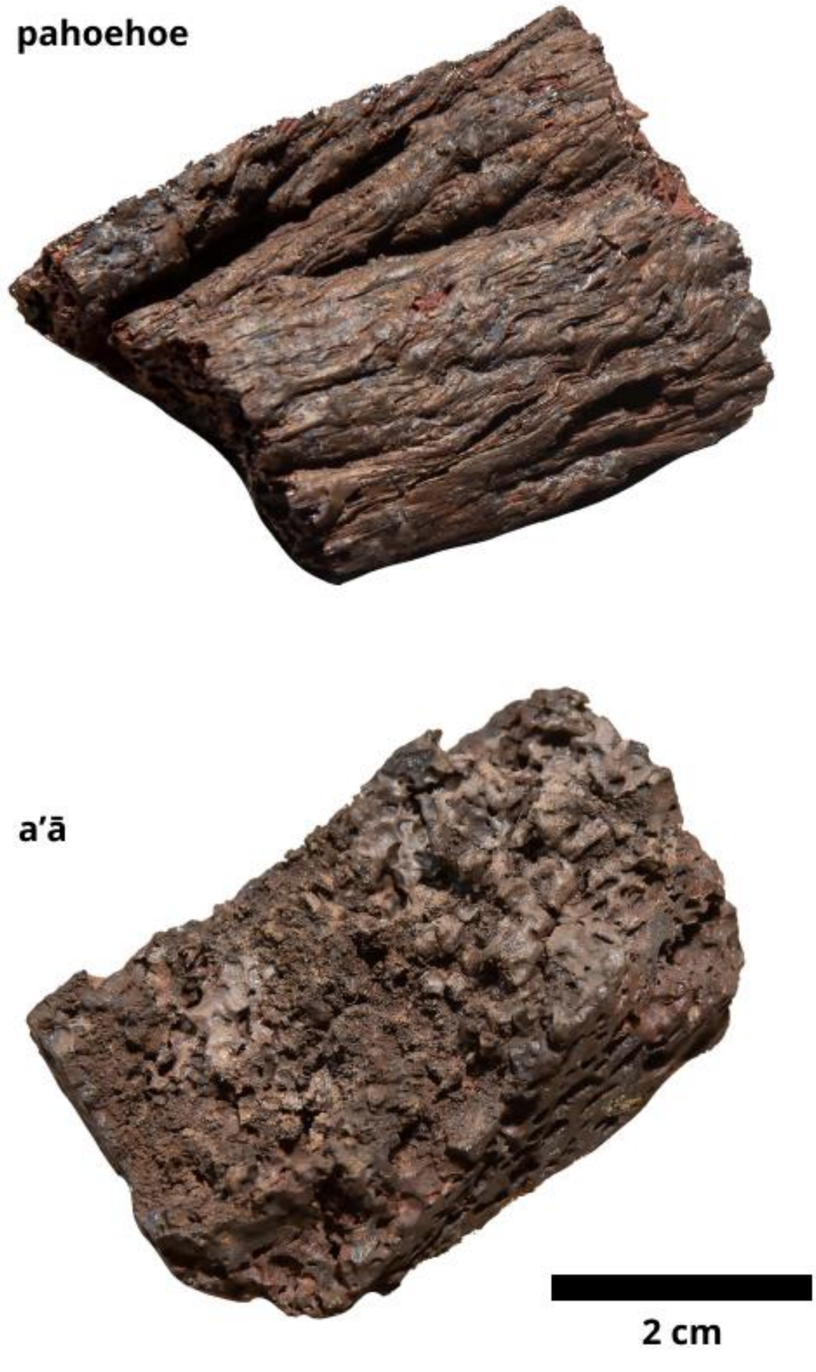

Figure 7. Images of the pahoehoe and a’ā samples used in this study.

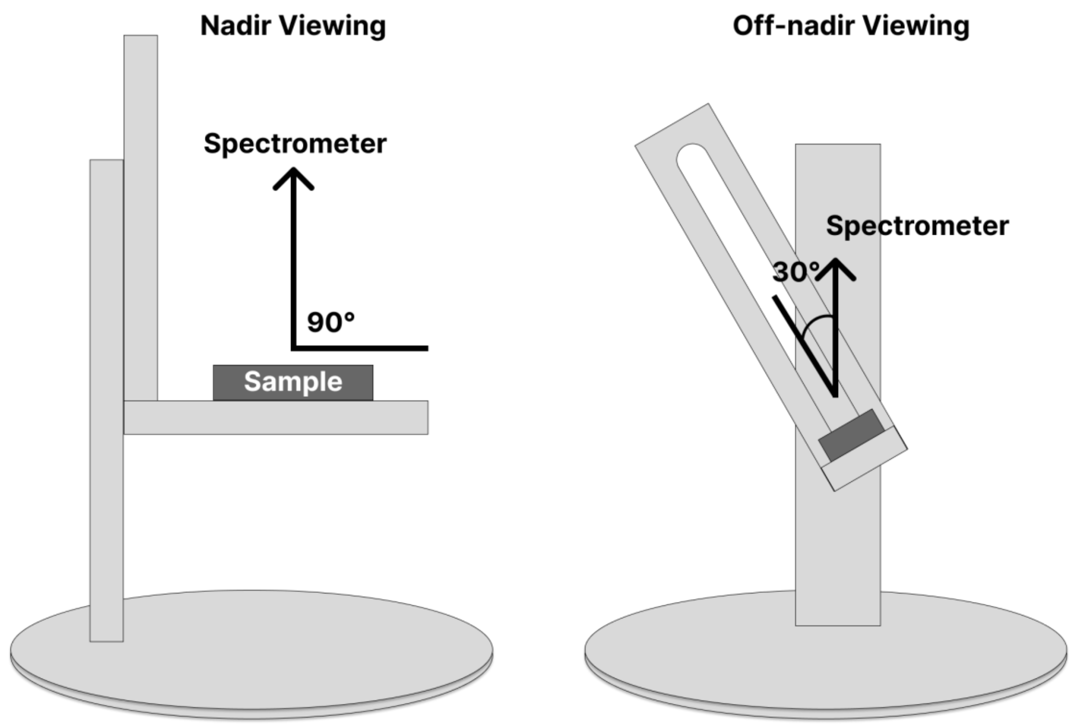

Figure 8. Custom sample stage designed to facilitate spectroscopic acquisition at off-nadir viewing geometries.

Emissivity spectra were acquired following the two-temperature method outlined by Ruff et al. (1997). All samples and blackbodies were placed into an environmental chamber, which was purged using air scrubbed of water vapor and carbon dioxide to minimize atmospheric spectral effects. Before TIR spectral analysis, samples were heated for 30 minutes using a DeWalt® D26960 heat gun set at 230°C and mounted at 45 degrees to and approximately 30 cm from the sample (Figure 9). After ten minutes, the samples reached a stable surface temperature of ~140°C (Figure 10). At the 30-minute mark, the heat gun was turned off, and samples were inserted into the spectrometer chamber for analysis. A total of 10 scans were completed for each sample. This process was repeated 5 times for each sample and the resulting spectra were averaged together to improve the signal-to-noise.

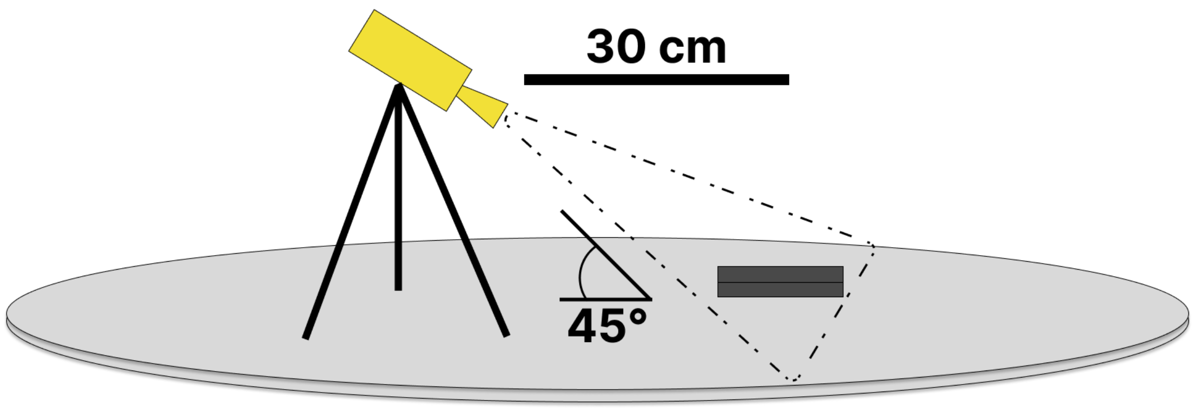

Figure 9. Experimental setup to directionally heat the samples using a DeWalt heat gun.

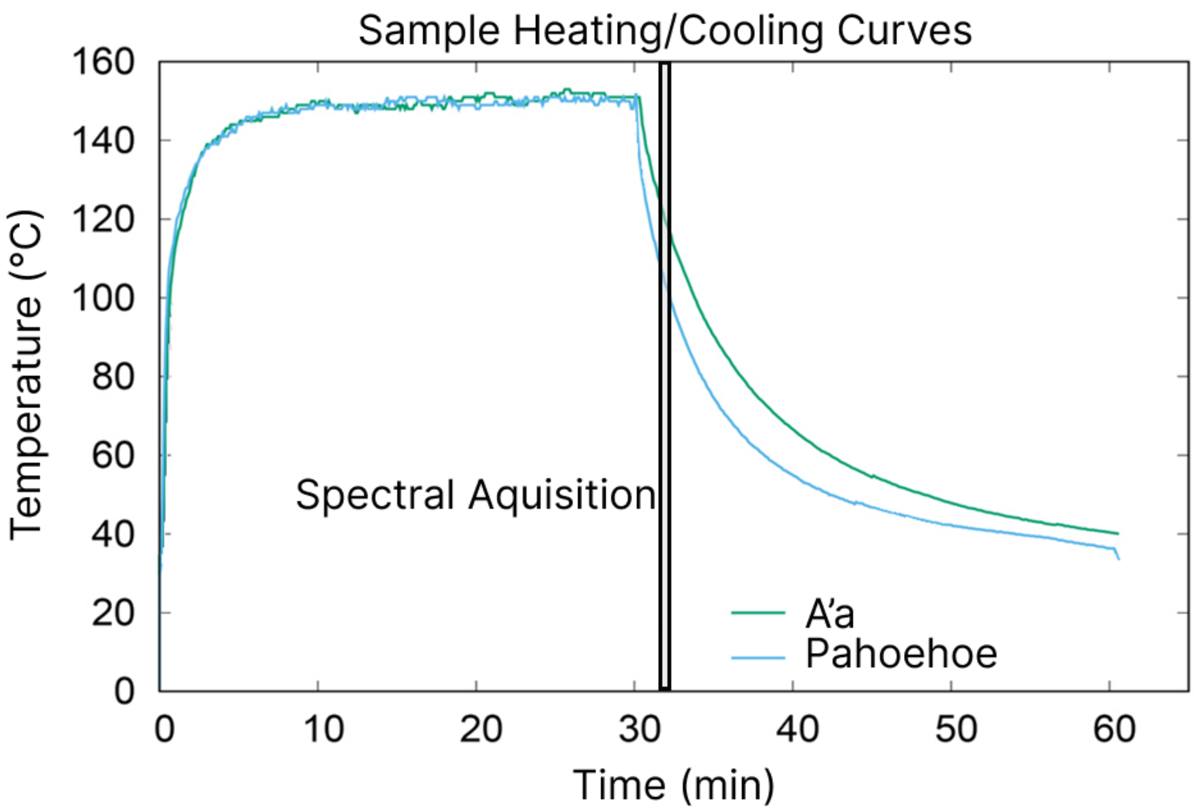

Figure 10. Cooling curves for the a'a and pahoehoe samples.

3.2.2 Surface Roughness Analysis

Three-dimensional (3D) surface reconstruction using digital stereo photogrammetry was performed using 200+ images captured with a 36.3-megapixel Nikon D800 full-frame digital single-lens reflex (DSLR) camera with a 50mm 1.5G prime NIKKOR lens set to an aperture of $f8$. External LED light sources were used to provide constant and even illumination. Samples were placed on a rotating plate with the camera placed ~1 m away and at a 45° angle (Figure 11). Samples were centered in the frame to minimize barrel distortion. Images were acquired every 1s as the sample stage was rotated, and the camera's autofocus was reacquired for every image. An identical approach was followed for the 3D surface reconstruction of commercially available sandpaper. This paper has an American National Standards in Dimensional Metrology (ASME) certified roughness of 10µm. Here, it is used to provide calibration and validate the sensitivity of the 3D reconstruction approach.

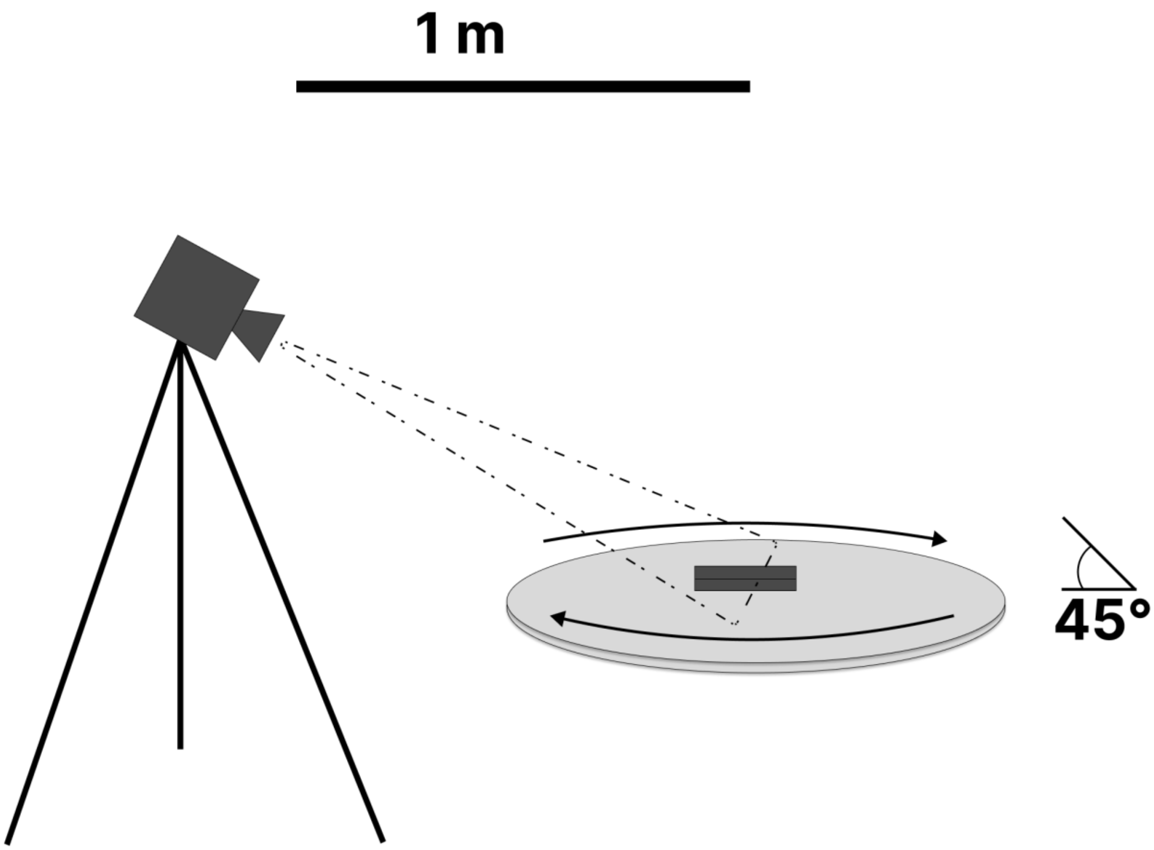

Figure 11. Experimental set up for image acquisition as part of the stereo photogrammetry and 3D surface reconstruction.

Images used for 3D surface reconstruction were compiled in AliceVision Meshroom© software, resulting in point cloud densities with over 46 million points. Meshroom© is an open-source 3D reconstruction software based on the AliceVision Photogrammetric Computer Vision Framework that includes Camera Tracking algorithms. Within Meshroom©, 3d surfaces were digitally rotated about the observing axis to recreate the nadir and off-nadir viewing geometries. No manipulation of the data was performed. After 3D surface reconstruction, statistical topographic analysis using parameters chosen from the AMSE was performed in MATLAB®. Selected parameters include Root mean square (RMS) height, kurtosis, skewness, Hurst exponent, and cross-sectional RMS. Prior to statistical analysis, samples were detrended about a mean surface, and moving means and moving Root Mean Square (RMS) heights were calculated.

The statistical parameters chosen are adapted from the ASME metrology standards for surface roughness quantification. Root mean square height (R_q) describes the standard deviation of points (n) on a surface as a function of their heights (z) relative to the reference plane (xi). $\bar{z}$ is the mean height of the profile over all xi (Figure 12). RMS height is defined by the equation:

$$R_q = \sqrt{\frac{1}{n-1}\sum_{i=1}^{n}(z(xi)-\bar{z})^2} \qquad \textbf{Equation 5}$$

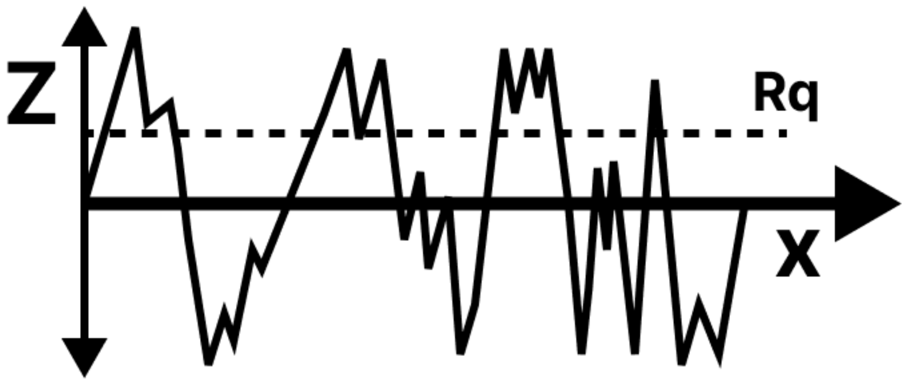

Figure 12. RMS height (Rq) describes the standard deviation of heights about a detrended mean (x).

RMS height was calculated using a 10µm moving window across each 3D surface. Due to the length-scale-dependent nature of surface roughness, R_q alone does not provide an adequate quantification of surface roughness. For example, waviness on the mm scale may cause shadows or bright surfaces where directionally heated. However, it does not affect TIR radiation in a similar way to µm scale roughness. Due to this, the sampling length must be considered and reported where performing surface roughness quantification.

Additional statistical roughness parameters of cross-sectional RMS (RMS_x), kurtosis (S_{ku}), skewness (R_{sk}), and the Hurst exponent (H) were performed better to quantify variations in surface roughness across the sample. RMS_x is the standard deviation of points along a profile. Although similar to R_q described above, RMS_x was measured along two profiles perpendicular to each other. This differs from R_q, which is calculated using a moving window for the entire 3D surface. Kurtosis (S_{ku}) is a statistical parameter describing the sharpness of a profile about a mean line. Essentially, it describes how pointed or rounded the surface is and is calculated using the formula:

$$S_{ku} = \frac{1}{\varepsilon_l^4}\frac{1}{n_l}\sum_{i=1}^{n_l}\left[\frac{1}{p_l}\sum_{j=1}^{p_l} z_j^4\right]$$ **Equation 6**

Where η_l is the number of intervals of length l, ε is the RMS height, p_1 is the number of points within l, and z_j is the height variation from the median line within the interval i. A S_{ku} below 3 indicates a rounded surface and is referred to as platykurtic. S_{ku} values above 3 indicate a greater number of sharp peaks within a narrow range of heights. These are referred to as leptokurtic surfaces and a normal or Gaussian distribution of peaks results in a $S_{ku} = 3$ (Figure 13).

Skewness (R_{sk}) measures the profile's asymmetry about the mean line with positive or negative values indicating an abundance of peaks or valleys, respectively (Whitehouse, 1994). A skewness of 0 indicates an equal distribution. Skewness is calculated using the formula:

$$R_{sk} = \frac{1}{\varepsilon_l^3}\frac{1}{n_l}\sum_{i=1}^{n_l}\left[\frac{1}{p_l}\sum_{j=1}^{p_l} z_j^3\right]$$ **Equation 7**

with ε being the rms height, η_l is the number of intervals of length l, p_1 is the number of points within l, and z_j is the height variation from the median line within the interval i. S_{ku} and R_{sk} were calculated over a 10μm length scale, identical to the RMS_x and RMS height analyses.

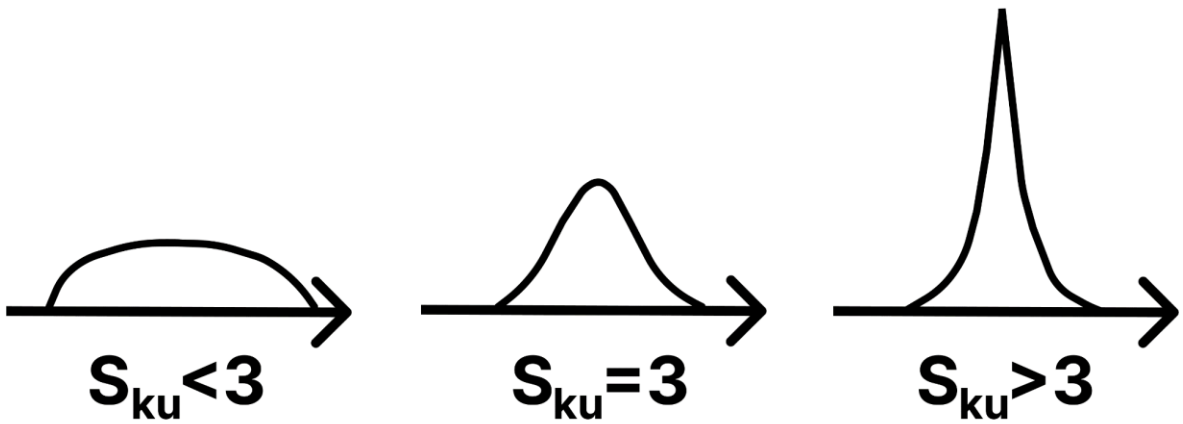

Figure 13. Kurtosis is a measure of the sharpness of the profile.

Lastly, the Hurst exponent describes a surface's self-similarity or fractal nature across different length-scales. Surfaces that become smoother or rougher as the length scale increases (e.g., cm to m) have an H value closer to 0. Whereas surfaces that maintain their roughness or smoothness as the scale increase tend to have an H value closer to one. Here, H is equal to the slope of the line where the RMS deviation (v), also called the Allen variance, is plotted versus the step size in log-log space. The Allen variance is given by the equation:

$$v(\Delta x) = \sqrt{\frac{1}{n}\sum_{i=1}^{n}[z(xi) - z(xi + \Delta x)]^2} \quad \textbf{Equation 8}$$

where z is the height at every step (Δx), n is the number of sample points, and z(xi) is the height of the surface at point xi. For natural terrains, the RMS deviation typically follows a power law that trends with horizontal scale, set by the distance between successive points (Shepard et al., 2001). The Hurst exponent is then given by the equation:

$$v(\Delta x) = V_0(\Delta x)^H \qquad \textbf{Equation 9}$$

Where Δx is the step size and V_0 is the RMS deviation at the chosen horizontal scale (10µm is used here).

3.3 Results

Two-dimensional surface profiles are shown in Figure 14, and statistical results are presented in Tables 1 and 2. The total vertical relief for the pahoehoe sample was measured at ~0.4 mm, with most variation occurring on the ~0.1 mm scale, predominantly caused by the waviness of the pahoehoe ropes (Figure 14a). A small change in RMS_x of 0.05mm was calculated between nadir and off-nadir viewing geometries. Nadir viewing of the sample also produced greater kurtosis and skewness values than off-nadir viewing. In both cases, S_{ku} values range from 2.5-3, with a low R_{sk} consistent with a random distribution of surface features at both nadir and off-nadir viewing geometries. However, where viewed from off-nadir, the R_{sk} drops to negative values, and S_{ku} is greater than 3. This change in R_{sk} indicates that surface features tend to be sharp and below the mean surface height, suggesting a prevalence of pits or vesicles. Where viewed off-nadir the skewness indicates a more rounded topology.

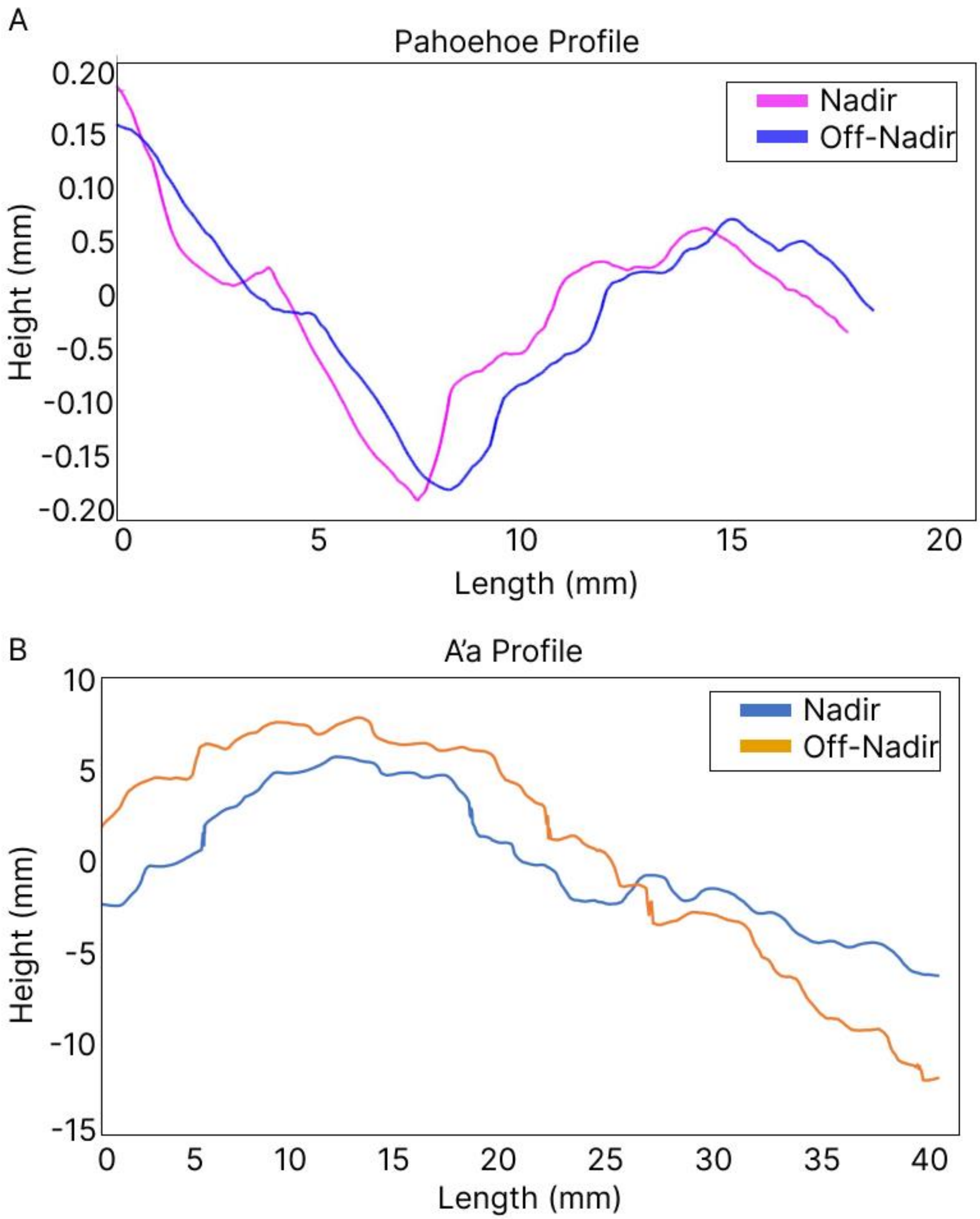

Figure 14. Two dimensional profiles of the A'ā and Pahoehoe samples acquired at nadir and off-nadir viewing geometries.

The measure of the Hurst exponent was relatively the same between nadir and off-nadir at 0.9726 and 0.9678, respectively. Hurst values above 0.5 indicate a fractal-like surface and similar topographic expression at different length scales.

The a’ā sample exhibits a similar trend, and the two-dimensional surface profile is shown in Figure 14b, with statistical results presented in Table 2. The total vertical relief was measured at ~ 20 mm with local height variation on the 5mm scale. RMS_x was more significant in the a’ā sample, as can be expected, where surface heights vary more drastically. The change in RMS_x between nadir and off-nadir was calculated at 0.148mm. The a’ā sample has a S_{ku} <3. Indicating a more rounded surface at both off-nadir and nadir viewing geometries. R_{sk} values were negative where viewed from nadir and slightly positive where viewed off-nadir (Table 2). Like the pahoehoe sample, this indicates a pitted or vesicle-rich surface prevalence. Hurst values were also comparable to the pahoehoe sample, indicative of a self-similar (fractal) morphology from the 10µm to mm scale. Statistically, the samples are similar, with the most significant differences being RMS_x, which is ~10x greater in the a’ā due to its higher vertical relief, and skewness, indicating a more significant proportion of negative features present in the a’ā sample viewed at nadir.

Table 1. Statistical values of pahoehoe cross-sectional profile

Parameter	Nadir	Off-Nadir (23°)
RMS_x (mm)	0.078	0.0832
Kurtosis	3.2869	2.5215
Skewness	-0.0398	0.1912
Hurst	0.9726	0.9678
% Area Less than 50μm	50.2%	54.7%

Table 2. Statistical values of a'ā cross-sectional profile

Parameter	Nadir	Off-Nadir (23°)
RMS_x (mm)	0.657	0.805
Kurtosis	2.1305	2.0498
Skewness	-1.0127	0.1531
Hurst	0.94	0.97
% Area Less than 50μm	65.4%	69.2%

3.3.1 Micron-Scale Surface Roughness

3D surface reconstruction of the a’ā and pahoehoe samples, at nadir and off-nadir, reveal differences in RMS roughness at scales smaller than 50μm. RMS roughness was calculated using the sliding window RMS function in MATLAB, which calculates the RMS of the elevation data for each sample independently across each row and column. A moving window of 10 μm was used. Each sample's RMS height indicates that most variation occurs below 150 μm. Where viewed from off-nadir, the pahoehoe sample has ~4.5% more features with a 50 μm or smaller change in height. Features of this size constitute 50.2% areal coverage at nadir viewing geometries, and 54.7% areal coverage where viewed at 23° off-nadir over the same area (Figure 15). Furthermore, features at the 10 μm scale account for 22.5% of the surface area in the nadir image and 35.1% in the off-nadir image. This is significant as features at the 10’s of the micron scale are closest in size to the TIR wavelengths used in this study and likely to have significant scattering effects, which are apparent in the TIR spectrum.

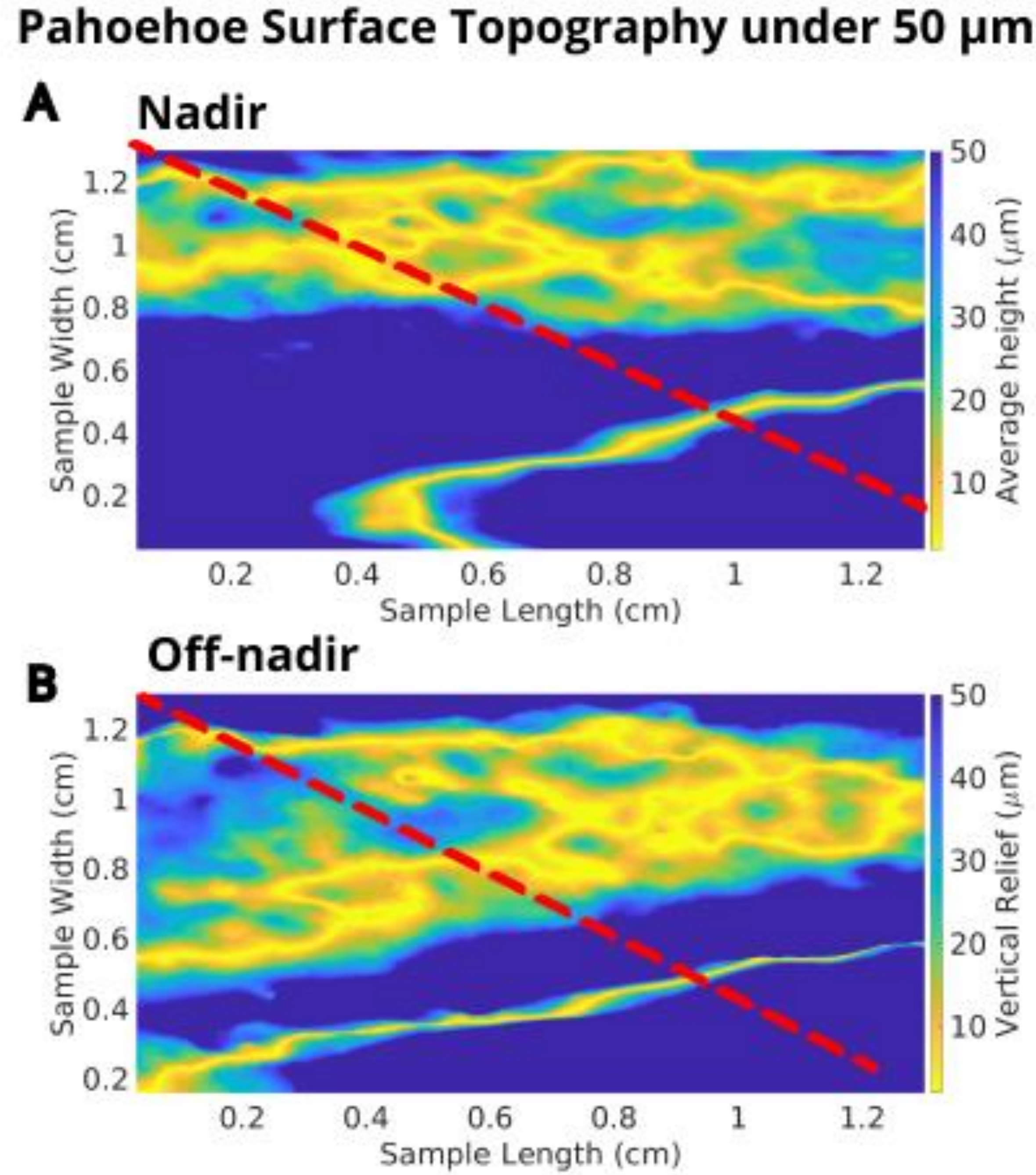

Figure 15. Topographic mapping results show the distribution of 50 µm or smaller surface heights for both nadir and off-nadir viewing geometries of the pahoehoe sample. Dotted lines indicate the cross-section path used for statistical analysis.

The a’ā sample shows a greater size distribution of heights with the majority of variation occurring below 800 μm due to the abundance of peaks and pits discussed previously. Notably, macro-scale roughness in the a’ā is due to vesicles (pits and peaks). In contrast, macro-scale roughness in the pahoehoe sample is predominantly due to waviness in the roughness profile from the pahoehoe’s ropy texture. Where viewed off-nadir, the abundance of small-scale features (vertical change <50 μm) was calculated at ~69%, compared to ~65% at the nadir viewing geometry (Table 2, Figure 16). In both samples, off-nadir viewing geometries resulted in a roughly 5% ± 0.5% increase in small-scale features. This may indicate that off-nadir viewing captures surface features along the walls of vesicles, less exposed to erosional forces than the surface.

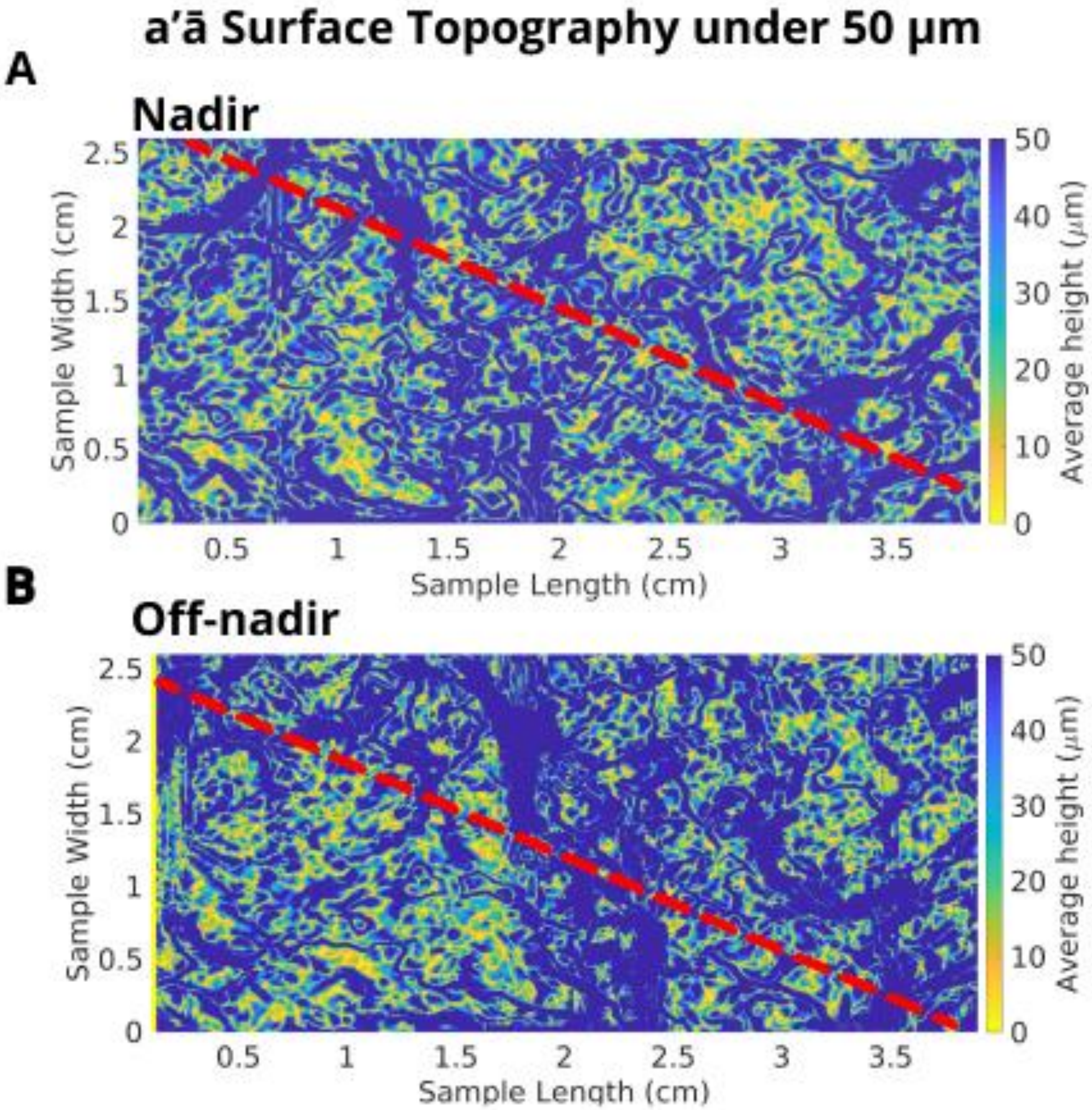

Figure 16. Topographic mapping results show the distribution of 50 µm or smaller surface heights for both nadir and off-nadir viewing geometries of the a'ā sample. Dotted lines indicate the cross-section path used for statistical analysis.

3.3.2 Infrared Spectroscopy

TIR spectral features of these samples are typical of basaltic volcanic glass (Kahle et al., 1988; Crisp et al., 1990; Yant et al., 2016; Minitti and Hamilton, 2010; Berger et al., 2020). Spectra exhibit dominant features at 1240 cm^{-1} (8.1 µm), 1097 cm^{-1} (9.1 µm), and 675 cm^{-1} (14.8 µm), and a less apparent broad shoulder centered around 950 cm^{-1} (10.5 µm). These features are labeled IV, III, and II, sequentially by their position (Fig 17, A-C). Feature I is linked to Al-O vibrations and may suggest evidence for weathering (Crisp et al., 1990). Feature I is seen in both the pahoehoe and a'ā samples and present in both viewing geometries. Generally, the nadir pahoehoe sample shows stronger spectral features than the a'ā sample, regardless of viewing geometry. Where viewed off-nadir, spectral contrast decreases in the pahoehoe (4 ± 0.5%) and a'ā samples (6 ± 0.5%) compared to nadir, the most dominant impact of which is on features I, III, and IV. The a'ā sample exhibits a greater change in spectral contrast between nadir and off-nadir. Spectral feature III (the Si-O stretching feature) increases emissivity by 8% from ~0.83 to 0.91. In comparison, feature III in the pahoehoe sample increases emissivity by 4% from ~0.82 to 0.86 (Figure 17B). The increased spectral depth of feature I at off-nadir viewing geometries suggests an increase in the thickness of an amorphous silica coating. Off-nadir viewing geometries also produce an exaggerated feature I in the pahoehoe sample and the a'ā sample, but to a lesser degree. Lastly, a slight spectral slope is present in the off-nadir viewing geometries potentially related to each sample's directional heating.

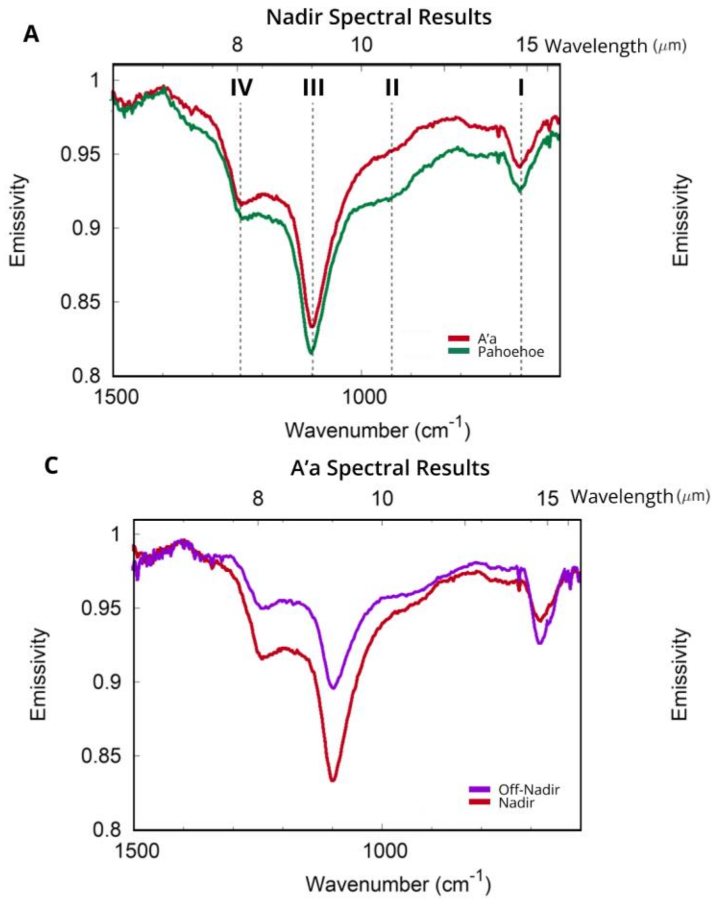

Figure 17. FTIR emissivity results for pahoehoe and a'ā samples show spectral differences between off-nadir and nadir viewing geometries. Spectral features described in the text are labeled I-IV. Vertical lines indicate the spectral centers of each feature. (A&B) Spectra from each roughness are compared at nadir and off-nadir (23°), viewing geometries showing spectral changes between samples of varying roughness.

3.4 Discussion

3.4.1 Photogrammetry

3D surface reconstruction indicates that the off-nadir viewing geometry contains a ~5% increase in features <50 μm compared to the nadir viewing angle in both morphologies. Using a Monte Carlo ray tracing model, Warren et al. (2019) demonstrated that increased emission angles result in multiple scattering or view shadowing events. This model works by tracing bundles of rays backward through the system to the emission point. The observed increase in scattering was predominantly seen at emission angles above 50°, and lower angles had a negligible effect on the overall emissivity (Warren et al., 2019). The statistical analysis completed on the sample cross-sections and analyzed in this manuscript provides a better understanding of how this surface interacts with its emitted energy and results in the observed emission spectrum. The higher kurtosis values in the nadir viewing geometry indicate a more leptokurtic (spiky) height distribution, increasing the likelihood of scattering. Additionally, negative skewness values indicate a predominance of "valleys" detected at both viewing geometries. Lastly, the high H value (approaching 1) indicates self-similarity at the μm-cm scale. Combined, these analyses point to an increase in micron-scale surface roughness if viewing a highly vesicular surface from off-nadir geometries.

3.4.2 Thermal Infrared Spectral Effects

Glassy Hawaiian basalts with spectral features similar to those described in section 3.3.2 are thoroughly investigated by numerous authors (Kahle et al., 1988; Crisp et al., 1990; King et al., 2004; Minitti et al., 2007; Abbott et al., 2013; Yant et al., 2016). In Hawaiian basalts, spectral features are typically subdued between ‘a’ā samples and pahoehoe morphologies (Kahle et al., 1988). Spectral features I, II, and IV are attributed to the presence of an accreted silica-rich rind or coating, indicating the samples have undergone some degree of weathering (Kahle et al., 1988, Crisp et al., 1990), with feature I being specifically linked to Al-O vibrations (Crisp et al., 1990). Feature III indicates stretching vibrations within the silica tetrahedra of the glass structures. This feature tends to shift towards shorter wavelengths with age as the glass becomes more polymerized (Crisp et al., 1990). Additionally, features II and III are typically dominant in pahoehoe systems and are indicative of flow age (Kahle et al., 1988). The fact that these spectral features I, III, and IV change in intensity where viewed off-nadir suggest that at off-nadir viewing geometries “see” a more significant amount of weathered silica products, potentially within the vesicle space. Additionally, stronger absorptions between 10 and 12 microns are typical of young pahoehoe with a well-developed chill crust. As these flows age, weather, and devitrify, feature (II) diminishes, and feature III becomes more pronounced (Kahle et al., 1988, King et al., 2004). This explanation provides one possible cause for the observed spectral changes in these samples; however, this hypothesis requires further chemical or thin section analysis.

TIR emission spectra also demonstrate a measurable decrease in spectral contrast between the nadir and off-nadir measurements (Figure 17). Changes in emission angle decrease spectral contrast in both the pahoehoe and a'ā samples (Figure 17 A, B). Here, we interpreted this as an effect of the apparent "roughness" of the sample, and off-nadir viewing geometries appear rougher compared to nadir, especially towards longer wavelengths.

3.4.3 Comparison to Multispectral THEMIS Resolution

Hyperspectral laboratory TIR data were down-sampled to 9-band THEMIS resolution to better understand the effects of micron-scale roughness at a spectral resolution analogous to ROTO data (Figure 18). In addition to the decreased spectral contrast described previously, a slight spectral slope between 7.9 and 12.5 microns became more evident in the simulated THEMIS resolution data (Figure 18 E, F). The pahoehoe sample exhibited a pronounced spectral slope in the off-nadir data compared to the a'ā sample. A similar trend is observed in the nadir data but to a lesser extent. Spectral slopes indicate sub-pixel temperature mixing (anisothermality) below the spatial resolution of the TIR instrument (~1.5cm in the study). Anisothermality can result from either a variation in the thermophysical properties of the surface (i.e., changes in grain size, thermal inertia etc.) or an increase in hot and cold surfaces within a pixel (i.e., sunlit and shadowed).

Before spectral analysis, samples were directionally heated for 30 minutes using a commercial grade heat gun set at 230°C and a 45° angle to the sample surface. To simulate the off-nadir viewing geometry akin to ROTOs, we tilted the samples 23° "sunward" before insertion into the spectrometer. This viewing geometry effectively aligns the warmer surfaces (previously heated) towards the spectrometer window and shadowed surfaces away. Under these viewing conditions, these results indicate that the pahoehoe sample exhibited a greater degree of anisothermality in off-nadir viewing geometries than in nadir. In other words, more cold and warm surfaces were visible within the spectrometer's 1.5cm spot size.

Additionally, the pahoehoe sample has a large topographic depression running the length of the sample, forming the low point between two ropes. This feature may be “shadowed” (cold) from the heat-gun FOV at 45° and within the spectrometer FOV at 23°, which explains the observed anisothermality. In contrast, the a’ā sample exhibited a lesser spectral slope despite its statistically rougher topography. We attribute this to the significant topographic relief of the a’ā sample and hypothesize that at off-nadir viewing geometries, cold surfaces are effectively “shelf-shadowed” from the spectrometer’s FOV.

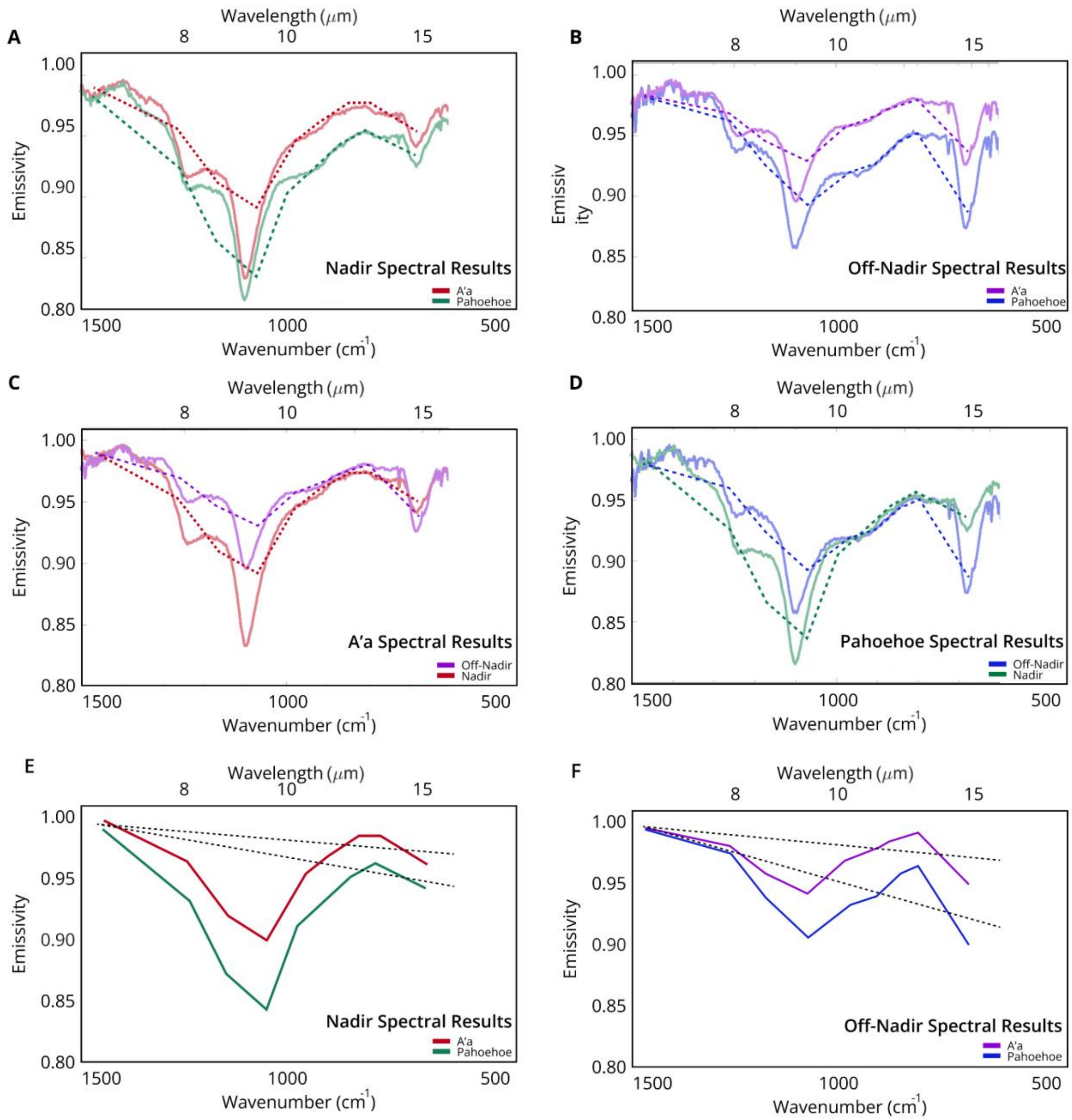

Figure 18. Hyperspectral TIR data reduced to THEMIS resolution. In addition to a change in spectral contrast, lower resolution THEMIS data exhibit a slight spectral slope that went previously undetected.

3.5 Conclusion

Surface roughness on spatial scales below the resolution of orbital data may reveal valuable information about formational processes and subsequent surface alteration on Mars. TIR emission data from THEMIS ROTO observations provide a novel approach to directional emissivity measurements and may improve our ability to quantify surface characteristics such as roughness, rock abundance, dust abundance, and thermophysical properties. However, to do so requires an advanced understanding of how TIR-emitted energy interacts with surface features. The work presented here demonstrates that off-nadir viewing geometries provide a better view of the sides of features or into vesicles/pits. This is apparent by the change in spectral features apparent in the off-nadir emission spectra. Although the scale of investigation in orbital datasets is greater (macro vs micro), I expect that the change in viewing geometry will reveal similar nuances of the surface missed by nadir investigations. Most notably, where investigating the slopes of features such as crater rims or the boundaries between surface units.

High-resolution, digital stereo photogrammetry is fine enough to allow a direct connection with changes in TIR emission data. The decrease in spectral contrast at off-nadir viewing geometries is traced to an increase in µm-scale roughness compared to the same surface viewed from nadir. However, it was not quantified as a function of the viewing angle. Statistical analysis of surface morphology indicates that off-nadir viewing geometry results in an apparent increase in micron-scale features compared to the same surface viewed at nadir. This is due to increased surface scattering and multiple reflections that have a blackbody-like effect on the emitted radiance (Ramsey and Fink; 1999). The degree of change is dependent on the surface morphology.

Additionally, viewing geometry may increase the magnitude of spectral slopes if the change in viewing angle increases the sub-pixel anisothermality. However, at the micron scale, changes in roughness do not necessarily equate to an increase in spectral slope. Further investigation is needed to quantify the spectral slope effect of anisothermal mixing on sub-pixel topography and the role viewing geometry plays.

4.0 Quantifying sub-meter surface heterogeneity on Mars using off-axis Thermal Emission Imaging System (THEMIS) data

4.1 Introduction

TIR observations of Mars by the multispectral THEMIS instrument are used to determine a wide array of surface and atmospheric properties, including surface mineralogy, rock abundance, and thermophysical surface properties, as well as atmospheric dust and water ice contents (Christensen et al., 2003; Smith et al., 2003; Christensen et al., 2005; Bandfield et al., 2004; Fergason et al., 2006; Putzig et al., 2005; Hamilton and Christensen, 2005; Rodgers and Christensen, 2005; Bandfield and Edwards, 2008; Bandfield, 2009; Ahern et al., 2021). Accurate determination of these properties is fundamental to understanding the planet's past and current surface evolution. For example, correct retrieval of the temperature-independent spectral property of emissivity is key to determining surface mineralogy and composition (Bandfield et al., 2004). However, this can require the removal of temperature-mixing effects, which may impart unwanted spectral slopes. Commonly, this involves an assumption of an isothermal pixel-integrated surface temperature within the instrument's instantaneous field of view (IFOV). However, if the corresponding area on the ground contains a surface with units of differing thermal inertias (TI), the assumption of a uniform surface temperature becomes invalid. This can produce an artificial spectral slope that may complicate future compositional analysis. The minimum fraction at which this occurs is currently unknown. However, in general, the greater the temperature distribution, the more prominent these effects appear in the TIR data.

This work combines an off-nadir THEMIS IR dataset, collected by ROTO of the Mars Odyssey spacecraft, with the KRC thermophysical model (Kieffer, 2013) to describe sub-pixel surface units found in the Apollinaris Mons region. Using KRC, we forward model the effects of anisothermality by way of a two-component surface model using units of differing thermal inertias mixed laterally. TIR spectra are sensitive to the degree to which a surface unit remains thermally isolated. This scale is estimated based on the surface's derived thermal inertia, obtained from the THEMIS quantitative thermal inertia mosaic (Bandfield and Edwards, 2008; Fergason et al., 2006).

Due to their unique viewing geometries, we propose that ROTOs allow for a more accurate determination of sub-pixel thermophysical properties than traditional methods, especially in regions heavily mantled by dust. For example, in dusty environments, the high emission angles achieved by ROTOs permit the THEMIS IFOV to observe the less dusty sides of rocks. In contrast, nadir observations only perceive the dust-mantled tops. The difference in temperature between low thermal inertia dust and high thermal inertia rock produces sub-pixel anisothermality that, if successfully modeled, can be used to derive a local rock abundance. Determining the particle size is possible where differences in derived TI values result in temperature separability. The work presented here explores derived TI values ranging from 50 to 2500 thermal inertia units (TIU), corresponding to particle sizes ranging from dust to bedrock, respectively

4.1.1 Study Location

Apollinaris Mons is a volcanic edifice located between the northern lowland and southern highlands. It covers an area ~190 km wide and features a large summit caldera and a 140 km fan deposit that extends to the southeast (Greeley and Spudis, 1981; Robinson et al., 1993; El-Maarry et al., 2014; Chuang et al., 2019). A series of eight new ROTO observations were collected from 18:00h to 19:00h LTST, 38° to 47° L_s, 93° to 102° solar incidence, and surface emission angles from -31° to +33° (Table 1). Images are centered around 174.26° E, -6.40°N and cover an area that includes Apollinaris Mons caldera, extends north into the lower Medusae Fossae formation and south towards Gusev Crater (Figure 1). This ROTO campaign was specifically designed to investigate the surfaces thermophysical properties and Apollinaris Mons was chosen due to the documented presence of rough surface features (Bandfield, 2009; Zimbelman et al., 2010) as well as the contested formation hypothesis of the Medusae Fossae Formation (MFF; Edgett et al., 1997; Tanaka, 2000; Bradley et al., 2002; Hynek et al., 2003; Mandt et al., 2008).

We selected two study areas within the THEMIS ROTO data that exhibit warm pixel temperatures (> 185 K) and rigorous spectral and thermophysical analysis was performed to quantify the degree of subpixel thermal mixing due to variable surface units. Study area 1 is best described as a warm slope associated with a collapse feature in the lower Medusae Fossae formation, just north of the Apollinaris Mons complex (Figure 20).

Table 3. Data specific parameters of the eight ROTO images acquired for this study.

THEMIS Image ID	Roll Angle	Emission Angle	Solar Longitude (L_s)	Local Time (True)
I86177001	-31	35.3	47.0	18.2
I86202001	-24	27.2	47.9	18.3
I85939006	-12	13.4	38.3	18.3
I85964009	-2	2.6	39.2	18.4
I85989005	8	10.2	40.2	18.5
I86014012	18	20.3	41.1	18.6
I86039007	26	29.4	42.0	18.6
I86064009	33	37.5	42.9	18.7

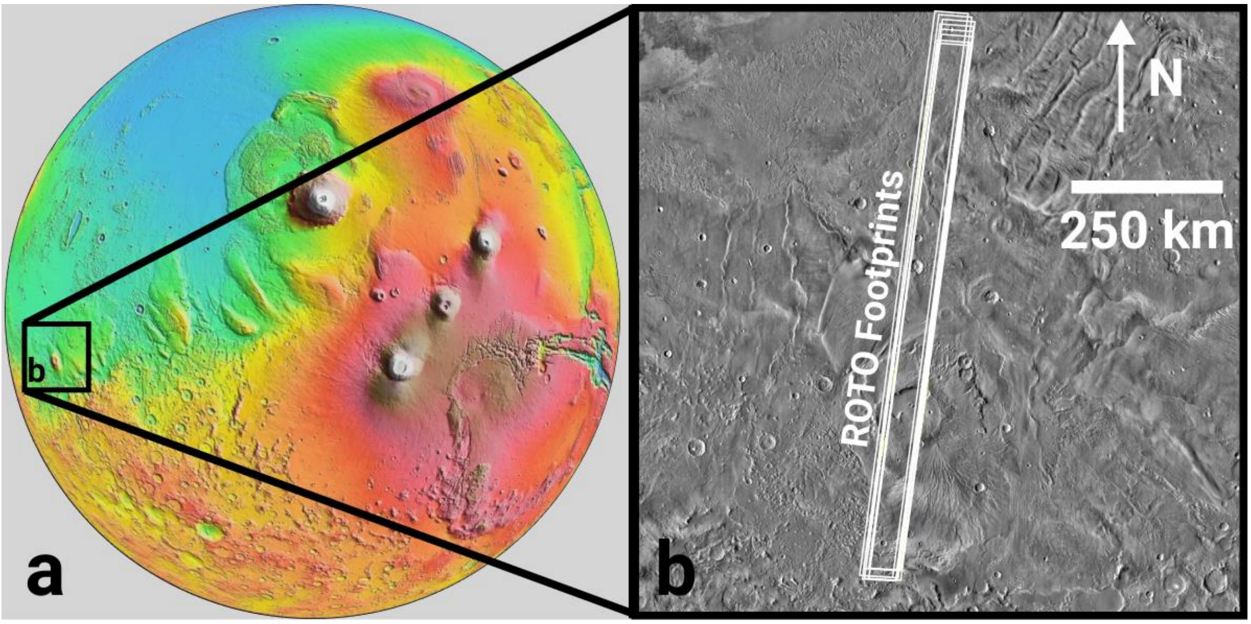

Figure 19. **a) Mars Orbital Laser Altimeter (MOLA) topographic map of Mars showing the location of the study region near Apollinaris Mons. b) THEMIS daytime image mosaic with the March 2021 ROTO footprint shown**

The MFF is a large, equatorially located, Amazonian age, fine-grained deposit stretching from 170 to 240°E. Morphological characteristics within the MFF include yardang fields, collapse features, and layered deposits analogous to large terrestrial ignimbrites (Scott and Tanaka, 1982; Tanaka, 2000; Hynek et al., 2003; Mandt et al., 2008). Study region one is located within a collapse feature just north of the Apollinaris Mons caldera. These features are typically interpreted as the result of subsurface collapse or movement and are commonly associated with the release of volatiles (McColley et al., 2005; Mandt et al., 2008). This area was chosen because it retains surface temperatures above the atmospheric temperature for the entire ROTO observational period. This allowed for a complete surface emissivity analysis at each ROTO emission angle (Figure 20).

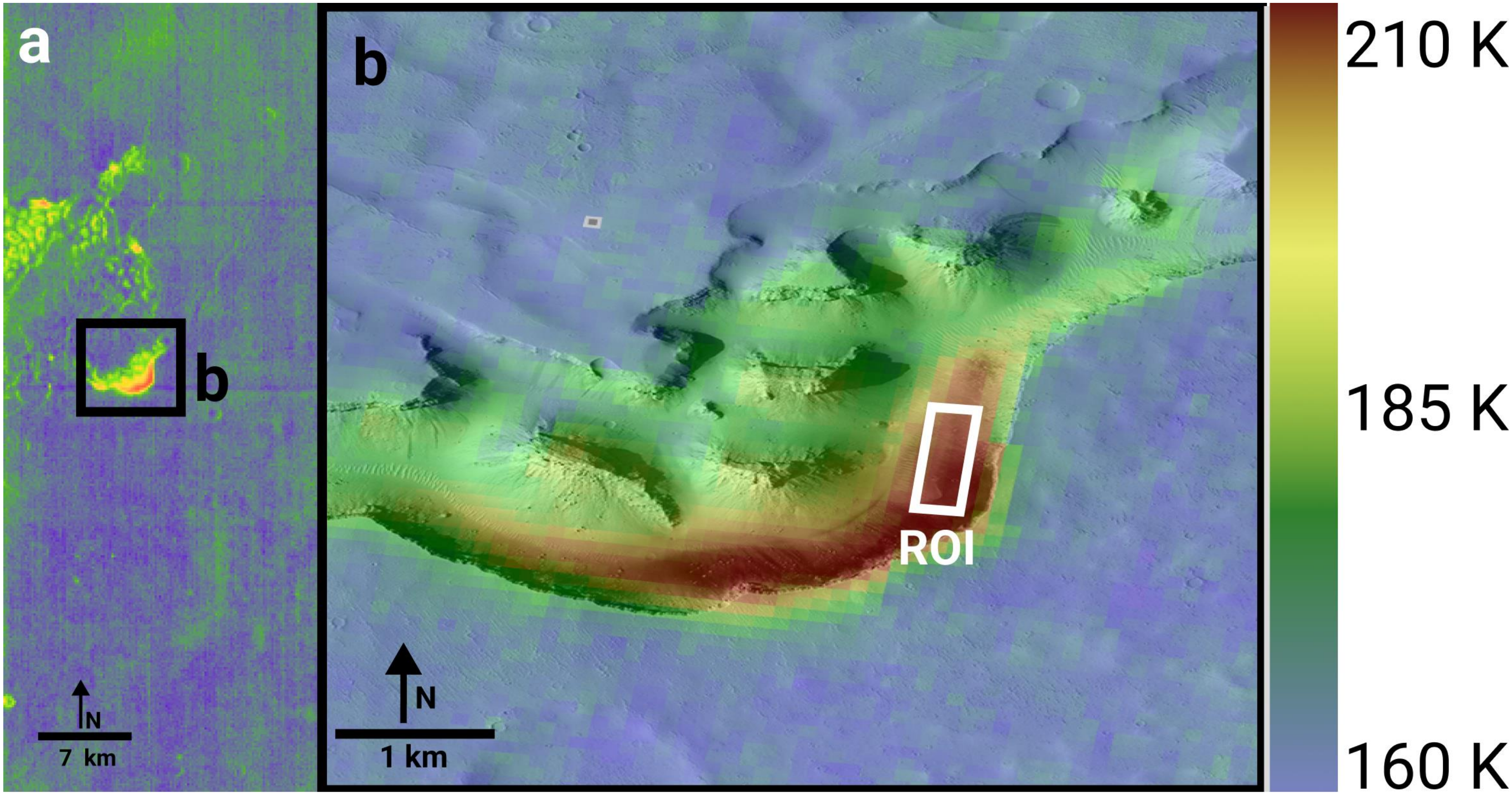

Figure 20. a) Colorized BT image showing study area 1. Higher temperatures are indicated by warmer colors. b) Colorized BT image overlain on HiRISE image ESP_047230_178. The white box indicates the region of interest (ROI) used for spectral emissivity extraction.

Study area 2 is located at the southwestern edge of the Apollinaris Mons fan deposit before it meets chaos terrain. This unit falls within the fan deposit south of the Apollinaris Mons caldera, which is described as rolling plains composed of volcanic material overlain with aeolian deposits (Scott et al., 1993; Chuang et al., 2019). After emanating from a ~2 km wide channel in the caldera rim, the fan deposit covers much of Apollinaris Mons' south flank with a runout distance of ~150 km. Bisecting the fan are numerous channels interpreted as pyroclastic flows, lahars, or other fluvial processes (Gulick and Baker, 1990; Farrell and Lang, 2010; Gregg and Krysak, 2011; El Maarry et al., 2012). Impact craters in the fan deposit display a layered texture on their walls, with some exhibiting rampart ejecta indicating a volatile-rich substrate at the time of impact (Lang et al., 2010; El Maarry et al., 2012). Due to the season, overpass time, and thermal inertia (TI), much of this surface has BT values below 200K. These temperatures generally fall below the atmospheric temperature at this time of day and require the use of BT analysis instead of emissivity. Area 2 lacks the large-scale topographic slopes observed in study area 1 but displays warmer BT than the surrounding terrain (Figure 21).

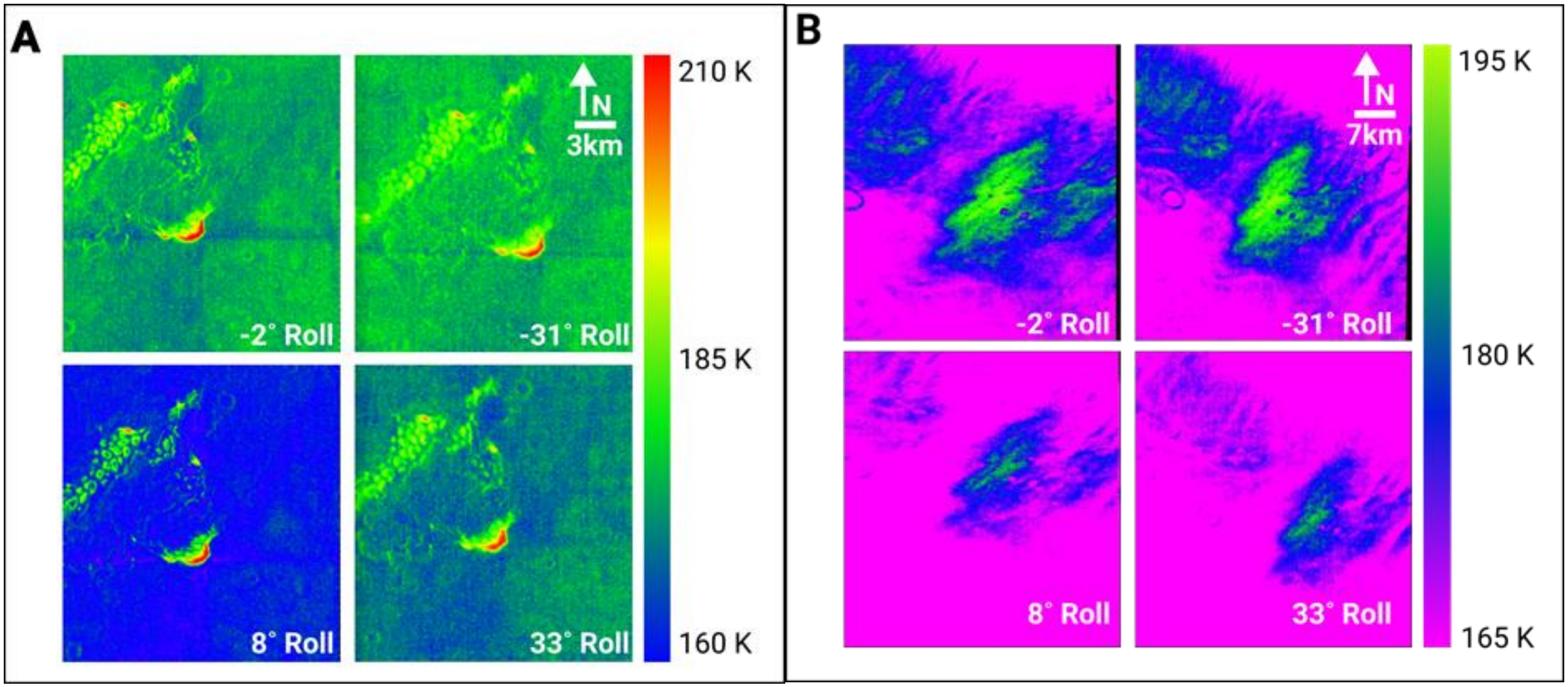

Figure 21. Colorized brightness temperature images at Study Areas 1(A) and 2(B) demonstrate the change in observed brightness temperature as a function of emission angle. ROTOs at rolls of -2º, -31º, +8º, and +33º are shown.

4.2 Methodology

4.2.1 THEMIS Instrument

THEMIS uses an uncooled microbolometer array with nine spectral channels between 6.8 and 14.9 µm. The instrument acquires TIR data at a spatial resolution of ~ 100m/pixel and bandwidth of ~1µm (Christensen et al., 2004). Christensen et al. (2004) and Bandfield et al. (2004) describe the radiometric calibration and associated uncertainties for the THEMIS instrument. A standard THEMIS "4-panel" decorrelation stretch (DCS) image (e.g., Gillespie et al., 1986) set was used to identify regions where dominant spectral slopes are present (Bandfield, 2009; Osterloo et al., 2008). DCS images use THEMIS calibrated spectral radiance displayed in 3 different band ratios and a corresponding surface temperature image (e.g., Bandfield, 2006; 2008; 2009). This process removes highly correlated spectral data, enhancing the color differences between spectral channels. Here, pixels with anisothermal spectra appear as blue or cyan pixels indicating a negative spectral slope (Figure 22).

Where possible, atmospherically corrected surface emissivity spectra were obtained using the methods described in Bandfield et al. (2004). This technique assumes an invariant atmosphere over the study area. It provides a straightforward approach to removing atmospheric emission and scattering by first choosing a region of variable temperature but uniform composition within the

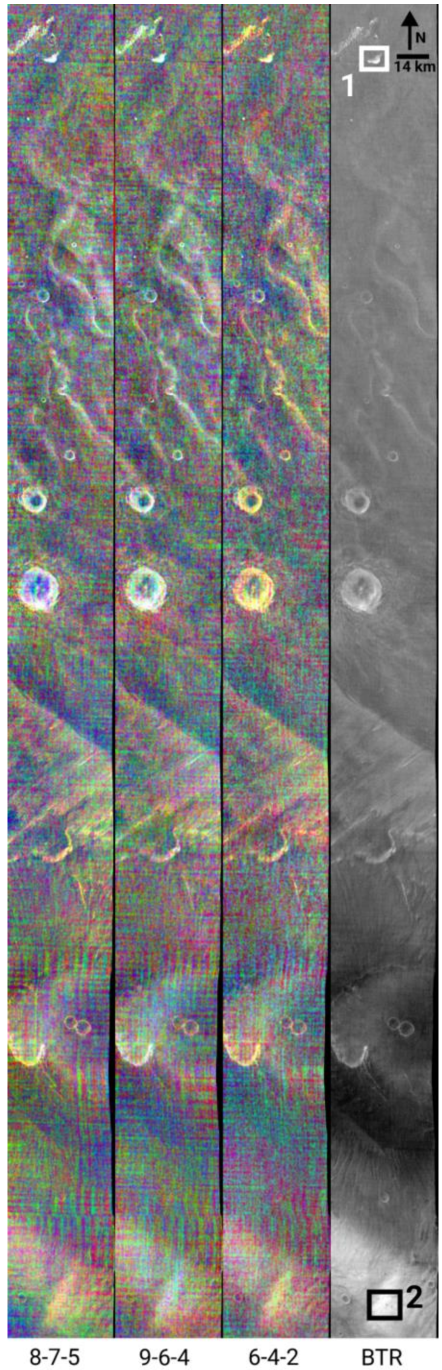

Figure 22. THEMIS 4-panel plot of the ROTO data (ID# I86177001) covering the region north of Apollinaris Mons and centered near 174° E, 8° S. The three left images are DCS images of THEMIS radiance using bands 8-7-5, 9-6-4, and 6-4-2, respectively.

THEMIS scene. To determine surface emissivity, it is first necessary to separate atmospheric dust and ice absorptions from the measured emissivity. Here, this was achieved using the methods of Bandfield et al., (2004). Using the THEMIS DCS, a nearby compositionally homogenous training region was chosen that also contained overlapping TES pixels. TES pixels chosen for the atmospheric correction exhibit a warm surface (≥250 K), clear atmosphere, and are acquired during the same season as the THEMIS ROTO observations (Table 4). Selected TES spectra are averaged and deconvolved with atmospheric dust, water ice and synthetic CO_2, water vapor, the Martian high and low-albedo surface spectrum, a blackbody spectrum and a set of mineral endmembers to obtain linear least squares fit to the measured emissivity (Appendix C) (Smith et al., 2000; Bandfield, 2002; Rodgers et al., 2005). A blackbody spectrum is included in this library to account for differences in spectral contrast between library endmembers and surface spectral components observed with TES. TES emissivity data were atmospherically corrected using spectral mixture analysis to model the TES atmospherically corrected emissivity spectra

Table 4. TES data selection constraints.

Target temperature, K	≥ 250
Emission angle	0-5
Orbit Range (OCK)	3556, 3971, 6109
Total ice extinction	< 0.08
Total dust extinction	< 0.15
Scan length	10

(Ramsey and Christensen; 1998; Smith et al., 2000; Rogers and Aharonson, 2008). The TES-derived atmospheric properties are then removed from the THEMIS data on a pixel-by-pixel basis resulting in atmospherically corrected THEMIS surface emissivity data (Smith et al. 2000; Bandfield and Smith 2003; Bandfield et al., 2004; Bandfield, 2008). However, known emissivity for THEMIS bands 1 and 2 (6.8 µm) cannot be derived as the TES atmospheric endmembers and TES-derived surface emissivity have limited spectral resolution between 7.7-12.1µm. Instead, the methods of Bandfield and Smith (2003) are applied to these bands by removing water vapor and CO_2 hot band absorptions from the previously selected TES emissivity spectrum. The accuracy of this technique relies on high signal to noise with minimal atmospheric dust (< 0.15) and ice (<0.08) at the time of data acquisition.

Since 2014, the Mars Odyssey spacecraft has followed the terminator, allowing for dusk and dawn observations. Although this provides for unique viewing conditions that can accentuate topographic features by illumination at high solar angles, it has created thermal challenges where attempting to accurately measure the surface contribution to the measured radiance. In cases where the atmospheric temperature is greater than the surface temperature, atmospheric emission dominates the radiance spectrum effectively masking surface emission over most of the THEMIS wavelength region. Temperature differences on the surface under these atmospheric conditions can be inferred by examining the brightness temperature differences between wavelengths where the atmospheric emission is minimal. For this study, brightness temperature differences between THEMIS bands 3 (7.93 µm) and 9 (12.57 µm) and from opposing ROTO angles are used.

Brightness temperature is calculated by fitting a Planck curve to channels 3 (7.93 µm) and 9 (12.57 µm), wavelength-dependent brightness temperatures are then averaged over each region of interest (ROI). Band 3 (7.93 µm) was chosen because the atmosphere is relatively transparent at this wavelength and the surface emissivity of most rock-forming minerals is near unity. However, band 3 (7.93 µm) can be noticeably impacted by dust and water ice in the atmosphere (Smith et al., 2003). Band 9 (12.57 µm) was chosen as it contains the highest signal to noise and is also relatively transparent to atmospheric dust. However, the wings of the atmospheric CO2 absorption band may be detected at colder surface temperatures. To accurately predict the effects of sub-pixel heterogeneity on the measured brightness temperature or emissivity, a model forecasting both realistic temperatures is required (Bandfield and Edwards, 2008; Bandfield, 2009).

4.2.2 Modeling Approach

This study utilizes wavelength and viewing angle-dependent differences in emissivity or brightness temperature to separate thermally mixed surface units. To achieve this, we forward model the TIR spectral slopes or band-dependent differences in brightness temperature using a two-component thermal model. Here, we consider rocks as blocks 10cm or greater. This approximation is based on the sensitivity of the TIR spectrum and the separability of diurnal curves of materials with distinct TI values (Figure 5). At the LTST of the ROTO collection, surface units with TI values up to 1250 TIU are distinguishable from one another, whereas TI values from 1250-2500 TIU produced inseparable surface temperatures. On Mars, TI values of 1250 represent particle sizes of 10-15 cm, and TI values of 2500 represent blocks >26cm (Figure 23) (Presley and

Christensen, 1997; Fergason et al., 2006, Nowicki and Christensen, 2007; Bandfield and Edwards, 2008).

Using the KRC model (V 3.5.6, Kieffer, 2013), we predicted surface temperatures for a range of thermal inertia components at each THEMIS ROTO observation used in this study. Model inputs accounted for latitude, longitude, local time, and solar longitude (Ls), albedo, elevation, slope, dust albedo and visible dust opacity at the time of observation. Albedo input values were obtained from a 2 pixel per degree (ppd) TES global albedo map and dust opacity was extracted from the dust climatology database (Montabone et al., 2020) using the latitude, longitude, L_s and Mars year.

The KRC model has repeatedly been shown to successfully model complex surface types and thermophysical properties (e.g., Titus et al., 2003; Armstrong et al., 2005; Kieffer et al., 2006; Fergason et al., 2006; Edwards et al., 2009; Bandfield and Edwards, 2008; Bandfield and Feldman, 2008; Ahern et al., 2021). The model assumes a one-layer atmosphere coupled to the surface with both solar (spectrally gray) and thermal radiation (isotropic and spectrally gray). KRC predicts surface temperatures by solving the heat conduction equation through forward-finite differences. The model accounts condensation and atmospheric pressure variation, downwelling radiation, upwelling radiation, direct and diffuse insolation, an insulating primary layer, and the latent heat of CO_2, if saturation temperature is reached (Kieffer, 2013; Ahern et al., 2021).

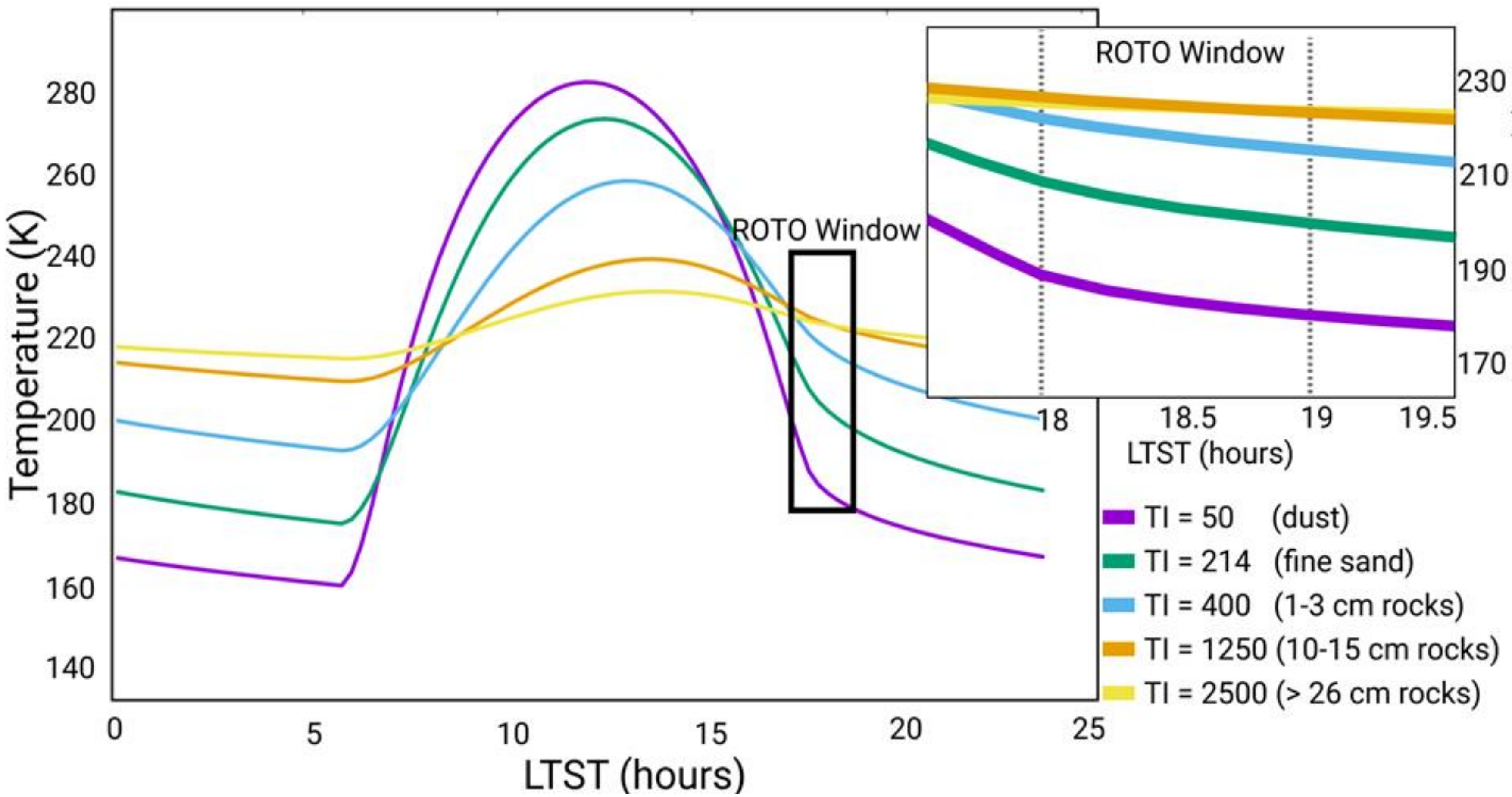

Figure 23. Diurnal curve of different materials with TI values ranging from 50-2500 TIU. Surface units with TI values above 1250 TIU produce temperatures indistinguishable from one another and are inseparable in sub-pixel mixture modeling.

Using the predicted temperatures from KRC, sets of simulated blackbody spectral radiance are calculated for each TI component. Radiance spectra are given "spectral color" by multiplying the radiance values by the TES high albedo surface emission spectra obtained from the Arizona State University (ASU) spectral library and down-sampled to the THEMIS band filters (Christensen et al., 2000).

Assuming that the measured surface emissivity is a combination of surface dust, rock, and sand, radiance spectra are mathematically mixed in combinations of two endmember abundances (90/10, 80/20, 70/30, etc.) to produce a new mixed temperature simulated radiance spectrum. This method is effective as radiance curves of spatial mixtures mix in a linear fashion (Ramsey and Christensen, 1998; Nowicki and Christensen, 2007; Bandfield, 2009; Audouard et al., 2014). Finally, emission spectral slopes were simulated by dividing the mixed temperature radiance spectrum by the Planck radiance at THEMIS band 3 (7.93 μm). This method of emissivity separation is identical to the one applied to THEMIS measured radiance, allowing for a direct comparison (Bandfield, 2009).

If surface temperatures are too cold to allow for accurate emissivity retrieval, brightness temperature is calculated at bands 3 (7.93 μm) and 9 (12.57 μm). THEMIS brightness temperature measured at band 9 is compared to the modeled brightness temperature calculated from the KRC-derived spectral radiance. As band 9 is the most atmospherically transparent, it is considered the closest to the kinetic surface temperature. Here, we use the BT difference between bands 3 and 9 as a proxy for spectral slopes in emission data and an indicator of sub-pixel temperature mixing. Apparent and simulated brightness temperatures are calculated using a look-up table of calculated bolometric Planck radiances. In short, the look-up tables consist of the THEMIS filter functions convolved with the Planck curve (assuming an emissivity of unity). Measured radiance is passed through the look-up table to determine what temperature produces the measured radiance in each band. The highest brightness temperature is assumed to equal the true surface kinetic temperature. The function repeats to determine the emissivity and brightness temperature in the other THEMIS bands (Christensen et al., 2004). Ultimately, surface emissivity modeling and brightness temperature modeling provide a means to estimate the sub-pixel surface unit abundance. Modeled abundance derived from spectral emissivity modeling is the preferred approach as it employs the entire THEMIS spectral range and provides greater leverage of the complete data compared to the brightness temperature approach.

4.2.3 Rock Abundance Modeling

Significant relative proportions of visible (and less dust-covered) rock increase the magnitude of the observed emissivity spectral slopes. In other words, a more considerable ratio of a high TI, rocky surface surrounded by low TI dust produces emission spectra with a steeper spectral slope towards longer wavelengths. To evaluate the effects of anisothermality caused by differences in TI of the surface units, synthetic emission spectra, and brightness temperatures are modeled at each of the observed ROTO viewing geometries. For colder surfaces, the available wavelength possibilities due to atmospheric emission are limited (e.g., area 2), and the simpler two-band brightness temperature model is employed.

Because an object's TI depends on its thermal conductivity, particle size can be inferred from an object's TI value. Lower TI values indicate fine-grained material, whereas higher TI values indicate larger particle sizes (Jakosky, 1986; Dollfus and Deschamps, 1986; Ruff and Christensen, 2002; Fenton et al., 2003; Nowicki and Christensen, 2007; Piqueux and Christensen, 2011; Ahern et al., 2021). At the sub-pixel scale, surface unit discrimination depends on the temperature contrast between those surface units (Cowart and Rogers, 2021). Over the LTST of the eight ROTO overpasses (18-19h), the KRC (Kieffer, 2013) thermal model was used to predict the temperatures for surface units with TI values correlating to Martian dust (50 TIU), sand (214 TIU), duricrust (600 TIU), and rocks of 0.1-0.15 m (1250 TIU) with the estimated TI values for each component taken from Presley and Christensen (1997) and Golombek et al., (2003).

4.2.4 Sensitivities and Uncertainties

Aspects of the TIR measurement and models described here have associated uncertainties and sensitivities. These are presented in Table 2 and described in detail below. Sources of uncertainties in the model include (1) uncertainties in THEMIS brightness temperatures; (2) model sensitivities due to uncertainty associated with the values of various surface and atmospheric parameters (albedo, dust column opacity, etc.), and (3) uncertainties in ROTO viewing geometry (pixel elongation, detection timing, pointing position) (Table 5).

Table 5. Model uncertainties and associated errors. Percent errors are combined using a root square sum (RSS) method as model parameters are uncorrelated.

Precision	*Modeled Sensitivity*	*Percent Temperature Change*
Brightness temperature	1.2 K	6%
Albedo	0.05	0.5%
Dust Opacity	0.09	0.5-1%
Pixel Elongation	1 px	16%
Detector timing	1-2 px	8%
Pointing position	1 px	16%
RSS		15.6%

4.2.4.1 Surface temperature derivation

THEMIS brightness temperature is determined by comparing the scene's radiance with the internal reference calibration flag measured in eight-bit data numbers (DN). This method can produce several factors that complicate THEMIS data calibration and brightness temperature derivation, the most dominant of which is atmospheric gas and aerosol absorptions. Typically, this can result in a 10-15 K underestimation of surface temperatures if viewing a warm surface through a cold atmosphere (Bandfield and Edwards, 2008). We attempt to minimize atmospheric effects by completing a full atmospheric correction of the data. Additionally, the near symmetry of the ROTO produces observations with similar atmospheric path lengths, further diminishing potential atmospheric effects between paired observations (-31 and +33, -24 and +26, etc.).

The absolute calibration of THEMIS nighttime images also produces uncertainties associated with the instrument's internal calibration. Fergason et al., (2006) and Bandfield et al., (2004) offer a thorough discussion of these. To summarize, the uncertainty analysis reported in Fergason et al., (2006) concluded that brightness temperatures are calibrated to a precision of 1.2 K and absolute accuracy of 2.8 K at night (Fergason et al., 2006).

4.2.5 Model sensitivities due to uncertainties associated with surface parameters

To test the sensitivity of the two-component TI model, we chose to investigate the effects of incorrect thermal inertia, albedo, and atmospheric dust opacity on the model results. We used TI values between 50 TIU – 100 TIU in 10 TIU increments and between 800 – 2500 in 100 TIU increments to simulate dust and rock of different particle sizes (Presley and Christensen, 1997). The change in TI from 50 – 100 TIU results in an 11 ± 2 K variation in predicted surface temperature for the fine particle size component. This represents values of 182 – 193 K. Varying the TI of the rock component results in a 6 ± 3K variation in predicted surface temperature from 217-223 K. These new values for high and low TI components are used to assess the associated uncertainties and sensitivity of the two-component mixing model. We calculated model fits using an unconstrained linear least squares fitting analysis to determine the root mean square (RMS) error and median absolute deviation (MAD). As the measured spectra fall within ~0.9 to 1 emissivity, we define significance in the model as RMS error values ≤ 0.03 or 3σ of the standard deviation in RMS error.

At site 1, an increase of 11 K for the dust component does not produce a significant model fit to the measured spectra and results in an RMS error of 0.07 and MAD of 0.05 between the measured and modeled spectra (Figure 24). Variation in the high TI component from 217 to 223 K results in a minimal variance from the modeled results, increasing the modeled RMS error from 0.03 to 0.05. The derived RMS error represents a ±5% distribution of components for each model run. The nadir viewing geometry at study region 1 is an exception, and the associated error is ± 3% of the modeled component ratio.

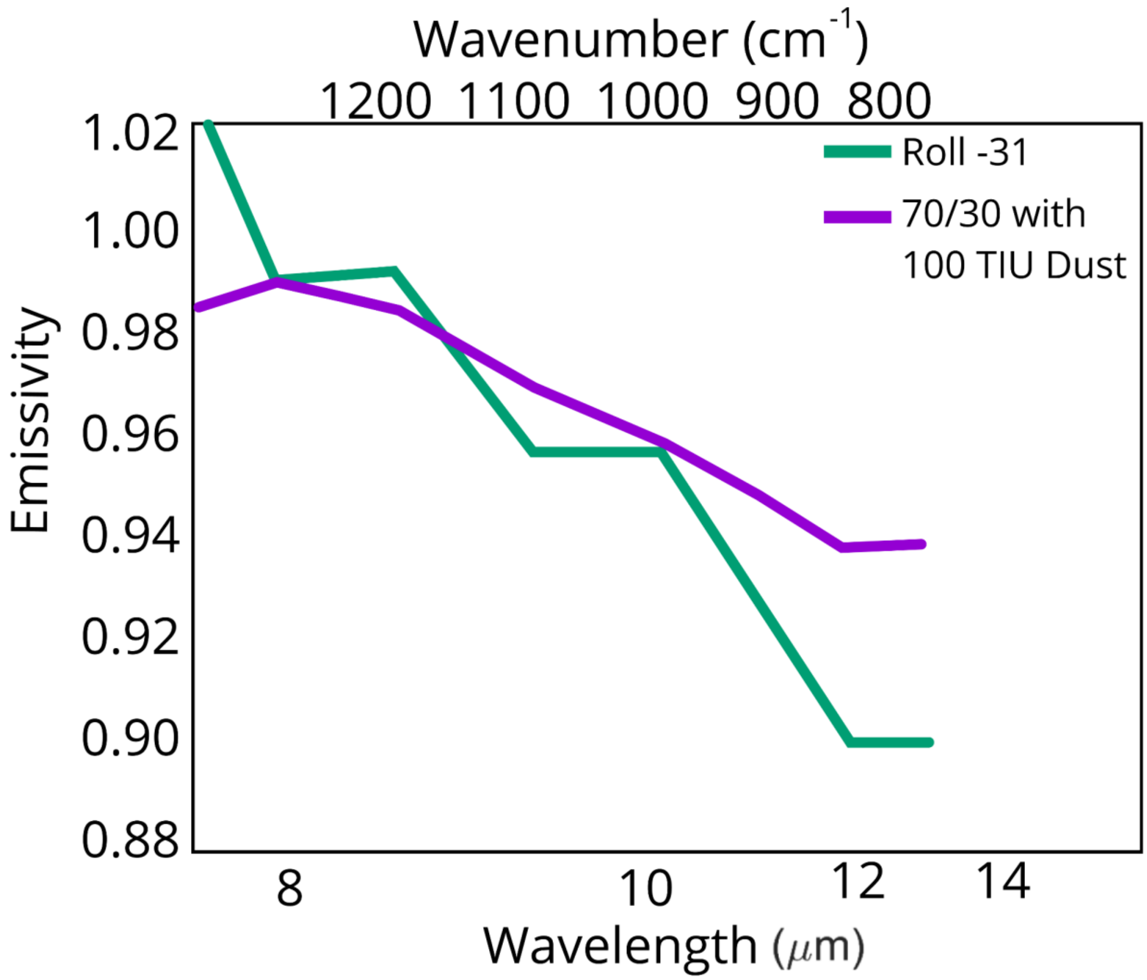

Figure 24. Spectral slope sensitivity analysis using 100 TIU dust in a 70/30 mixture. Changing the TI values for dust from 50 to 100 TIU results in a non-significant spectral slope match.

Where relying solely on brightness temperature differences, variations in the modeled brightness temperature and TI result from small changes in the component ratios for the two-component model. For example, at study site 2, the best model fit was produced using a dust-to-duricrust ratio of 75/25 instead of dust-to-rock, as used in site 1. This mixture resulted in the closest fit to the measured brightness temperature and derived TI (Table 6). However, varying the dust/duricrust ratio by ± 5% results in a modeled TI for the mixture that differs from the THEMIS-derived values by ± 27 TIU and a modeled brightness temperature at band 9 that varied from measured values by ± 5 K (Table 7). Although the difference in brightness temperature between bands 3 and 9 remains relatively low at 3-5 K. This indicates that although effective, rock abundance modeling based on differences in brightness temperature does not provide the same precision in percent cover estimation as spectral slope modeling.

Table 6. Measured Brightness Temperature Results: Study Site 2

Image Id	*Roll (°)*	*B3 Temp (K)*	*B9 Temp (K)*	*Difference (B3-B9) (K)*	*Time (hours)*	*Ls (°)*	*Emission angle (°)*	*Incidence Angle (°)*
I86177001	-31	193.8	191.6	2.2 ±0.2	18.2	47.0	35.3	95.0
I86202001	-24	194.5	191.9	2.6 ±0.3	18.3	47.9	27.2	96.0
I85939006	-12	193.7	190.2	3.5 ±0.4	18.3	38.3	13.4	95.5
I85964009	-2	194.7	191.6	3.1 ±0.6	18.4	39.2	2.6	96.9
I85989005	+8	192.9	187.9	5 ±0.4	18.5	40.2	10.2	98.0
I86014012	+18	192.4	189.8	2.6 ±0.4	18.6	41.1	20.3	99.6
I86039007	+26	192.2	189.4	2.8 ±0.6	18.6	42.0	29.4	100.8
I86064009	+33	192.4	188.5	3.9 ±0.3	18.7	42.9	37.5	102.1

Table 7. Model results from study region 2 show the simulated brightness temperature and thermal inertia for model runs compared to the measured brightness temperature averaged across THEMIS bands 3-9.

Mixture Ratio	*Bands 3-9 Simulated BT (K)*	*Simulated TI (TIU)*
Measured results	193-190 ± 2.8 K	185 ± 12
80/20 dust/duricrust	188-185 ± 3	160 ± 6
75/25 dust/duricrust	190 -187 ±3	187 ± 6
70/30 dust/duricrust	198-192 ± 3	215 ± 6
70/30 dust/rock	215-205 ± 3	410 ± 6
75/25 dust/rock	212-207 ± 3	350 ± 6
80/20 dust/rock	210-205 ± 3	290 ± 6

4.2.5.1 Uncertainties associated with albedo and atmospheric properties

Albedo and atmospheric dust opacity play a less drastic role in predicting surface temperature with KRC. We obtained surface albedo values from the THEMIS VIS-ALB images for the study region. As the ROTO images are collected just after sunset, uncertainty in albedo is relatively high because less time has passed for the daytime albedo effects to diminish. Using KRC, we tested an albedo uncertainty of 0.05, which resulted in a predicted surface temperature of ± 2 K. Overall, this had little to no impact on the simulated emissivity spectral slopes. The associated RMS errors between measured and modeled spectra varied by < 0.002.

Atmospheric dust opacity (TAUD) was obtained from Montabone et al. (2020). TAUD values are obtained from the same Ls and geographic location as the THEMIS temperature data. As this data is a new ROTO dataset collected in Mars Year 36, the Mars Climate Database (MCD) does not yet contain atmospheric dust opacity during these observations. Instead, we used values for Mars year 34. Due to the lack of THEMIS data, IR values are multiplied by 2.6 as recommended by Montabone et al. (2020). Associated uncertainty with atmospheric dust opacity is an average of 0.09 for Mars Year 34 over the Ls of ROTO acquisitions, which are adopted here.

4.2.5.2 Uncertainties in ROTO viewing geometry

Due to the ROTO's unique pointing capabilities, uncertainties in surface footprint size represent the largest source of uncertainty in these observations and model results. To compare surface characteristics at different emission angles, the pixels used in each observation must be statistically similar in surface units, distribution, and physical properties. Changes in albedo, thermal inertia, and areal distribution of surface units between the ROTO measurements due to errors in instrument pointing will have a significant effect on the derived model abundances. Additionally, due to the off-nadir viewing geometry, pixel areas can become elongated, covering more of the surface instead of their typical 100m in nadir data.

I divide errors in surface footprint into two main categories, those related to uncertainty in the timing of the detector and those related to accuracies in spacecraft pointing/orbital position. Errors in detector timing only occur in the along-track direction and result in ± 1-2 pixels of uncertainty which follow a Gaussian distribution. This indicates that most errors are on the sub-pixel to one-pixel level. Inaccuracies in the spacecraft pointing/orbital position result in ± 1-pixel error and occur in both the along-track and cross-track directions. We utilize averaged TIR emission spectra and BT over multiple pixels in the ROIs to reduce the uncertainty in the THEMIS measurement. Pixel elongation introduces the largest source of error and is most dominant at the larger rolls of -31, -24, +26, and +33. Here I estimate that pixel elongation accounts for ~1 pixel worth TIR data are sensitive to the scale at which the facets of surface units remain thermally isolated. We estimate the spatial sensitivity based on the surface's TI. At low TI (<100 TIU), the TIR spectrum is sensitive to features on a scale of ~ 1 cm. At a moderate TI (150-300 TIU), the scale of sensitivity increases to ~10 cm, and at high TI (>800 TIU), the scale is ~1 m (Bandfield and Edwards, 2008). Nighttime thermal emission measurements, on the other hand, provide qualitative information on relative differences in surface particle size, degrees of inundation, and total rock abundance (Kieffer et al., 1977; Christensen, 1986; Fergason et al., 2006, Ahern et al., 2021). After sunset, with solar forcing removed, surface units thermally equilibrate at a rate directly proportional to their TI if thermal diffusion allows anisothermality to exist in the first place. The surfaces studied here have THEMIS-derived TI values between 150-350 J m^{-2} K^{-1} $s^{-1/2}$ (Fergason et al., 2006). This constrains the TIR sensitivity to temperature mixing at the ~10 cm scale, five times smaller than High Resolution Imaging Science Experiment (HiRISE) spatial sampling (54.4 cm/pixel) and a scale previously only accessible by in-situ investigation.

4.3 Results

4.3.1 Surface Emissivity Results

A six-pixel region of interest (ROI) within study area 1 was chosen where the surface temperatures remained well above the atmospheric temperatures in all the THEMIS ROTO images. A consistent negative spectral slope is apparent in the extracted emission spectra from the ROI. Generally, ROTOs with a negative roll angle (-31°, -24°, -12°) show negative spectral slopes of a greater magnitude than those extracted from ROTOs with positive roll angles (+33°, +26°, +18°, +8°), the exception to this is the -2° (e.g., nadir) which displays the lowest magnitude spectral slope. Where comparing emission spectra from complementary ROTO angles (e.g., -31° and +33°, -24° and +26°, etc.), the endmember pairs (-31° and +33°) show the largest difference in spectral slopes, whereas intermediate pairs (-12° and +18°, -24° and +26°) show less of a difference (Figure 25). Where plotted together, the measured emissivity spectra may constitute a continuum of spectral slopes beginning at the -2° roll and ending at the -31° roll. As the spectral slope is directly correlated to the magnitude of sub-pixel temperature mixing within the instrument FOV, this observed range in slopes provides valuable insight into surface conditions at each viewing geometry. Furthermore, it demonstrates that ROTO observations provide a comprehensive view of surface features below the instrument's spatial resolution that would typically require repeat nadir observations over long timescales.

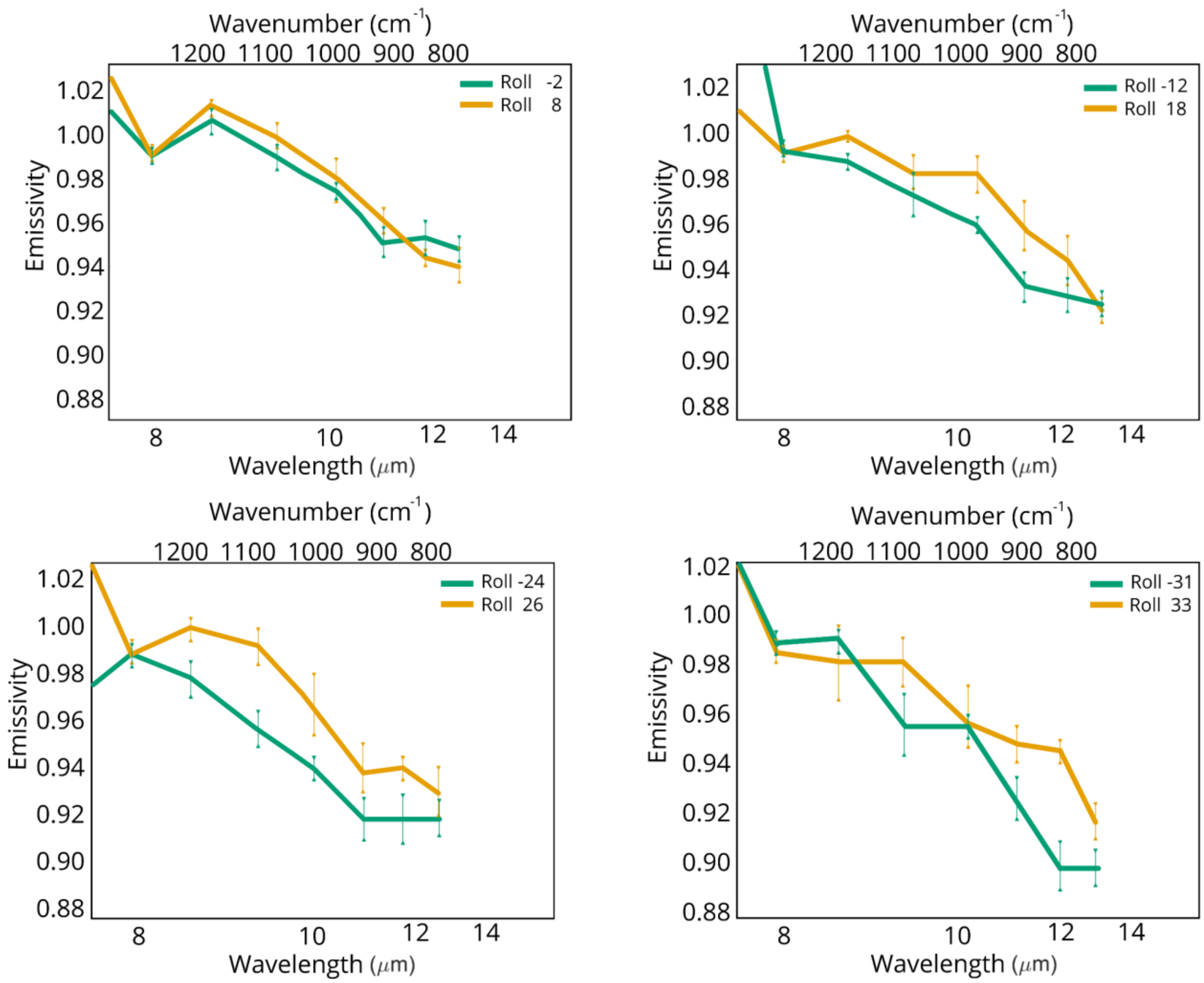

Figure 25. THEMIS emission spectra from each paired ROTO observation acquired averaged over the study ROI in Figure 20. Endmember roll angles (-31° and +33°, -2° and +8°) show the largest difference in spectral slope, whereas intermediate roll angles (-12° and +18°, -24° and +26°) show the smallest difference. Error bars represent the ROI's maxima and minima of band-dependent emissivity.

4.3.2 Brightness Temperature Results

All images used in this study are collected at LTST between 18:00-19:00h with emission angles between 2° and 37°. However, due to the off-nadir geometry of the ROTO acquisitions, the effective phase angle between the solar incidence and emission angles ranges from 59° - 139°. In study area 1, the eight post-sunset observations have temperature asymmetries about the -2° roll angle (effectively nadir), with the lowest temperatures recorded at the highest emission angles (33°, -31°). Negative roll angles favor western-facing slopes and show higher overall temperatures than positive roll angles of a similar magnitude. This corresponds to slopes recently illuminated by the western setting sun. Study region 2 has lower overall surface brightness temperatures than area 1. A maximum BT of 191K at the -31° ROTO roll and a low of 187K at the +8° ROTO roll is observed (Figure 26, Table 6). The ROTO roll angle of +8° shows the greatest temperature difference between THEMIS bands 3 and 9 at ~5K, and the smallest difference is observed in the -31° ROTO at ~2K. At study site 2, differences in BT between spectral channels decrease as the viewing angle moves to the more extreme positive and negative roll angles indicating a decrease in anisothermality at higher emission angles. The opposite is observed in study area 1.

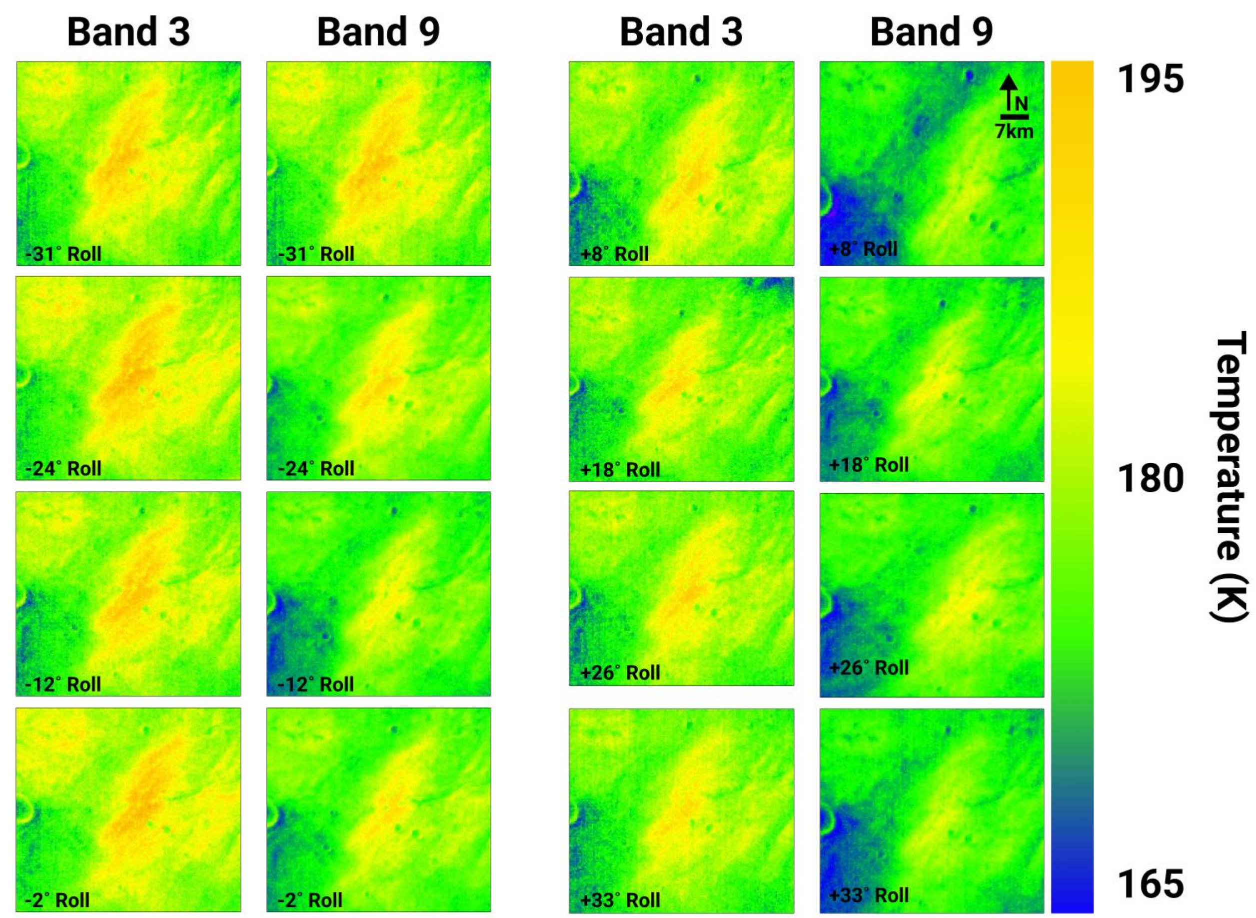

Figure 26. Band 3 and 9 colorized brightness temperature images at Study Area 2 demonstrating the change in observed brightness temperature as a function of emission angle.

4.3.3 Rock Abundance Modeling

Using the methods outlined in section 4.2.3, we analyzed the effects of sub-pixel anisothermality by forward-modeling the emissivity spectral slopes for a range of two-component surfaces (i.e., rock and sand, rock, and dust). The relative proportion of distinctly different surface units is apparent by varying the emission angle. For example, off-nadir emission angles are more effective at viewing the sides of warm rocks mantled or capped by dust. Here, we define "rocks" as objects 10cm or larger with thermal inertia of 1250 TIU or greater.

Where surface units exhibit significant temperature differences, an increase in the spectral slope magnitude is observed (i.e., cold, dusty surfaces, and warm rocks). Sand and dust contributions were varied from 60-95% ± 5% relative to the respective rock and regolith components. The resulting mixed TI radiance spectra are converted to emissivity resulting in sloped emission spectra similar to the observed ROTO emission spectra. Using the resulting synthetic spectra, we create a rock abundance model to represent the distribution of different surface units observed at each viewing geometry.

For site 1, model combinations containing varying percentages of rock (1250 TIU) and dust (50 TIU) produced mixtures that best matched the surface's observed bulk TI and temperature. The simulated anisothermal emission spectra for study area 1 are shown in Figure 27. Emission spectral slope modeling indicates that the higher magnitude off-nadir rolls best match the higher rock abundance models. A rock abundance upwards of 30 ± 5% best matches the higher magnitude emission angles with an RMS error of 0.03 and a MAD error of 0.02. As rolls approach nadir, the observed spectral slope decreases and more closely matches the lower rock abundance model of 5 ± 3% with an RMS error of 0.04 and a MAD error of 0.03. This supports our hypothesis that higher off-nadir emission angles are more effective at viewing the warm sides of dust-capped rocks. Additionally, it suggests that traditional methods utilizing nadir observations to derive rock abundance only account for the presence of 1/6 of the predicted total rock abundance, resulting in a drastic underestimation.

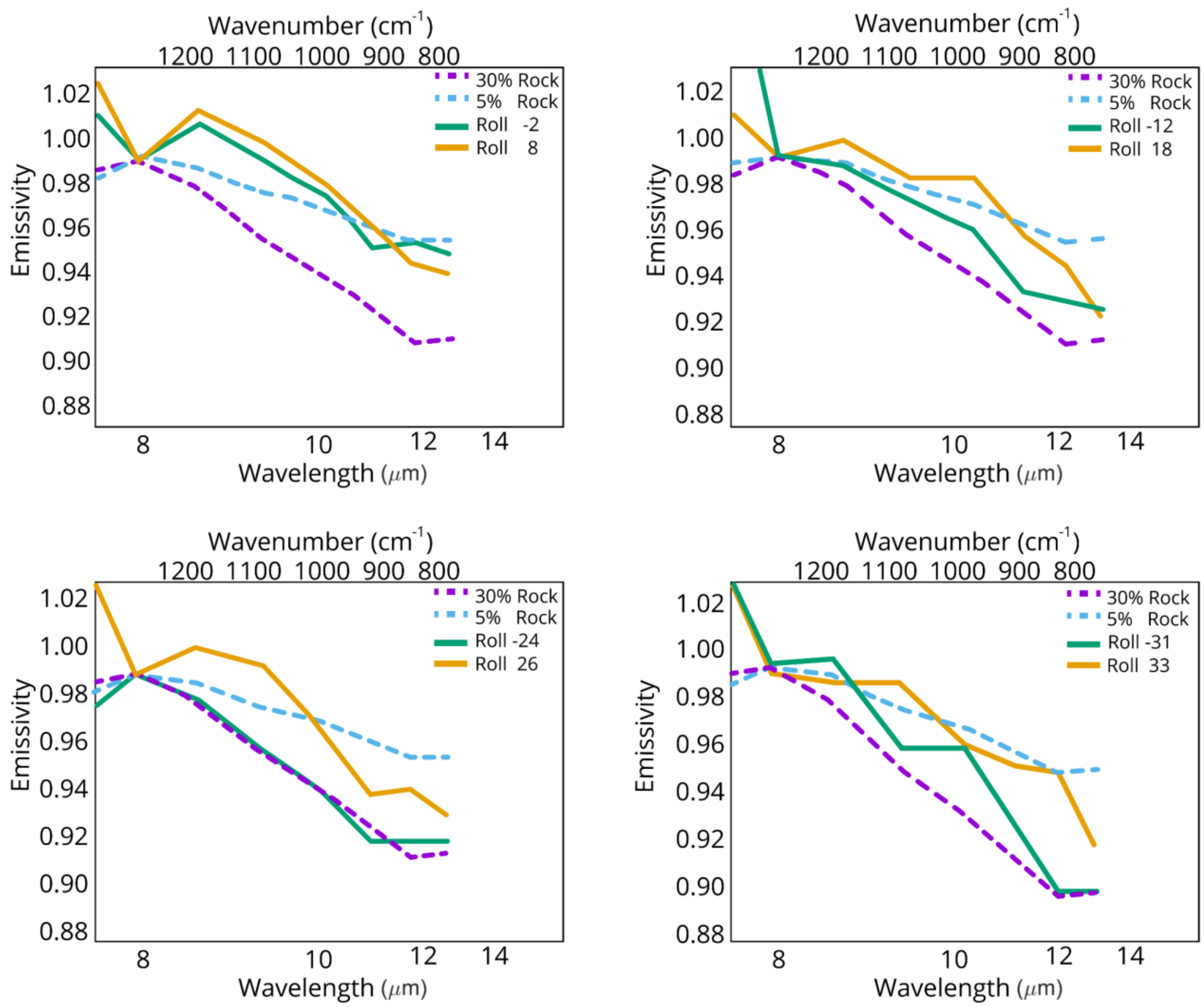

Figure 27. Simulated surface emissivity spectra modeled using the viewing parameters from Study Area 1 listed in Table 1. Spectra for 8 different viewing geometries are shown. An averaged Martian high albedo surface spectrum was convolved with the modeled blackbody spectrum to add "spectral color." The negative spectral slopes are due to differences in temperature caused by varying distributions TI units at each viewing geometry.

As the modeled percentage of rock and dust increases, the modeled spectral slope increases, our modeling predicts that this trend will continue until a maximum temperature difference is reached. Under the ROTO observing conditions, this occurs around 40% rock and 60% dust ± 5%. At this point, the trend reverses, and the modeled spectral slope decreases. At higher rock percentages, the warm rock surfaces dominate the TIR radiance, and the temperature difference between warm and cold surfaces decreases. Emissivity spectral slopes follow the same trend until a modeled surface contains 40/60 ± 5% dust and rock. This distribution of surface units has a nearly identical spectral slope to that of a surface with 90/10 dust and rock ± 5% (Figure 28). However, the modeled apparent brightness temperature and model integrated TI vary for these two surfaces allowing for identification between the two distributions of surface units.

Due to the cold surface temperatures (<200 K), rock abundance is derived at study area 2 using brightness temperature modeling. Results indicate a mixture of low TI (50 TIU) dust and a duricrust-like surface (600 TIU) in a 75/25 ratio. This mixture produces a model-integrated (weighted average) TI of 187 ± 6 TIU, close to the previous THEMIS-derived bulk TI for this region (185 ± 12 J m^{-2} K^{-1} $s^{-1/2}$) from Fergason (2014). The modeled BT range of 190 to 187 across bands 3-9 closely matches the average measured brightness temperature between bands 3-9 of 193-190 ± 2.8 K.

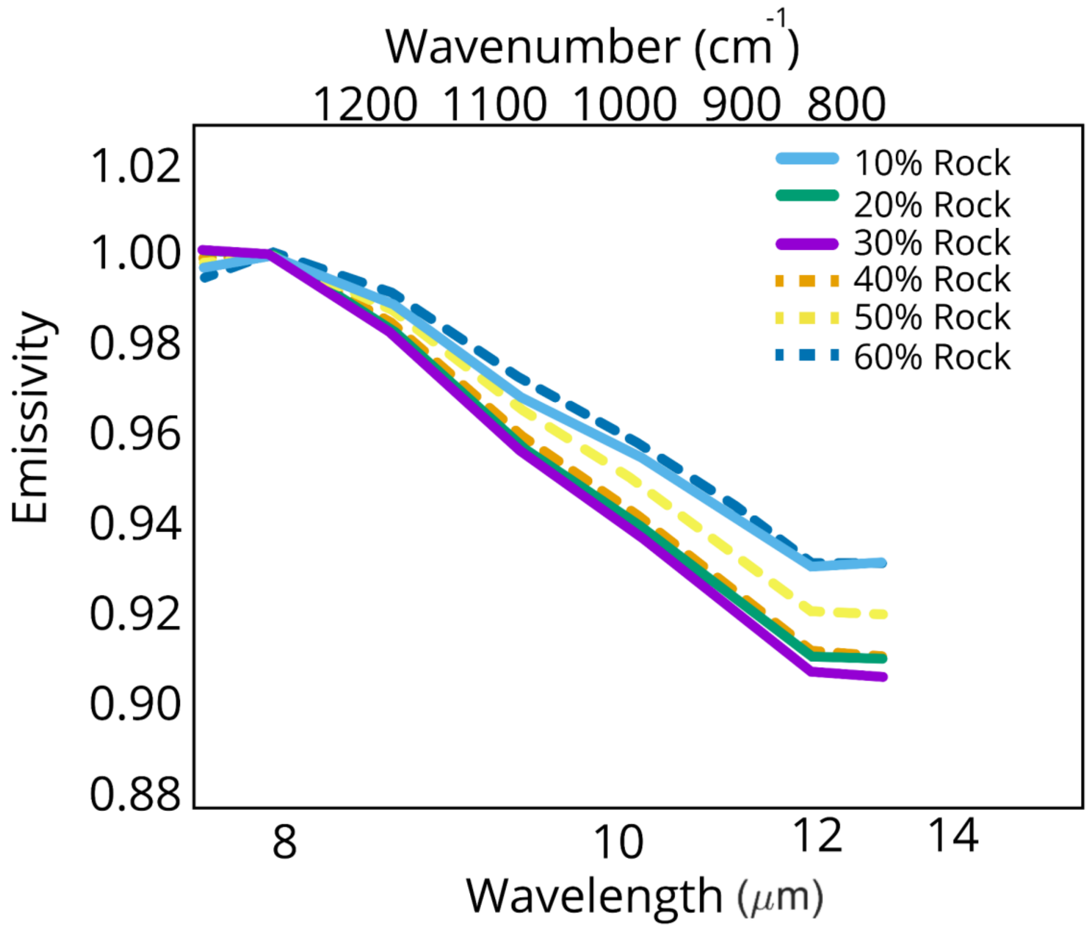

Figure 28. Synthetic emission slopes are created for varying mixtures of rock and dust. Adding a more significant percentage of rock into the mixture increases the spectral slope until a 30/70 rock to dust ratio is reached. After this point, the trend reverses, and spectra become less sloped.

4.4 Discussion

In the post-sunset observations investigated here, we proposed that the observed sub-pixel thermal heterogeneities result from mixtures of surface units with varying TI values that cool at different rates. At night, warmer temperatures represent surfaces dominated by a more significant proportion of higher TI objects (rocks), whereas cooler temperatures represent an abundance of lower TI materials (dust or sand). After sunset, lower TI materials cool quickly, and the higher TI materials retain heat longer, thus creating the observed anisothermality. Moreover, the less-dusty sides of rocks are more apparent where viewed using off-axis observations. Dust coatings, several hundred microns in thickness, can significantly lower TI values of underlying rocky material. This effect is more drastic at dusk and nighttime, where dust quickly cools. Coatings of one diurnal skin depth (~1cm) or greater can completely mask the TI signature of the underlying material (Mellon and Putzig, 2007). Rocks capped with airfall dust may have sides that are relatively dust-free. These sides are warmed by the pre-sunset sun and thus are accentuated in the ROTO data (Figure 29). This is evident by the increased magnitude of spectral slopes observed in the off-nadir emission data and associated modeled higher rock abundance (Figure 30).

Temperature heterogeneities in daytime data due to surface roughness are also shown to produce negatively sloped emission spectra (e.g., Bandfield and Edwards, 2008; Bandfield, 2009; Bandfield et al., 2015). Rough surfaces undergo disproportionate solar heating and self-shadowing compared with smooth surfaces. Both surface roughness and TI differences have similar effects on the TIR spectrum. However, disentangling these effects requires advanced spacecraft observations. For example, precisely timed overpasses where the region of study is observed under illumination and viewing conditions that limit the impact of surface roughness and the emitted radiance is the same regardless of morphology (Davidsson et al., 2015). Lunar work under similar viewing conditions demonstrates that anisothermality due to surface roughness is predominantly limited to high solar incidence angles and not significant after sunset (Bandfield et al., 2015; Warren et al., 2019; Rubanenko et al., 2020).

The work presented here concludes that surface roughness, where likely present, has minimal impact on the emitted radiance. The ROTO observations described here are conducted post-sunset, and the surface is fully shadowed (e.g., Bandfield and Edwards, 2008). Therefore, sloped emission spectra result from temperature differences due to sub-pixel temperature mixing produced by surface units cooling at differing rates as a function of their component TIs.

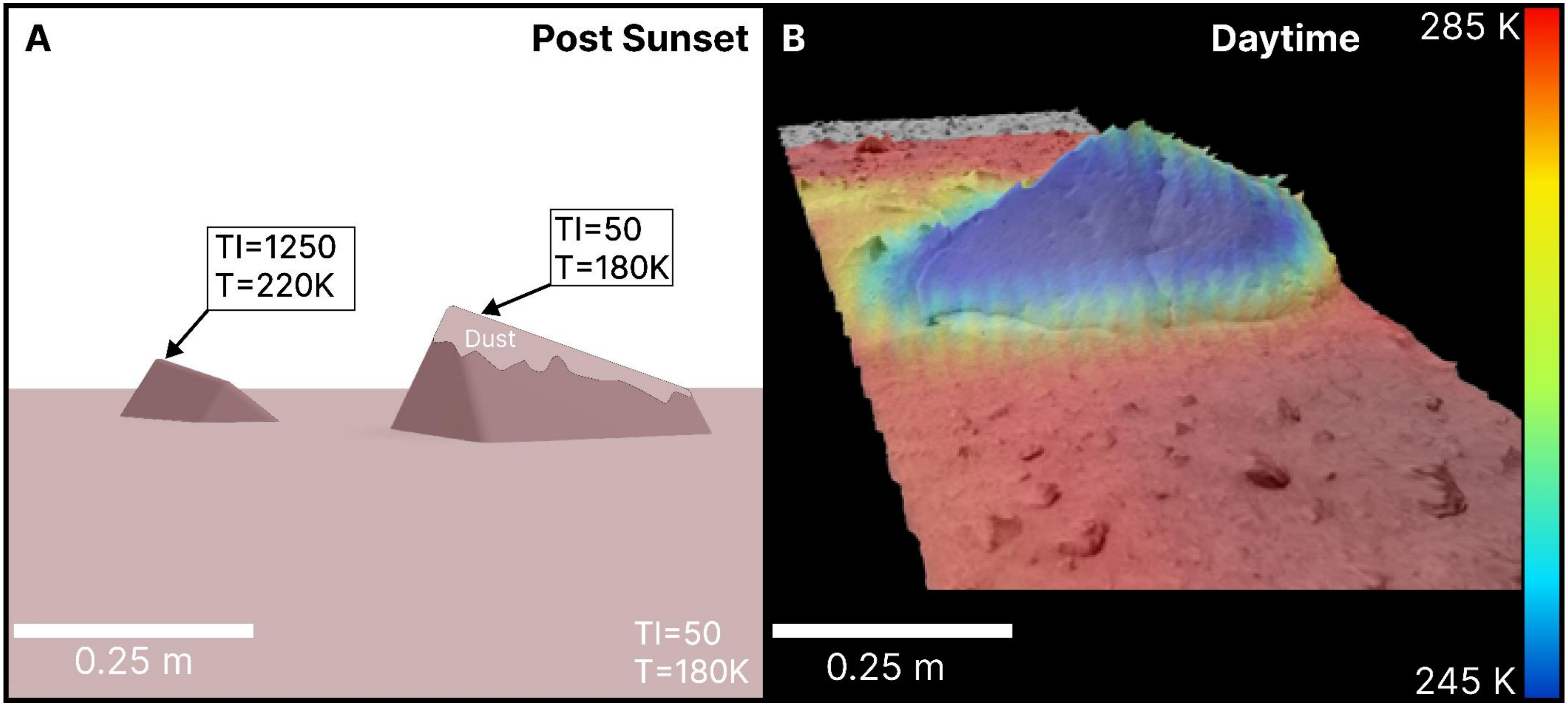

Figure 29. A) Schematic illustration demonstrating the expected temperature differences between less dusty rock sides versus the dust-capped top post-sunset. B) Colorized daytime Mini-TES temperature image from the Spirit rover of the basaltic rock "Adirondack." In daytime observations, high TI materials (rocks) appear colder compared to surrounding low TI materials (Mini-TES image provided by Jeff Moersch and Steve Ruff via personal communication).

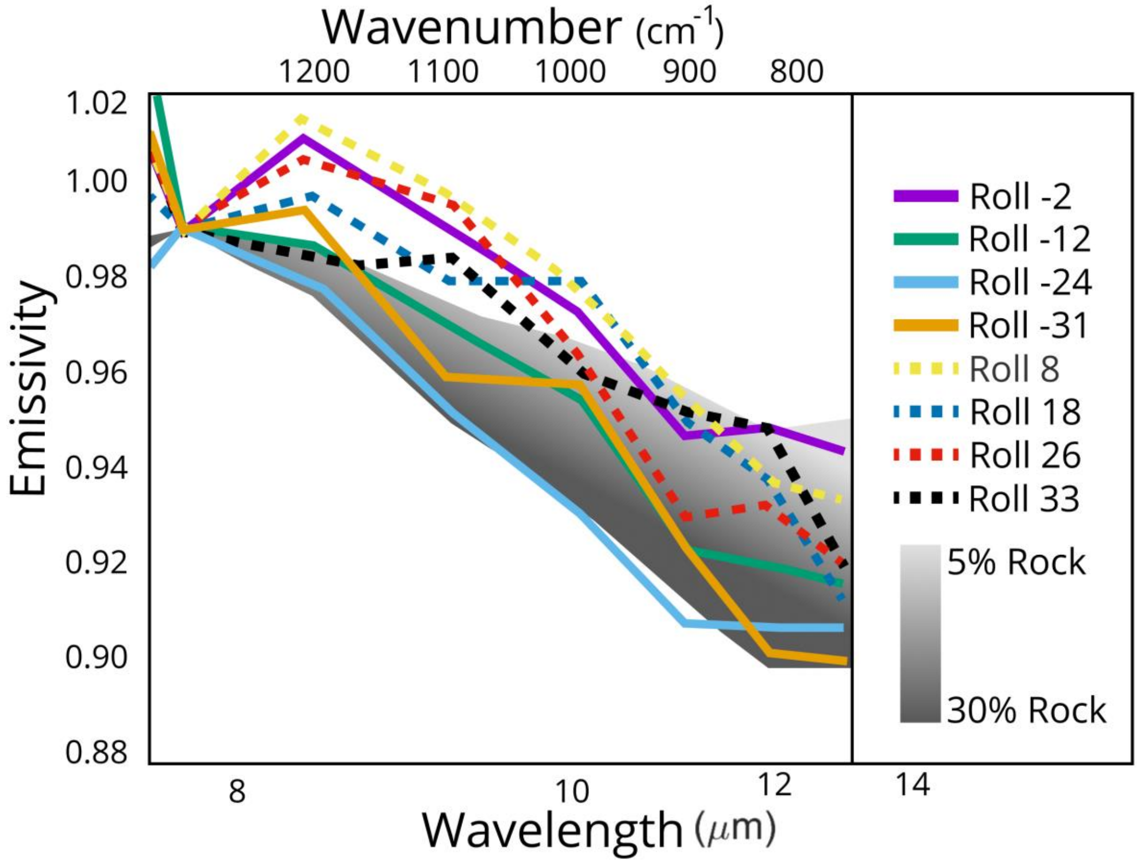

Figure 30. All THEMIS surface emissivity spectra from the collapse feature in study area 1 at each viewing angle. Negative ROTO angle observations are shown in solid lines, and positive ROTO angle observations are indicated as dotted lines. The shaded region denotes the range of spectral slopes equating to the modeled TI mixtures. The variability in spectral slopes is a result of differences in the relative distribution of high and low TI units in the FOV of each observation. Positive rolls generally exhibit higher emissivity, indicating less temperature mixing and a lower modeled rock abundance.

4.4.1 Comparison with previous rock abundance models

The THEMIS ROTO spectral variability observed between each spacecraft overpass is consistent with that of an anisothermal surface, as described by Bandfield and Edwards (2008) and Bandfield (2009). The -31° roll shows the greatest magnitude spectral slope. Spectral slopes decrease in magnitude as the emission angle decreases towards -2°. Spectral slope modeling of the -31° ROTO requires a higher rock abundance of 30% (Figure 30). The variability in modeled rock abundance values compared with viewing geometries indicates that higher emission angles capture a more significant proportion of high TI material than nadir viewing geometries. Prior rock abundance models describe a 3% - 5% abundance of rocks with TI values above 1250 TIU for this study region (Christensen 1986, Nowicki and Christensen 2007), similar to the nadir rock abundance derived here. Based on the increase in THEMIS spatial resolution and novel viewing geometry, we argue that the local rock abundance (objects > 10cm) is likely higher, upwards of 30%, as demonstrated in the modeling of emission data collected off-nadir.

Due to the sensitivity of the TIR spectrum, materials with lower TI values (i.e., sand and duricrust) can be modeled in addition to traditional rock abundance. Brightness temperature modeling at study region 2 indicates a complex surface composed of loosely cemented material mantled by significant amounts of dust. At larger emission angles, brightness temperature differences decrease, equating to a slightly more homogeneous surface. This difference indicates more isothermal conditions at high emission angles and may suggest a greater abundance of fine-grained material or rocky material. At emission angles approaching 0° (Rolls -2, +8), the surface appears more anisothermal, indicated by the greater difference in BT between THEMIS bands 3-

9 (Table 5, Figure 26). ROTO roll +33 exhibits a slightly higher than expected brightness temperature difference between bands 3 and 9 and does not match the expected trend. We attribute this to roll +33's late acquisition time at 18.7 hours.

4.4.2 Comparison to Orbital Data

4.4.2.1 Study Area 1

HiRISE image data of study area 1 shows a possible collapse feature within the lower Medusae Fossae formation (Figure 20). The ROI for this area contains the steep sides of the collapse feature rim along a north-western facing slope. Along the rim of the feature, surface material appears dark with large boulders interspersed, consistent with the modeled higher rock abundance. The floor has aeolian bedforms, indicating the presence of material transportable by the wind.

Due to the collapse feature's north-west slope orientation, ROTO observations with high magnitude negative rolls produce viewing geometries more perpendicular to the surface than those at the -2º and +8º observations. This higher roll angle effectively lowers the emission angle of surface units along the collapse feature slopes. Combined with the higher rock abundance near the features slope, this produces more significant checkerboard temperature mixing, resulting in the modeled higher rock abundance at negative roll angles. The THEMIS-derived TI and modeling results suggest a surface with a fine particle size component (dust-sized particles). However, dunes observed in HiRISE image data suggest sand-sized particles up to 160μm (Figure 31a). This discrepancy may indicate the presence of vertical layering of fine materials (optically thick dust over sand), which may suggest an inactive dune environment.

Large (≥ 163 cm) boulder-sized material is apparent in HiRISE images. In the TIR data, features of this size are indifferentiable from smaller cm size rocks due to the time of the Mars Odyssey overpass. Limits on temperature separability restrict the detection of rock sizes to an upper limit of 0.1-0.15m (Figure 23. However, this represents material well below the detection limit of HiRISE image data but may be represented by the dark material along the collapse features rim and floor (Figure 31b).

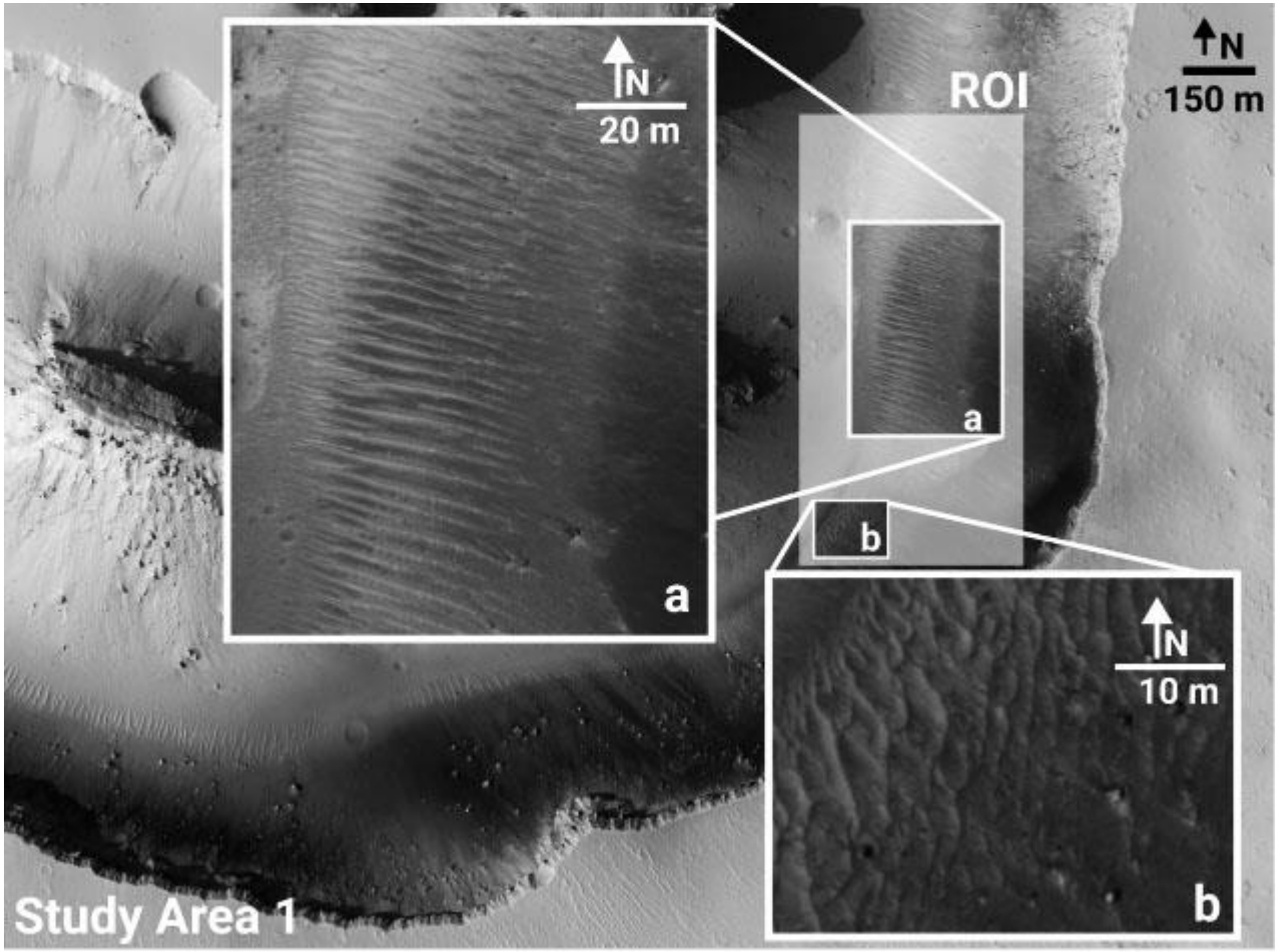

Figure 31. HiRISE image ESP_047230_178 of study area 1 shows the THEMIS ROI footprint in the shaded region. Areas A and B show aeolian bedforms and large boulders interspersed within the ROI, potentially coated by an optically thick layer of dust.

4.4.2.2 Study Area 2

MRO CTX image data of study area 2 reveals a complex surface dominated by impact craters and aeolian material (Figure 13). At the sub-100m scale, the terrain appears mottled with numerous small craters. Aeolian ripples are visible on the floors of some craters and along smoother plains-like terrain. The THEMIS-derived TI values of this region are low (185 TIU), suggesting the presence of abundant fine material at particle sizes of ≤ 100μm (dust to very fine sand, Presley and Christensen, 1997; Fergason et al., 2006). These values are consistent with the result from the TI modeling presented here, which indicates a 75/25 mixture of low TI material (50 TIU, ~1μm) and moderate TI material (600 TIU, poorly cemented material) (Table 7). Based on the endmembers used in the TI mixing model, we interpret this as an aerial mixture of volcaniclastic-like material or poorly cemented rock heavily mantled by dust.

Alternately, crater rims and ejecta blankets are shown to exhibit higher TI values than surrounding terrain (Mellon et al., 2000; Beddingfield et al., 2018). Tight groupings of small impact craters appear to behave similarly and show TI variation as a function of age and degradation (Beddingfield et al., 2021). The numerous small craters and their ejecta blankets seen in study area 2 likely represent a source of temperature variation at the THEMIS sub-pixel level. Impact gardening below the image resolution of CTX (14m/px) may indicate the presence of a larger rock fraction and provides an alternative hypothesis for the observed anisothermality. Distinguishing between these two possibilities would require HiRISE image data for this region.

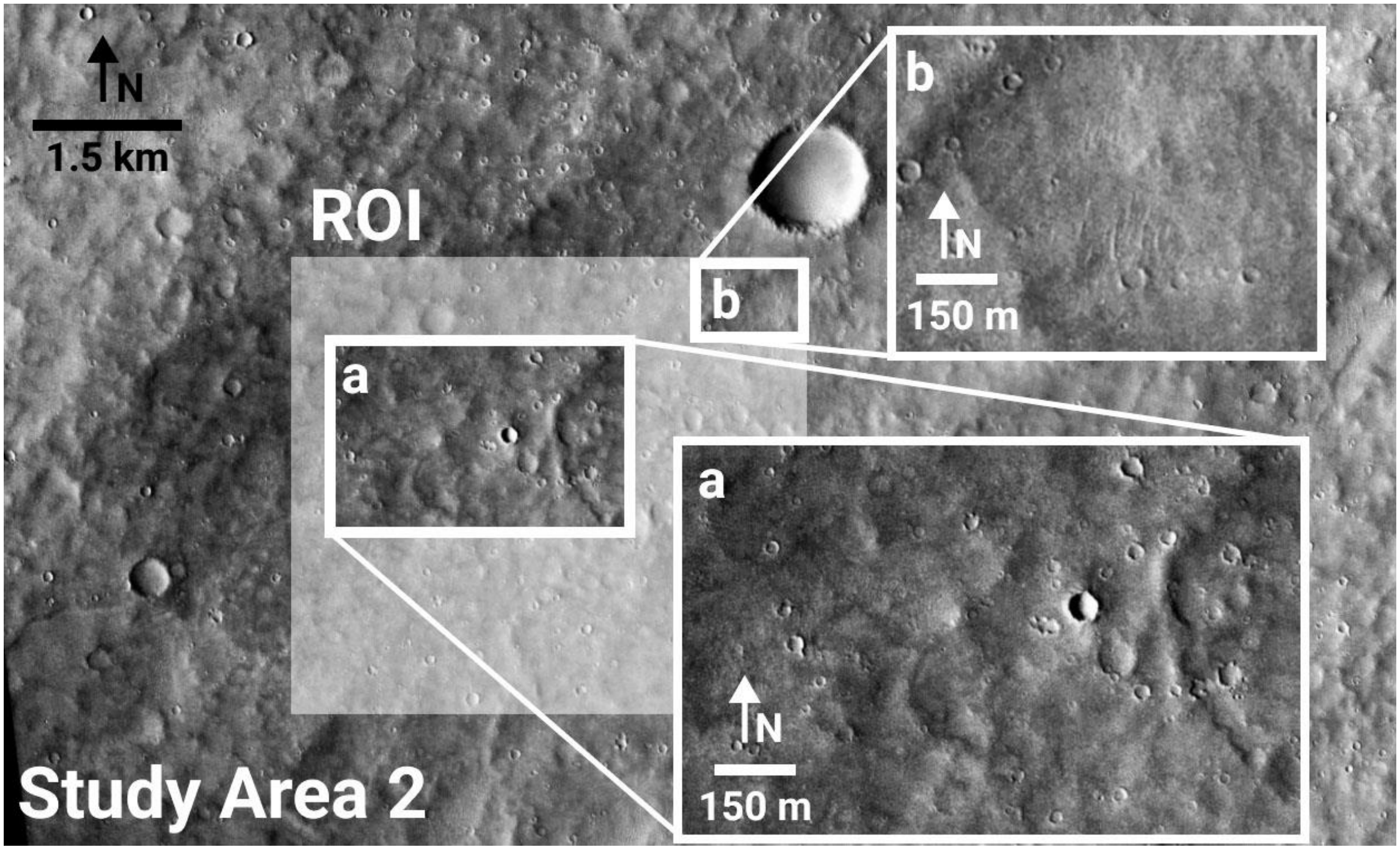

Figure 32. CTX image B05_011653_1714_XN_08S186W of study area 2 shows abundant small craters (a) and aeolian ripples (b).

4.5 Conclusions

Understanding the rock abundance of a planetary surface provides insight into the processes that have shaped it. Additionally, a planet's surface properties directly influence most remote sensing measurements, typically at scales well below the spatial resolution of the data. TIR spectroscopy provides a unique tool to determine sub-pixel surface properties. Surfaces with greater degrees of anisothermality typically have a greater degree of negative spectral slopes. Importantly, where viewed off-nadir, the resulting change in magnitude of the spectral slopes is diagnostic of the spatial distribution of surface units and their abundance. Using off-nadir datasets provides an independent way to validate rock abundance modeling that previously relied only on nadir data. Moreover, the off-nadir data may provide more accurate values by detecting the sides of rocks not as heavily mantled by dust as the upper surfaces imaged by nadir observations.

Although high-resolution visible images directly identify surface rock abundance, THEMIS TIR data provide greater spatial coverage and a quantitative way to extract thermophysical differences from orbital data (Bandfield and Edwards, 2008; Bandfield, 2009, Cowart and Rogers, 2021). For example, the surfaces observed in proximity to Apollinaris Mons show highly variable spectral slopes. Spectral slope modeling at each viewing angle indicates an increasing derived rock abundance with the maximum and minimum viewing angles (-31° & 0°) providing endmember estimates.

Relative rock abundance models do not provide a comprehensive characterization of surface properties. However, in conjunction with high-resolution visible image data and knowledge of the surface thermophysical properties, they provide a means to deduce regolith size, compaction/cementation, and surface unit abundance (Christensen, 1986). Utilizing the instrument pointing capabilities and higher spatial resolution of THEMIS, we estimate a local rock abundance approaching 30% ± 5% compared to 3-5% derived from previous models using nadir viewing geometries (Christensen 1986; Nowicki and Christensen, 2007). The effectiveness of this new model results from the off-nadir viewing geometry. Rocks mantled by optically thick surface dust, as thin as a few hundred microns, experience a reduction in TI, and coatings of dust ~1cm in thickness can completely mask the rock signature. Where viewed from nadir these surfaces do not contribute to the emitted radiance (Putzig and Mellon, 2007). However, off-nadir viewing detects the less dust-covered sides of rocks, effectively revealing high TI targets in an otherwise dusty landscape.

Where atmospheric temperatures exceed surface temperatures, traditional THEMIS IR atmospheric correction is not possible. However, in cases where surface emissivity cannot be extracted due to complexities in surface/atmosphere temperature interactions, a two-point BT comparison provides a valid alternative, albeit at a decreased precision. Brightness temperature modeling at study area 2 indicates a complex surface containing a mixture of dust and duricrust-like material in a 75/25 distribution (Table 7) and is supported by CTX data showing abundant small impact craters. These results and the relatively low TI suggest a heavily dust-covered surface with enough cementation to support crater retention, providing insight into the geologic nature of the volcanic fan unit (Figure 32). The derived TI values support prior hypotheses of an underlying volcaniclastic unit mantled by surface dust (Chuang et al., 2019). Additionally, spectral slope modeling may indicate impact gardening by small impacts (crater diameters < 11m) into the unit.

Unlike study area 1, brightness temperature differences are greatest at the nadir viewing geometry (ROTO -2, +8; Figure 4, Table 4), with more isothermal conditions at higher emission angles. This anisothermal variation indicates that the observed temperature mixing is solely a function of the surface's thermophysical properties and not a result of viewing geometry. Furthermore, it demonstrates the effectiveness of THEMIS ROTO acquisitions in detecting sub-pixel temperature differences from overpasses collected in a relatively short time, compared to using nadir images acquired across multiple local solar times and seasons.

The derived rock abundance estimates enabled by the ROTO measurements are six times greater than previous rock abundance estimates using nadir TIR data. This is due to the fact that off-nadir viewing provides measurements of surfaces not prone to airfall dust cover. This is significant in improving the accuracy of thermophysical and compositional studies. Additionally, the sensitivity of the TIR data is an order of magnitude improvement in scale over radar and visible surface imaging. Finally, the unique aspect of ROTOs provides a novel opportunity to re-interpret a surface, revealing previously undetected features at fine scales. This aids in geologic interpretation and can provide the groundwork for future exploration.

5.0 Applying spectral slope analysis to quantify vertical and horizontal mixing of thermophysically distinct units in THEMIS ROTO data

5.1 Introduction

The textual and geomorphological characterization of volcanic terrains from orbital remote sensing data is essential for understanding a planet's eruption dynamics and vital where ground validation is not possible (Byrnes and Crown, 2022; Shepard et al., 2001; Tolometti et al., 2020; Voight et al., 2021). On Mars, volcanic terrains are one of the most dominant terrain types encountered. Therefore, accurately mapping and characterizing such landscapes can provide fundamental knowledge of the planet's thermal and paleo-environmental conditions. For instance, the final morphology of basaltic lava flows results from the complicated interactions between the lava and the surface upon which it is emplaced. For example, lavas are a temperature-dependent mixture of minerals, liquids, and gases, and the properties of these materials change as the eruption and flows evolve and progress. The behavior of the flows solidifying crust is controlled by its composition and physics, which ultimately plays an essential role in the lava's final morphology. Additionally, lava flows emplaced during different eruptive periods can produce differences in surface roughness closely related to their textural, mineralogical, and petrophysical properties.

However, orbital instruments commonly have spatial scales in the tens to hundreds of meters per pixel, much greater than the degree of surface change observed between different lava flow morphologies and compositions. Furthermore, millions of years' worth of surface processes have weathered, buried, or otherwise visibly impacted flow surfaces, commonly obscuring the underlying flow, which can hinder further compositional or morphological analysis. The study presented here documents the results of a combined approach, utilizing directional emissivity from thermal infrared (TIR) image data and forward-modeling of thermophysical surface properties to determine the relationship between post-volcanic aeolian deposition and cm scale surface features. The generation, transport, and deposition of sediments and regolith (both horizontally and vertically) provide detailed information about how Mars' atmosphere has impacted its surface through aeolian resurfacing.

Previous analyses of lava flows in Daedalia Planum have suggested compositional variability between individual flow units based on observed surface morphology and preliminary analysis of TIR emission data (Ramsey et al., 2016; Crown and Ramsey, 2017). However, significant but variable dust mantling is present, which can alter or mask the underlying flows spectral signature entirely (Simurda et al., 2019). Where this occurs and multiple units are exposed at the surface, spectral slopes can result from temperature differences below the spatial resolution of TIR instrument data. These spectral slopes can be used to derive the thermophysical properties of the surface (i.e., roughness, particle size, and the physical mixing of materials) (Fergason et al., 2006; Simurda et al., 2019; Ahern et al., 2021; McKeeby et al., 2022). This study utilizes THEMIS TIR data acquired during ROTO of the 2001 Mars Odyssey spacecraft to derive the relative abundances of distinct thermophysical surface units in horizontal and vertical mixtures. Due to their unique multi-emission angle nature, ROTO data provide a means to derive the complex mixing scenarios seen in Daedalia Planum.

Using ROTO collected during evening overpasses allows the ground surfaces to be viewed at high solar incidence angles and moderate emission angles. This maximizes the temperature difference between the individual, thermally distinct components and can result in viewing angle-dependent variations in sub-pixel mixtures. Anisothermal spectral slopes are distinct, with magnitudes proportional to the degree of temperature mixing (Bandfield and Edwards, 2008; Bandfield, 2009). Here, we combine rigorous spectral slope analysis and the KRC thermal model to derive sub-pixel horizontal and vertical mixing scenarios and assess their contributions to the TIR spectrum. Surfaces exhibiting subpixel temperature differences are referred to as "anisothermal" and exhibit sloped emission spectra towards longer wavelengths. ROTOs are more effective at capturing sub-pixel anisothermality as they highlight subtle differences in surface characteristics. For example, on a rough surface, higher emission angles allow for the less dusty sides of rocks to be viewed, resulting in a rock abundance model six times more accurate than those relying on nadir data (McKeeby et al., 2022). Ultimately, this work estimates the particle size, observable lava outcropping, and overlying dust thickness on these lava flows young flows. Additionally, it provides insight into the aeolian and depositional environments present within Daedalia Planum, and may aid in future compositional analysis of these flows.

5.2 Background

5.2.1 Study Region

Arsia Mons is the most southern of three large shield volcanoes that form a linear chain within the Tharsis volcanic province. The volcano stands approximately 461 x 326 km across and 17.7 km in elevation with an average 5º slope. Throughout its history, this Arsia Mons has produced some of the most extensive lava flow fields on Mars. The volcano's edifice is built primarily of lava flow material (Mouginis-Mark and Rowland, 2008), ash deposits (Mouginis-Mark, 2002), and glacial deposits (Head and Marchant, 2003). Its summit comprises a single, 110 km wide collapse caldera containing several secondary shield volcanoes arranged linearly (Carr et al., 1977; Scott and Zimbelman, 1995; Richardson et al., 2017).

Expansive lava flow fields originate from the northeast and southwest flanks and surround the edifice. These postdate the central volcanic shield. Down-flow, the southwest flow field forms Daedalia Planum; a basaltic, elevated plains region at the southern margin of the Tharsis province (Scott and Tanaka, 1986; Dohm et al., 2001; Crown and Ramsey, 2017) (Figure 33). On the km scale, Daedalia Planum has a relatively shallow topographic slope ranging from 0º to <0.5º at the southern margin. Geologically, it is composed of complex overlapping lava flows with surface morphologies analogous to terrestrial a'ā and pahoehoe textures (Crown and Ramsey, 2017). At the centimeter to meter scale, these surfaces are described as some of the roughest on Mars based on spectral slope analysis (Bandfield, 2009). Additionally, relatively low crater counts suggest a relatively young surface age (Berman & Crown, 2019). TES-derived albedo of Daedalia Planum is 0.22-0.24, and the dust cover index (DCI) is 0.94-0.97, both indicating a relatively high degree of surface dust cover (Ruff and Christensen, 2002, Christensen et al., 2001, Ramsey and Crown, 2010; Crown and Ramsey, 2017; Simurda et al., 2019). The DCI is a measure of surface dust on Mars identified by a decrease in emissivity below 9 µm (above ~1200 cm^{-1}) TES data. Spectra below ~9 µm experience a pronounced reduction in emissivity due to transparency features in fine particle sizes silicates (see Chapter 2.3). The TES DCI utilizes this emissivity decrease to produce a global map of dust cover in 16 pixel-per-degree resolution (Ruff and Christensen, 2002). However, despite the high DCI values for Daedalia Planum, CTX and HiRISE image data suggest the presence of distinct lava outcrops with minimal dust mantling visible below the pixel resolution of THEMIS (Crown and Ramsey, 2017; Simurda et al., 2019).

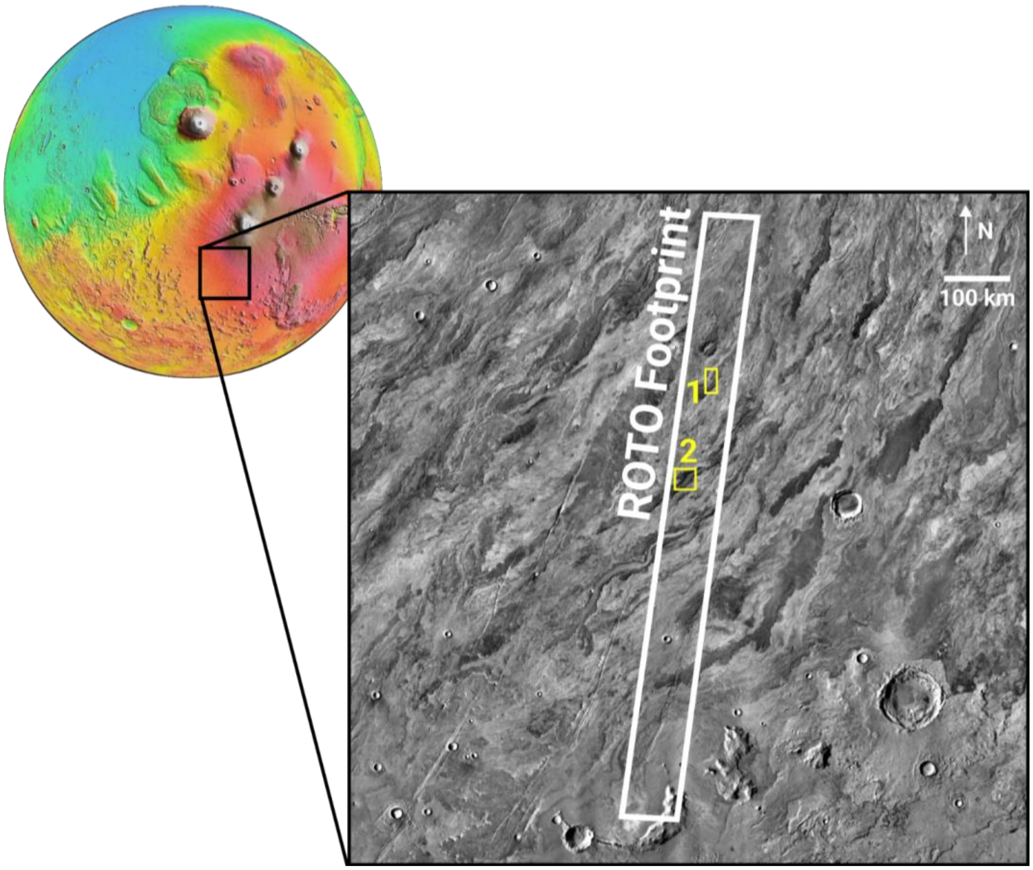

Figure 33. THEMIS daytime thermal IR brightness temperature image with the outline of the ROTO footprint shown in white. Study sites 1 and 2 are shown in yellow. The Mars Orbital Laser Altimeter (MOLA) colorized globe is shown to the left, with the study region denoted by the black rectangle.

5.2.2 Spectral Slopes and Anisothermality

Anisothermality is defined as the horizontal variation in surface temperature below the pixel resolution of an instrument. Anisothermal scenarios can arise from variations in shadows on a rough surface and checkerboard mixing of distinct thermophysical surface units (Nowicki & Christensen, 2007; Bandfield & Edwards, 2008; Bandfield, 2009; McKeeby et al., 2022). Where anisothermality occurs below the pixel resolution of a TIR instrument, the resulting TIR emissivity spectrum can become sloped as the combined radiance of different temperature objects no longer match that of a single blackbody radiance curve. In THEMIS data, this manifests as negatively sloped emissivity spectra that vary with emission angle and differences in brightness temperature with respect to wavelength (Bandfield et al., 2015). Here we utilize a set of multispectral THEMIS TIR observations acquired through ROTOs of the Mars Odyssey spacecraft, rolled about the along-track axis, to investigate the mixing of thermally distinct surface units. ROTOs produce sets of TIR image data where the relative proportions of surface units vary as emission angle changes (Figure 34). Thermophysical modeling of these datasets allows for quantitative analysis of thermal mixing by forward modeling the resulting spectral slope (McKeeby et al., 2022).

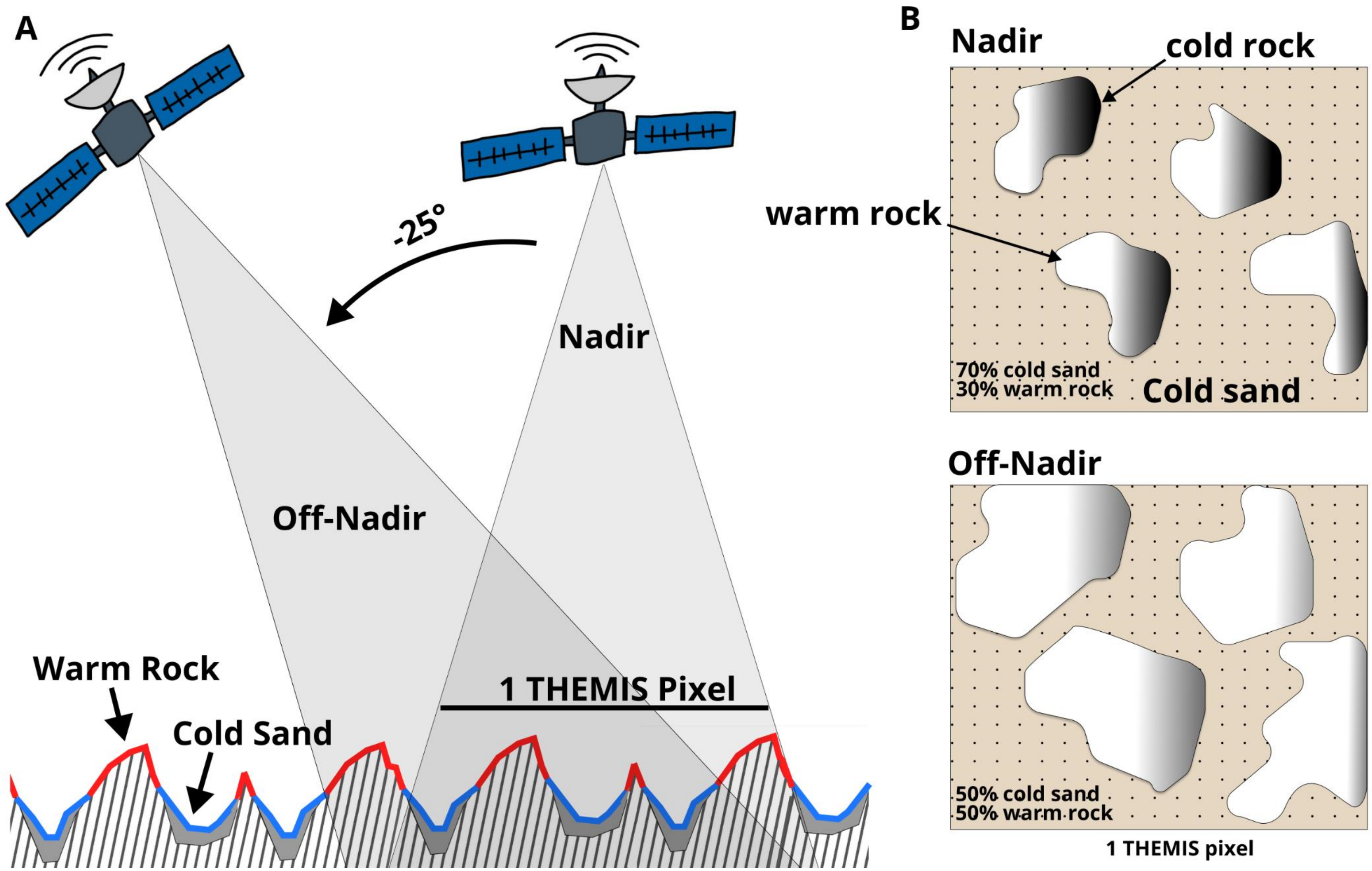

Figure 34. Schematic demonstrating how ROTOs affect the THEMIS instrument's viewing geometry and the expected change in the relative proportion of thermally distinct surface units. B) Cartoon schematic showing the relative proportions of cold sand and warm rock in each viewing geometry.

5.2.3 Previous Work

Ramsey and Crown (2010) and Crown and Ramsey (2017) completed a combination of image processing techniques and geomorphic analysis to investigate the applicability of TIR data analysis in the northeast Daedalia Planum region. Crown and Ramsey (2017) divided flows into two broad categories, bright, rugged lava flows and dark smoother lava flows, based on albedo differences and surface morphology distinguishable in CTX image data and THEMIS temperature data. Three-band DCS stretches using band combinations of 8-7-5; 9-6-4; and 6-4-2 highlighted differences in spectral emissivity related to dust cover and flow composition. Their work concluded that the variable thermal emission from flow surfaces results from a complex relationship between surface roughness, dust, albedo, and the underlying lava composition. On an individual scale, flows exhibit unexpected diurnal temperature variations between neighboring lava flows (Ramsey and Crown, 2010; Simurda et al., 2019). Simurda et al. (2019) took this classification further, separating flows into four categories based on their diurnal response, apparent brightness temperature, and TI value. They concluded that, locally, individual flows exhibit vertical layering of dust and sand with a linear mixture of rock, sand, and dust. My work deals with a localized region of Daedalia Planum containing only a subset of the flows Simurda et al. (2019) categorized. As such, only flow types B-D are discussed. Category A flows are not addressed as they were not contained within the ROTO footprint.

Briefly, as defined by Simurda et al., (2019), category B flows display the most significant change in temperature over the diurnal cycle and exhibit high daytime and low nighttime temperatures. These flows' rapid heating and cooling rates suggest a surface dominated by fine particles. Category B flows were avoided due to their diurnal response, which potentially reflects high degrees of dust mantling (Simurda et al., 2019) and a lack of available HiRISE image data. Category C flows exhibit an inverse temperature relationship to category B flows, slightly higher derived TI values and a lower diurnal temperature variation. This indicates a more significant proportion of exposed high TI material than category B flows.

Category C flows contain low daytime derived THEMIS BT, high nighttime THEMIS BT, and higher TI values. They exhibit the least variation over the diurnal cycle, low heating and cooling rates, and therefore may contain higher areal distributions of lava outcrops than sand (Figure 35A) (Simurda et al., 2019). Lastly, category D flows have little diurnal temperature response relative to the flow field and have consistently low daytime and nighttime THEMIS BT values. They exhibit a daytime temperature response of a complex surface that Simurda et al. (2019) contribute to an increase in larger block sizes and an increase in fine materials, limiting the temperature at night (Figure 35B). The percentage of lava outcrops is considered higher than sand and dust but less than category C flows. These flows exhibit consistently lower brightness temperatures throughout the sunlit hours. The authors attribute this to a complex surface containing a more significant percentage of lava outcrops than fine material, but less abundance than category C flows (Simurda et al., 2019).

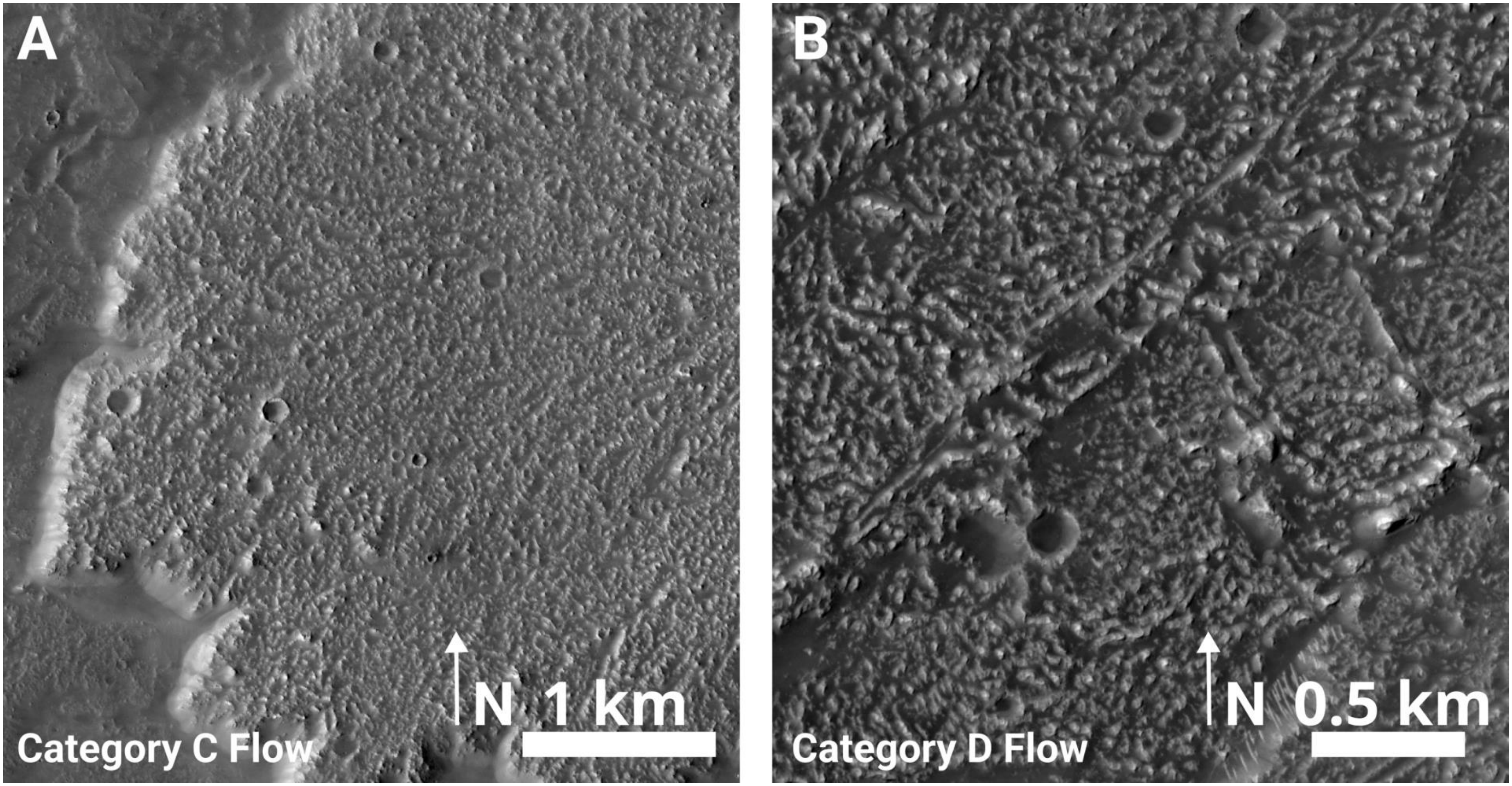

Figure 35. HiRISE image data (PSP_002711_1550, ESP_042006_1570) showing category C (A) and D (B) flow morphologies as defied in Simurda et al. (2019).

5.2.4 THEMIS-Derived Thermal Inertia

Thermal Inertia is an invaluable aid in understanding the surficial geology and surface processes on Mars that are potentially active today. THEMIS-derived TI consists of the highest spatial resolution thermophysical data currently available for Mars (100m/pixel) and can be used to quantify surface physical properties such as effective particle size. Under Martian atmospheric conditions, geologic materials' density and specific heat vary by a factor of ~3, whereas its conductivity varies by 3-4 orders of magnitude. This means that conductivity has a much stronger influence on the derived thermal inertia. An object's bulk conductivity is a function of its solid, radiative, and gas conductivity. Due to the relatively low surface temperatures on Mars, radiative conductivity is negligible. The contribution to bulk conductivity by gas is controlled by particle size and pore size relative to the mean free path within the pore spaces, which are inversely proportional to its density (Presley and Christensen, 1997, Fergason et al., 2006). This results in a strong relationship between TI and particle size, assuming an unconsolidated homogeneous unit.

Where calculating thermal inertia, the brightness temperature of the surface is determined by fitting a Planck curve to THEMIS band 9 (12.57 µm). Band 9 is chosen as it is relatively transparent to atmospheric dust and has the highest signal-to-noise ratio (Christensen et al., 2004; Fergason et al., 2006). THEMIS Band 9 temperatures are then converted to thermal inertia by interpolation with a 7-dimensional look-up table (latitude, season, local solar time, atmospheric dust opacity, thermal inertia, elevation, and albedo) generated in KRC (Kieffer, 2013). Interpolation is performed on a pixel-by-pixel basis based on the user defined inputs of season, latitude, longitude, and local solar time. Here, I utilize the published THEMIS-derived TI maps to constrain the average TI of the sub-pixel mixing model.

5.2.5 Skin Depth

Thermal skin depth describes the depth to which thermal energy penetrates the surface layer or material. Typically measured on either the seasonal or diurnal scale, it is generally considered the depth at which the temperature is equivalent to 1/e or ~37% of the surface value. Skin depth is proportional to the thermal inertia of the material and the orbital or diurnal period of the planetary body. For instance, a low inertia material with low thermal conductivity will exhibit a smaller skin depth and a larger variation in diurnal temperature than a high thermal inertia material (Jakosky, 1979). Skin depth is defined by the equation:

$$S = \sqrt{kP/\pi\rho C_p} \qquad \textbf{Equation 10}$$

Where k is the thermal conductivity, P is the orbital or diurnal period, ρ is bulk density, and C_p is the specific heat capacity at constant pressure (Jakosky, 1979; Putzig and Mellon, 2007; Biele et al., 2019).

Where viewing a surface from orbit, the surface temperature within an instrument's FOV is controlled by the mixture of its different surface units. If those units are distributed (either laterally or vertically) on scales less than a thermal skin depth, then the average TI and surface temperature will differ from that of each endmember component. Where this occurs at detectable scales, each component may behave differently relative to one another, and the resulting radiance will act as a composite of each component based on the fraction of their abundance (Jakosky, 1986; Putzig and Mellon, 2007). The surface temperature observed from a spacecraft acts as a composite mixture based on the spatial scale of the observing instrument (~100km for THEMIS). Additionally, the vertical scale depends on the material's thermal skin depth, a few decimeters - meters depending on the surface's thermophysical properties (Jakosky, 1979; Putzig and Mellon, 2007).

5.2.6 Dust cover

The TES Dust Cover Index (DCI) for Daedalia Planum is considered moderate to high (~0.95), indicating that some degree of dust mantling is likely for the region (Ruff and Christensen, 2002). This presents a complication for TIR spectroscopy as surface dust can alter or obscure the radiance from the underlying surface. At THEMIS wavelengths, Martian dust is relatively featureless and only contributes a slight spectral slope between 8-12 μm (Bandfield and Smith, 2003; Bandfield, 2009). Regardless, coatings of dust as thin as 10 – 20 μm have been shown to significantly reduce the underlying layers' spectral contrast and brightness temperature (Johnson et al., 2002; Putzig and Mellon, 2007). Previous work by Crown and Ramsey (2017) proposed that dust layering in Daedalia Planum may not be thinner than previously estimated or spatially heterogeneous. Simurda (2019) investigated this further and reported 200 μm dust coatings on individual lava flows based on their recorded diurnal temperature fluctuations.

5.3 Methodology

A THEMIS ROTO triplet and THEMIS daytime image were used in this study. The ROTO triplet was collected in September 2017 at local times of 17.7-18 hours and centered at 237.62°E and -23.26°N. Viewing geometries include solar incidence angles between 50°- 89° and emission angles between 1°- 28°. The daytime THEMIS image was collected in July 2012 with a local time of 16.39. Solar incidence is measured at 74.9° with an emission angle of 1.29°. THEMIS Sinusoidal Geometrically Registered Records (SNU) were atmospherically corrected using the same methods as described in chapter 4.2. Based on the availability of THEMIS ROTO (see Chapter 2.5.1), daytime image data, and available HiRISE image data, two regions of interest (ROI) were selected for analysis. Averaged TIR emission spectra from ~100-pixel ROIs were used to sample large areas of two flows, a visibly rough and smooth flow within ROI 1 and a paired channel and levee in ROI 2 (Figure 36). Large areas were chosen to minimize potential localized abnormalities in surface cover or dust mantling and differences in aerial coverage between each THEMIS image. TIR emission spectra extracted from each ROTO and daytime image were analyzed to determine the relative contributions of thermally mixed surfaces. Surface morphology at each ROI was compared using either HiRISE image data at 50 cm/pixel (ROI 1) or CTX image data at ~5 m/pixel (ROI 2) (McEwen et al., 2007; Malin et al., 2007). Visible images were acquired at solar incidence angles of 49° and 46°, respectively (Table 4).

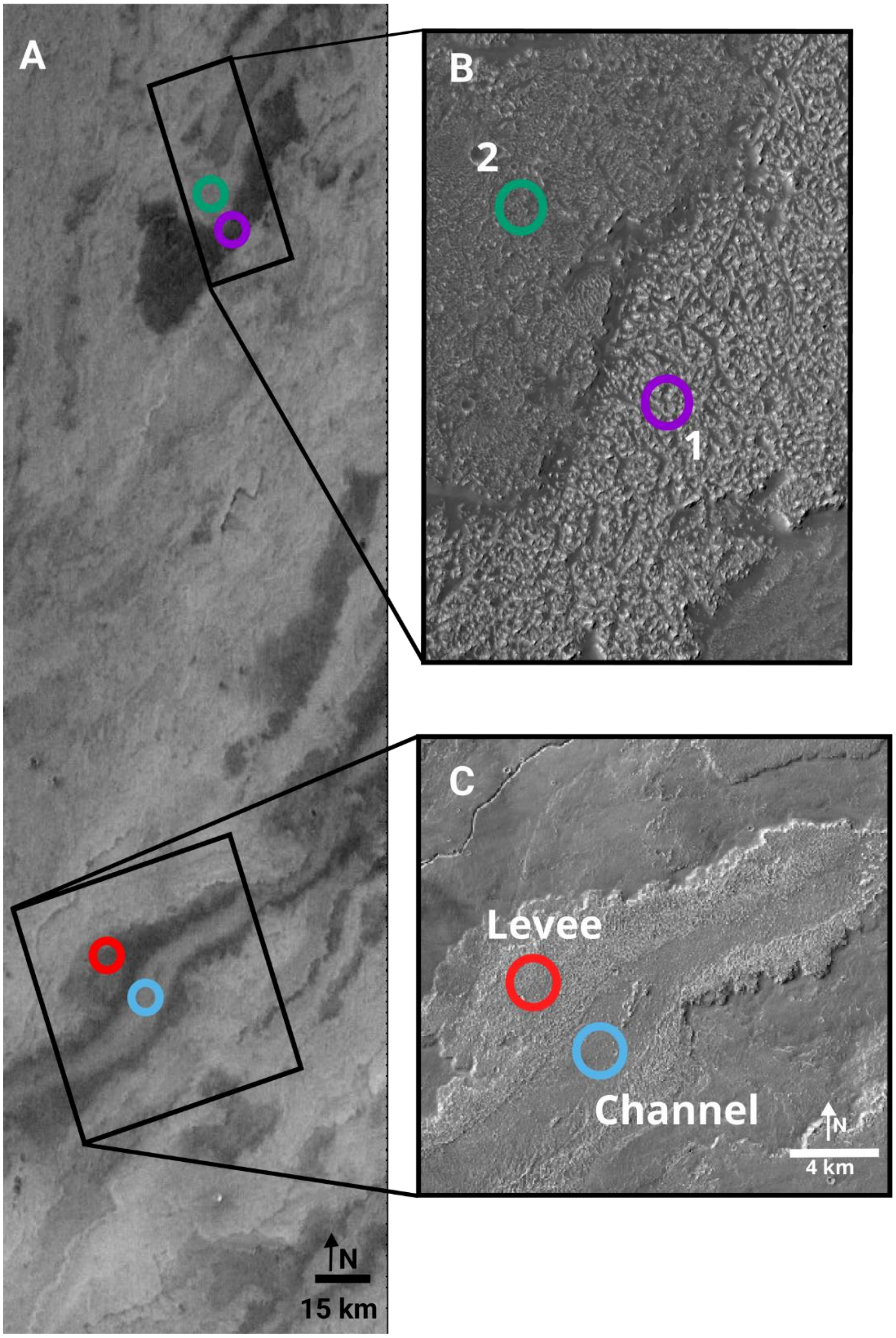

Figure 36. A) THEMIS TIR brightness temperature image collected during the ROTO campaign over Arsia Mons. B) HiRISE image showing the locations of Flows 1 and 2. C) CTX image showing the locations of Levee and Channel structures.

Table 8. Data-specific parameters of the THEMIS, CTX, and HiRISE image data used in this study.

Image ID	Roll Angle	Emission Angle	Solar Longitude (L_s)	Local Time	Incidence Angle
I68172002	-25°	-28.2°	355.85°	17.7	85.2°
I68222002	0°	1.4°	356.89°	18.0	89.0°
I47117003	0°	1.3°	146.38°	16.4	74.9°
P01_001524_1569_XN_23S122W 1	n/a	7.4°	17.68°	14.7	49.2°
J03_046028_1574_XN_22S123W	n/a	29.5°	156.3°	15.6	61.6°

5.3.1 Thermophysical Modeling and Prediction of Anisothermality

The presence of negatively sloped emission spectra and variations in TI values on a diurnal and seasonal time scale provides insight into surface heterogeneity (Jakosky, 1976; Putzig and Mellon, 2007; Bandfield and Edwards, 2008; Bandfield, 2009; Bandfield et al., 2015). However, understanding the scope of heterogeneity, including the potential range of materials and their configurations, becomes a complex problem. Here we employ ROTO observations paired with forward modeling of surface temperatures to produce a range of two-component scenarios containing lateral and vertical mixtures of different thermophysical materials. Using these modeled temperatures, we derive mixed component TIR emission spectra allowing for quantification of surface characteristics such as lateral dust/rock ratios, rock abundance, rock size, and estimated dust thickness.

The KRC thermal model (Kieffer, 2013; See Chapter 2.2.2.1 and Chapter 4.2) was used to predict surface temperatures over a range of thermal inertia values for each THEMIS observation. KRC model inputs of latitude, longitude, local time, solar longitude, visible dust opacity, and albedo at the observation time were used (Table 5). Here we adopted the techniques of Ahern et al. (2021) to account for dust column opacity. Briefly, dust column opacity values were extracted from the dust climatology database (Montabone et al., 2020) using the latitude, longitude, Ls, and Mars year for each observation. This database combines MGS TES, Mars Odyssey THEMIS, and MRO Climate Sounder (MCS) observations with global coverage from Mars years 24-32 (April 1999-July 2013). MCS data for Mars year 33 (May 2017-March 2019) are weighed more heavily than THEMIS data to account for Mars Odyssey's shift to a later overpass time (Montabone et al., 2020; Ahern et al., 2021).

5.3.2 Lateral Mixing Model

Two sets of models were run. The first utilized a two-component TI mixture without vertical layering (Figure 37A). KRC was used to independently predict temperatures for each component (i.e., dust, sand rock). The resulting temperatures were then converted to radiance utilizing the data processing software Davinci and convolved with the THEMIS spectral bands (Edwards et al., 2011, Edwards et al., 2015). Radiance spectra are given “spectral color” by multiplying the radiance values by TES averaged low and high albedo surface emission spectra, obtained from the ASU spectral library and down-sampled to THEMIS resolution. This method assumes that the measured surface emissivity is a combination of surface dust, rock, and sand. Radiance spectra are mathematically mixed in 10% increments of two endmember abundances (90/10, 80/20, 70/30, etc.) to produce new mixed temperature simulated radiance spectra. This method is effective as radiance curves of spatial mixtures mix in a linear fashion (Ramsey and Christensen, 1998; Nowicki and Christensen, 2007; Bandfield, 2009; Audouard et al., 2014). Finally, emissivity spectral slopes were simulated by dividing the mixed temperature radiance spectrum by the Planck radiance at the THEMIS band 3 (7.93 µm). This method of emissivity separation is identical to the one applied to THEMIS measured radiance, allowing for a direct comparison (Bandfield, 2009).

5.3.3 Vertical Mixing Model

The vertical layering model works the same way as the horizontal mixing model (Figure 37B). However, instead of calculating pure endmember temperatures, the KRC model is used to determine the surface temperature of a two-layer surface. Under these conditions, model inputs of upper layer TI, lower layer TI, and thickness of the top layer are used, along with the previous observation-specific inputs. Here, the thicknesses inputs for the top layer ranged from 0.3mm - 1mm. Upper TI values of dust (63 TIU) and sand (214 TIU) were used, and lower layer TI values of rock (1200 TIU) and sand (214 TIU) were used. Radiance spectra are laterally mixed using the resulting 2-layer temperatures, and emissivity spectral slopes are simulated in an identical fashion as described above in section 5.3.2.

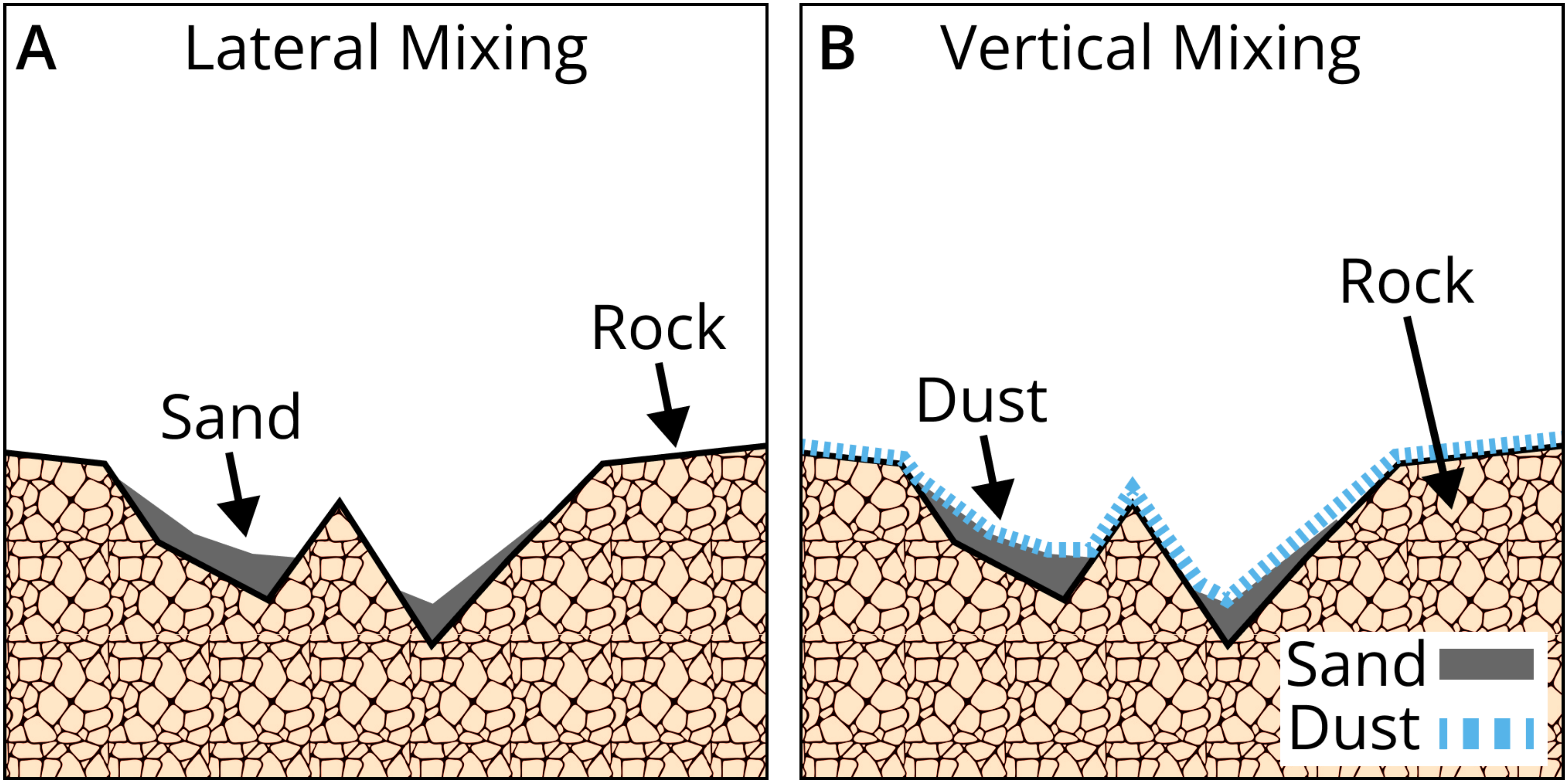

Figure 37. Schematic showing lateral (A) and vertical (B) mixing of rock, sand, and dust.

Table 9. KRC input parameters are used to calculate horizontal and vertical mixtures of thermally distinct surface units.

Name in KRC	Description	Value or Source
LAT/LON	Latitude	**Study area 1**: -21.735° N, 237.847° E, **Study area 2**: -22.605° N, 237.621° E
ELEV	Elevation	**Study area 1**: 4,203 m, **Study area 2**: 3,913 m
SLOPE	Slope angle	Assumed to be 0
ALBEDO	Albedo	2 ppd TES global albedo map (KRC default)
TAUD	Visible dust opacity (IR dust opacity*2.6)	Montabone et al., 2015, 2020
TAURAT	Ratio of TIR to VIS dust opacity ratio	0.2
DUSTA	Single scattering dust albedo	0.9
LS	Solar longitude (season)	See Table 7
HOUR	Local time	See Table 7
T	Surface temperature	Set by user/interpolated by model from given INERTIA
INERTIA	Layer 1 TI/apparent TI	63, 214 TIU
INERTIA2	Layer 2 TI	214, 1200 TIU
Thick	The thickness of layer 1	0.3mm - 1.0mm

5.3.4 THEMIS Spectral Processing and Analysis

THEMIS image data were processed in ASU's Davinci software using the standard radiance and atmospheric corrections described by Bandfield et al. (2004) and Edwards et al. (2011). This method uses a TES emissivity spectrum acquired from a spectrally bland ROI to separate and remove the atmospheric emission signature from the surface emission spectra. A thermophysical and compositionally homogeneous region is chosen as a "training region" based on visual inspection of CTX and THEMIS decorrelation stretch (DCS) image data. The previously acquired atmospheric signal is subtracted on a pixel-by-pixel basis. For a more in-depth discussion on atmospheric correction, the reader is referred to chapter 4.2 and Bandfield et al. (2004).

After atmospheric correction, emissivity/temperature separation is performed, and the retrieved emissivity spectra show different spectral slopes indicative of sub-pixel heterogeneous temperatures (Figure 39).

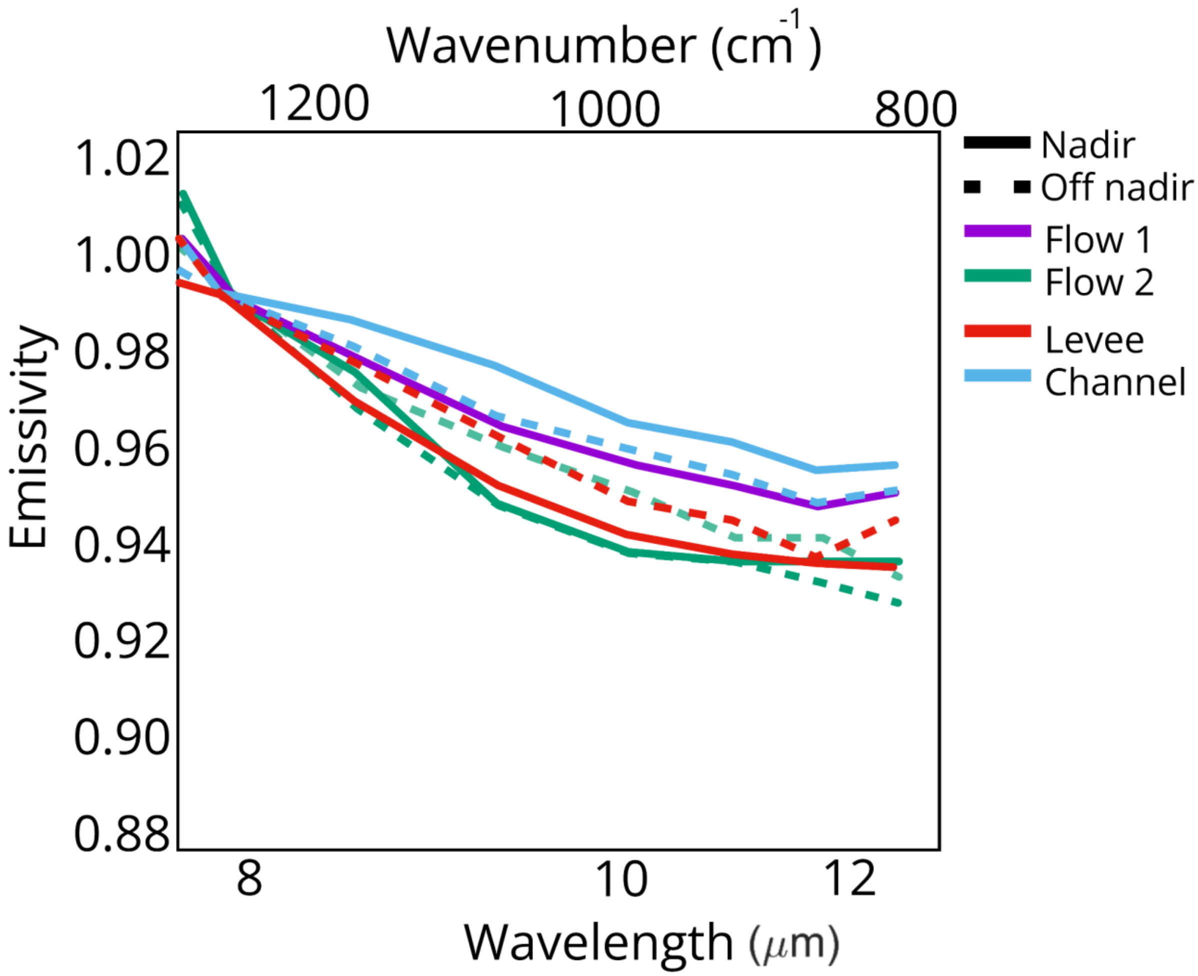

Figure 38. Spectral plot showing the presence of spectral slopes in the nadir and off-nadir data.

5.4 Results

5.4.1 Visibly Rough and Smooth flows

In study region 1, averaged emission spectra were extracted from the atmospherically corrected emissivity data and are shown in Figure 40. In the nadir TIR data, the two flow types appear similar in spectral shapes to Martian dust derived elsewhere on the surface (Bandfield, 2002). However, their spectral slopes are statistically different, with the bright, rugged flow (Flow 1) exhibiting a greater magnitude slope from ~7.5 to 11.5µm. The off-nadir TIR spectra collected at an emission angle of 25° show a similar story, although spectral slopes differ slightly. In comparison, the daytime TIR data exhibit nearly isothermal spectra with only a slight variation in slope between the two flows (Figure 40). Negative spectral slopes are commonly observed where surfaces contain multiple temperatures below the pixel resolution of the instrument, in this case, 100m (Bandfield et al., 2009, Crown and Ramsey, 2017; McKeeby et al., 2022).

In daytime TIR data, emission spectra from both flows in study region 1 are dust-like in composition and exhibit a slight negative spectral slope that is more pronounced in flow 1 (bright and rugged in visible image data). Flow 2 (darker and smooth in visible image data) exhibits little to no spectral slope. Differences in spectral shape are apparent where comparing the daytime and evening flows. Nadir spectral data collected during the ROTO reveal stronger absorption features at ~9.5µm, which matches basalt observed elsewhere on the surface (Bandfield, 2002; Crown and Ramsey, 2017). The ~9.5 µm absorption is less apparent in the off-nadir data and nearly absent for flow 2. In visible HiRISE image data, flow 1 appears rougher than flow 2 at the 1.5m scale (~50 cm/pixel) (Figure 41).

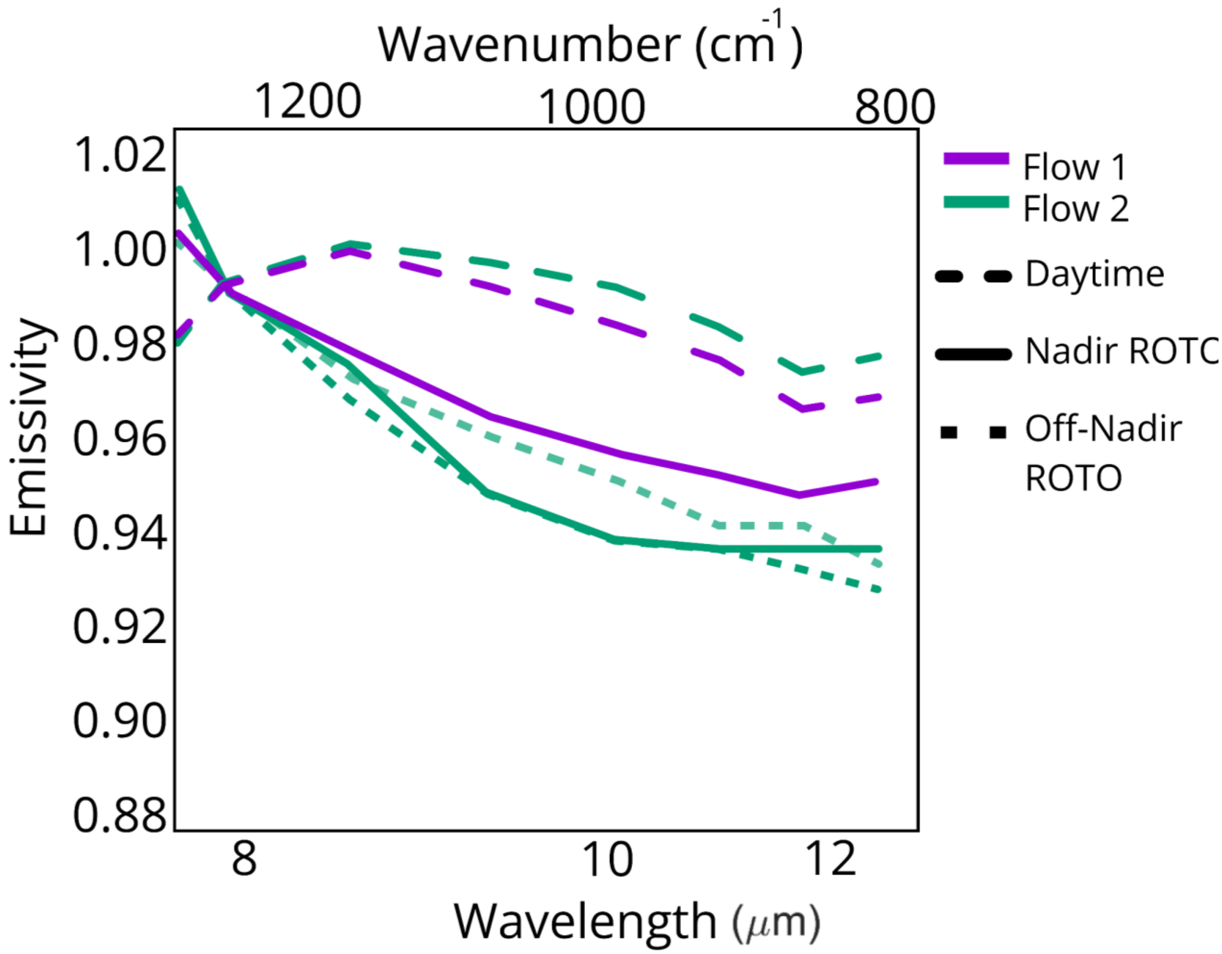

Figure 39. TIR emission spectra from study site 1 for flows 1 and 2. The dotted and solid spectral curves denote daytime and ROTO nadir/off-nadir data to the right.

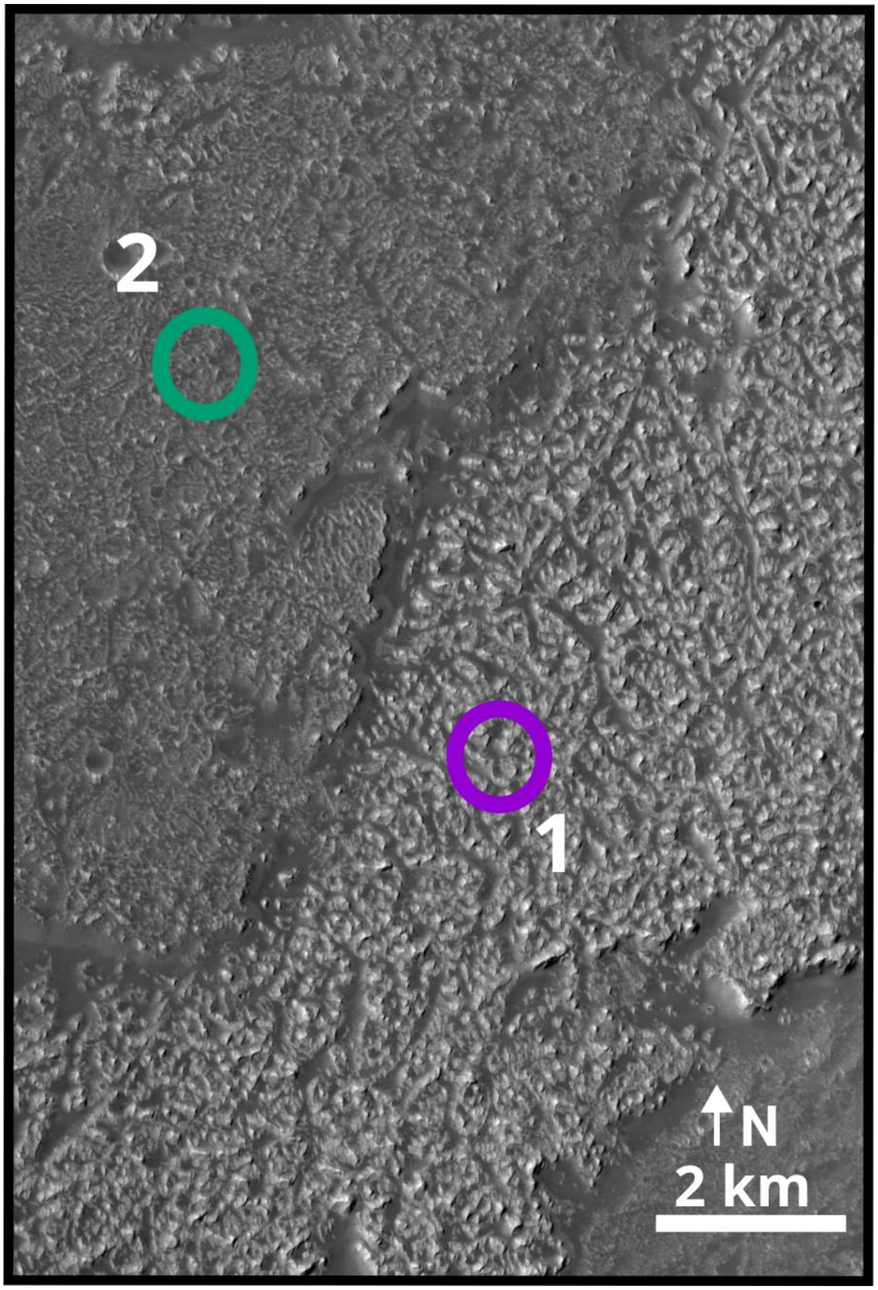

Figure 40. HiRISE image (J03_046028_1574_XN_22S123W) showing the locations of Flows 1 and 2 color-coded to their associated TIR emission spectra in figure 40.

5.4.2 Channelized Flow and Levee

Study region 2 is contained within a singular flow that displays visible levee and channel structures. A 100-pixel area was sampled from the channel and northern levee. Averaged atmospherically corrected emission spectra were extracted and are shown in Figure 42. Spectral slopes trends are similar to those observed in study region 1 and all four ROTO spectra display varying degrees of negative spectral slopes from ~7.5 to 11.5µm. In the nadir ROTO TIR data, spectral slopes strongly differ between the levee and the channel, with a greater negative slope observed from the levee spectrum. Off-nadir ROTO spectra show a similar response but a much lesser degree (Figure 42). Additionally, levee spectra exhibit a slightly stronger absorption feature at ~9.5 µm.

Daytime emission spectra lack major diagnostic absorption features and instead contain a slight negative slope from ~8.5 to ~12.5 µm, similar to Martian dust. Spectral slopes are similar in magnitude to daytime data from study region 1, with the levee spectra displaying a slightly greater spectral slope. In visible image data, a channelized flow is seen bounded by lateral levees. Along the flow length, the central channel appears to widen visibly, and small breakout lobes are observed extending from the main channel (Crown and Ramsey, 2017). The central channel appears smoother at CTX resolution (~5m/pixel) compared to the levee units. Levees appear to be a horizontal mixture of outcropping lava flows inundated by smoother material (Figure 43). Unfortunately, no HiRISE image data is available for this region.

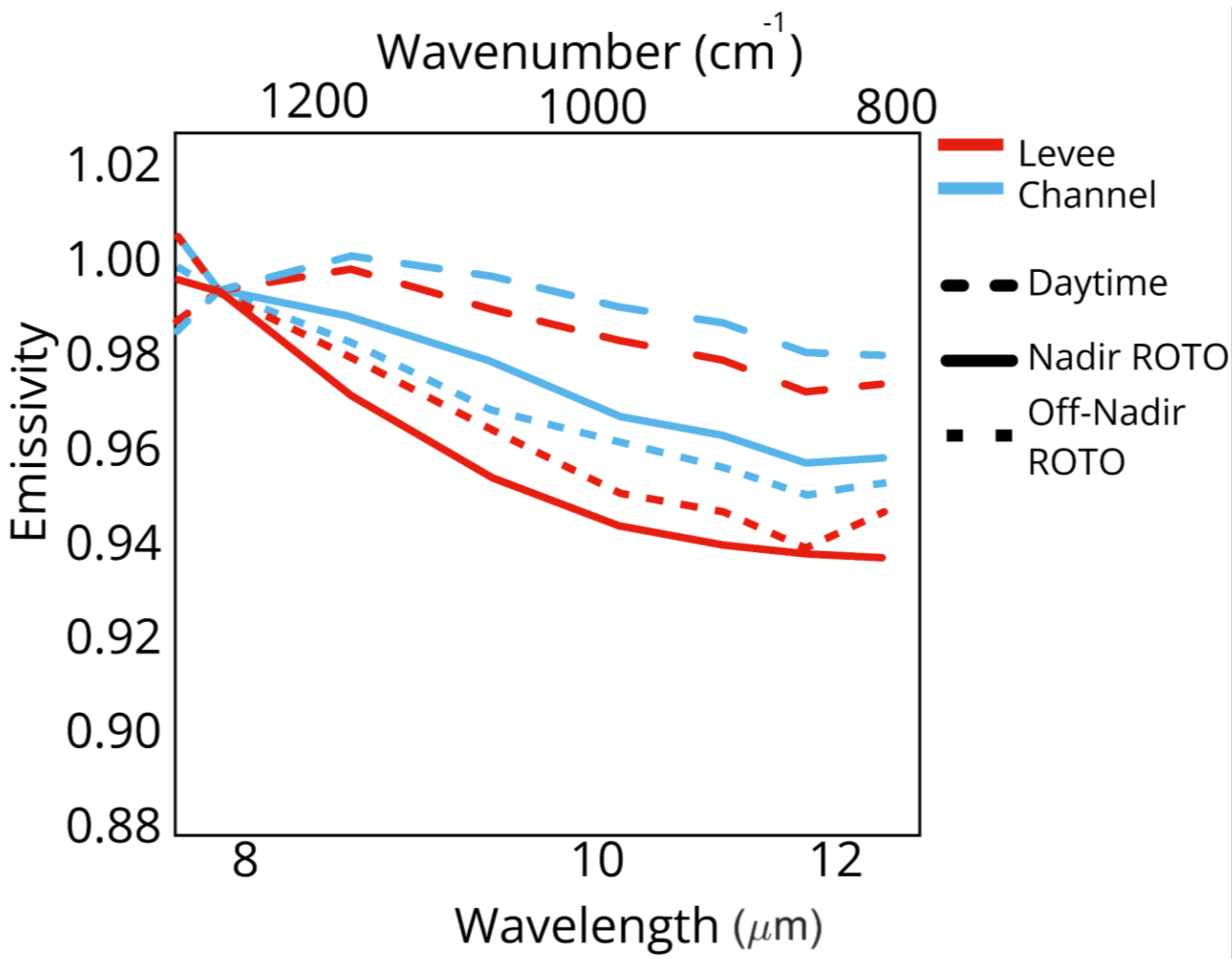

Figure 41. TIR emission spectra of the channel and levee flow portion in study site 2. The dotted and solid spectral curves denote daytime and ROTO nadir/off-nadir data to the right.

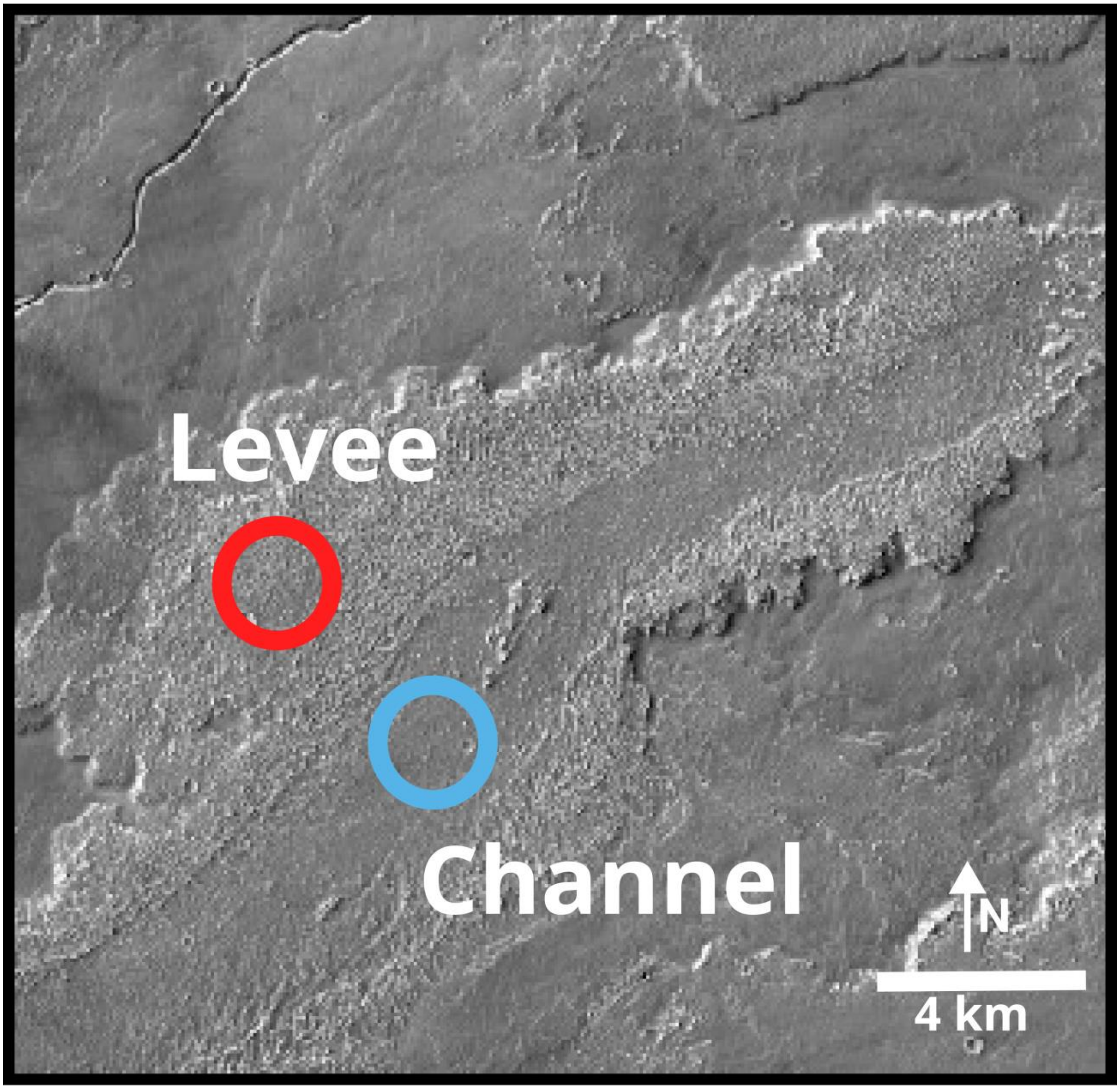

Figure 42. CTX image (P01_001524_1569_XN_23S122W 1) shows the locations of the levee and channel ROIs where TIR emission spectra were extracted.

5.4.3 Thermophysical Model Results

Initial surface heterogeneity was analyzed using single-layer horizontal mixtures of rock and sand, rock and dust, and dust and sand. Modeled spectral slopes and brightness temperature are calculated using the methods described in section 5.3.1. The modeled emission spectra were compared to measured THEMIS ROTO data at nadir and off-nadir viewing geometries. The modeled spectral slope and TI are compared to measured values to assess the model fit, and the root mean square (RMS) error and median absolute (MAD) error are calculated. Significance was defined where the RMS error was less than or equal to 0.003 or 3σ of the total RMS error. All model uncertainties represent their components' ± 5% relative contribution. As the spectral slope is a function of the difference in temperature across a THEMIS pixel, it independently does not provide a precise representation of surface conditions. For example, spectral slopes of a similar magnitude may arise from multiple combinations of distinct thermophysical units. Here we include the addition of brightness temperature to constrain the modeled mixture to temperatures realistic to the time of observation.

5.4.3.1 Horizontal Mixing

The simplest mixing scenario includes a lateral, one-layer mixture of two thermally distinct components. Mixtures of rock & sand, rock & dust, and dust & sand were mixed at different relative percentages to create simulated composite radiance spectra. At flow 1, a modeled rock to dust ratio of 50/50 produced the closest match to the observed spectral slope from the nadir data. This resulted in a model fit with an RMS error of 0.0028, a MAD error of 0.0015, and a modeled brightness temperature of 209K compared with the measured temperature of 189 K (Figure 43). This model contains rock to dust ratios of 60/40 and 40/60 produced spectra with RMS errors of 0.0021 and 0.0036, respectively, and modeled brightness temperatures of 212 K and 206 K, respectively. Mixtures containing rock and sand did not produce significant model fits (RMS error <0.003 or 3σ standard deviation). Mixtures containing rock to sand distributions of 40, 50, and 60 percent rock with their relative percent sand component produced RMS error values ranging from 0.013-0.014. These results are shown in Table 10.

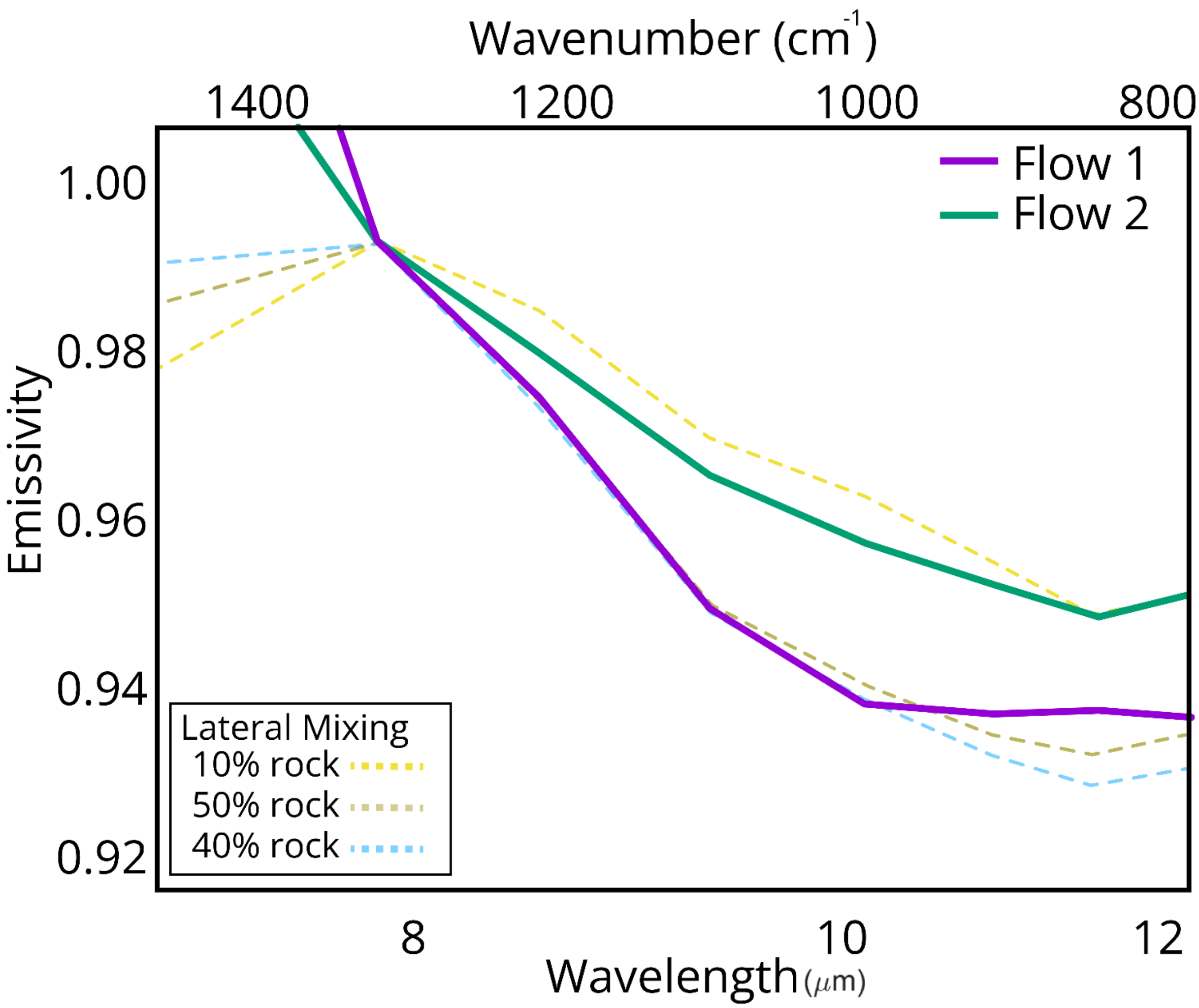

Figure 43. Results from the horizontal mixing model and measured TIR emission spectra from study site 1.

Table 10. Measured results for flow 1 compared to the horizontal mixing model results. The black box designates the best model fit.

Model Combination (± 5%)	*Brightness Temperature (± 2 K)*	*RMS error*	*MAD error*
Flow 1	189	N/A	N/A
40/60 Rock and Dust	206	0.0036	0.0025
50/50 Rock and Dust	209	0.0028	0.0015
60/40 Rock and Dust	212	0.0021	0.0018
40/60 Sand and Dust	200	0.0133	0.0125
50/50 Sand and Dust	202	0.0137	0.0133
60/40 Sand and Dust	204	0.0142	0.0138
40/60 Sand and Rock	219	0.0098	0.0092
50/50 Sand and Rock	215	0.0099	0.0092
60/40 Sand and Rock	213	0.0104	0.0091

Spectral modeling of the emissivity spectrum extracted from the flow 2 nadir data predicts a lower ratio of rock to dust. The modeled emission spectrum consisted of 10% rock and 90% dust which fit the measured data with an RMS error of 0.002 and a MAD error of 0.0018 (Figure 44, Table 11). A brightness temperature of 200K was calculated from the modeled radiance spectrum compared to a measured value of 203K at flow 2. These results are consistent with the smoother surfaces in HiRISE image data (Figure 41). In those HiRISE images, distinct ripple features are visible on both flow surfaces indicating that sand must be present in some abundance. Modeled mixtures containing combinations of sand and rock or sand and dust did not produce simulated spectral slopes matching the observed data (Table 11). The mixtures of sand and rock resulted in spectral fits with RMS error values above 0.003 and modeled brightness temperatures ~10 – 15 K warmer than measured values. Combinations of sand and dust produced modeled brightness temperatures close to the measured values. However, spectral slopes indicated a nearly isothermal surface, unlike the measured results. RMS error values ranged from 0.0071 – 0.0079 (Figure 45). These findings contrast the work by Simurda et al. (2017) and Simurda (2019), which identified combinations of rock and sand as present on these flows.

Table 11. Measured results for flow 2 compared to the horizontal mixing model results. The black box designates the best model fit.

Model Combination (± 5%)	*Brightness Temperature (± 2 K)*	*RMS error*	*MAD error*
Flow 2	203	N/A	N/A
10/90 Rock and Dust	206	0.0020	0.0018
20/80 Rock and Dust	204	0.0035	0.0030
30/70 Rock and Dust	202	0.0058	0.0052
60/40 Rock and Dust	212	0.0023	0.0019
40/60 Sand and Dust	200	0.0071	0.0070
50/50 Sand and Dust	202	0.0074	0.0071
60/40 Sand and Dust	204	0.0079	0.0024
30/70 Sand and Dust	202	0.0044	0.0040
40/60 Sand and Rock	219	0.0045	0.0042
50/50 Sand and Rock	215	0.0047	0.0045
60/40 Sand and Rock	213	0.0050	0.0047

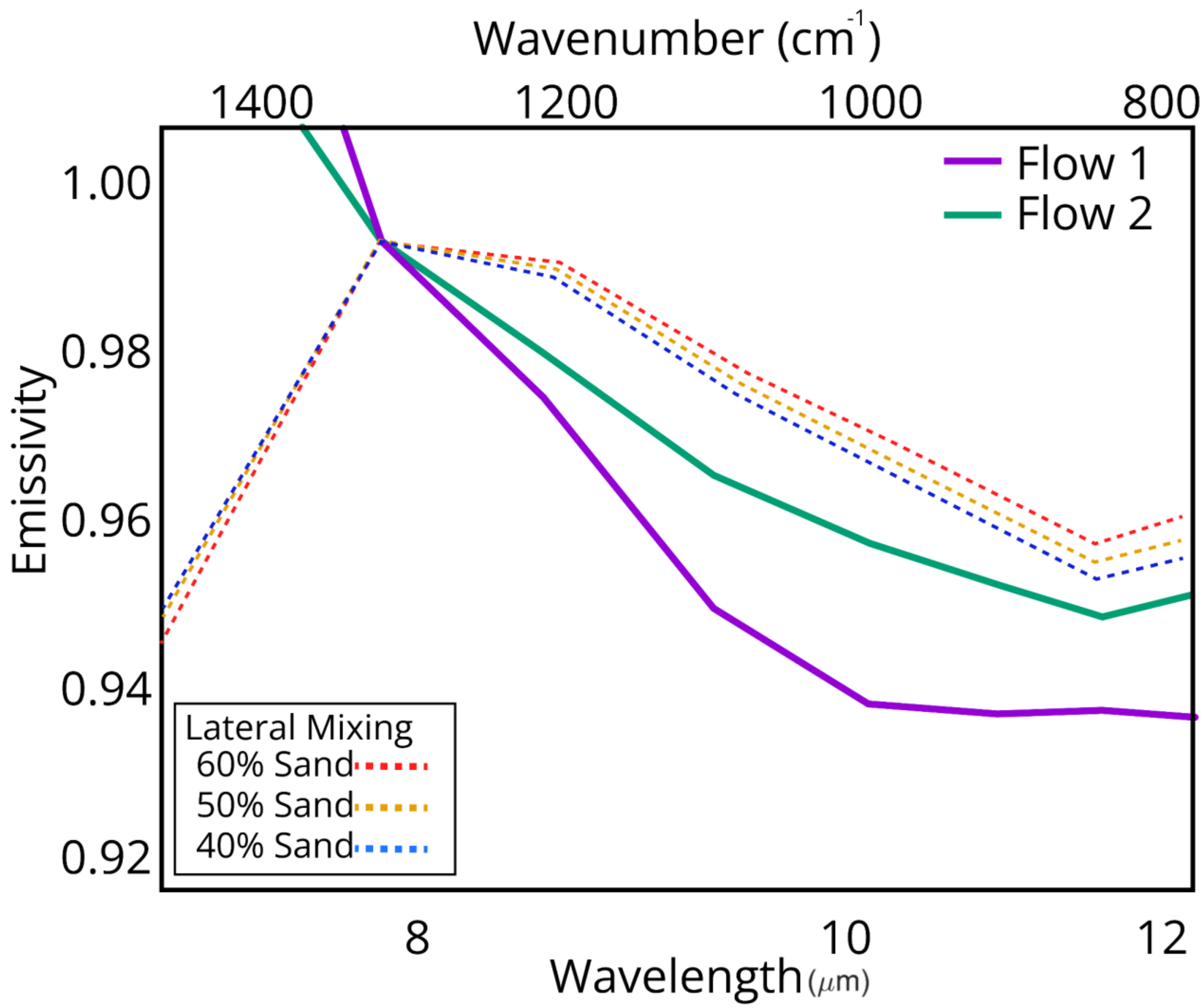

Figure 44. Emissivity spectra were produced from the horizontal mixing model (dotted lines) using mixtures of sand and rock. Solid lines indicate the measured TIR emission spectra at study site 1.

Thermophysical modeling of lateral mixing at study site 2 indicates a slightly higher rock to dust ratio in the levee region than was observed at the visibly rough flow in study site 1. The observed spectrum best matched the model containing a 60% rock and 40% dust ratio. This model ratio produces a simulated brightness temperature of 210K (Figure 45). The measured brightness temperature of this flow is 198K in band 9 (12.57 μm). The RMS error between the modeled and measured spectra was 0.002, and the MAD error was 0.002. However, two other model runs also fell within the RMS error's threshold for significance. The 50/50 distribution of rock and dust produced a modeled spectrum with an RMS error of 0.0021, and the 40/60 rock to dust model produced a modeled emissivity spectrum with an RMS error of 0.0022 between modeled and measured spectra (Table 12). The modeled brightness temperatures for these two model runs are 209 K and 206 K, respectively. This leaves some ambiguity in the modeled results. The lower modeled brightness temperature values may indicate a higher percentage of dust versus rock.

Table 12. Measured results for the levee portion of the flow compared to model results from the horizontal mixing model. The black box designates the best model fit, and the gray box signifies other model runs that fall within the significance parameters.

Model Combination (± 5%)	*Brightness Temperature (± 2 K)*	*RMS error*	*MAD error*
Levee	198	N/A	N/A
20/80 Rock and Dust	204	0.0035	0.0030
30/70 Rock and Dust	202	0.0058	0.0052
60/40 Rock and Dust	210	0.0020	0.0020
50/50 Rock and Dust	209	0.0021	0.0019
40/60 Rock and Dust	206	0.0022	0.0021
60/40 Sand and Dust	204	0.0117	0.0016
30/70 Sand and Rock	202	0.0044	0.0040
40/60 Sand and Rock	219	0.0071	0.0063
50/50 Sand and Rock	215	0.0073	0.0065
60/40 Sand and Rock	213	0.0077	0.0058

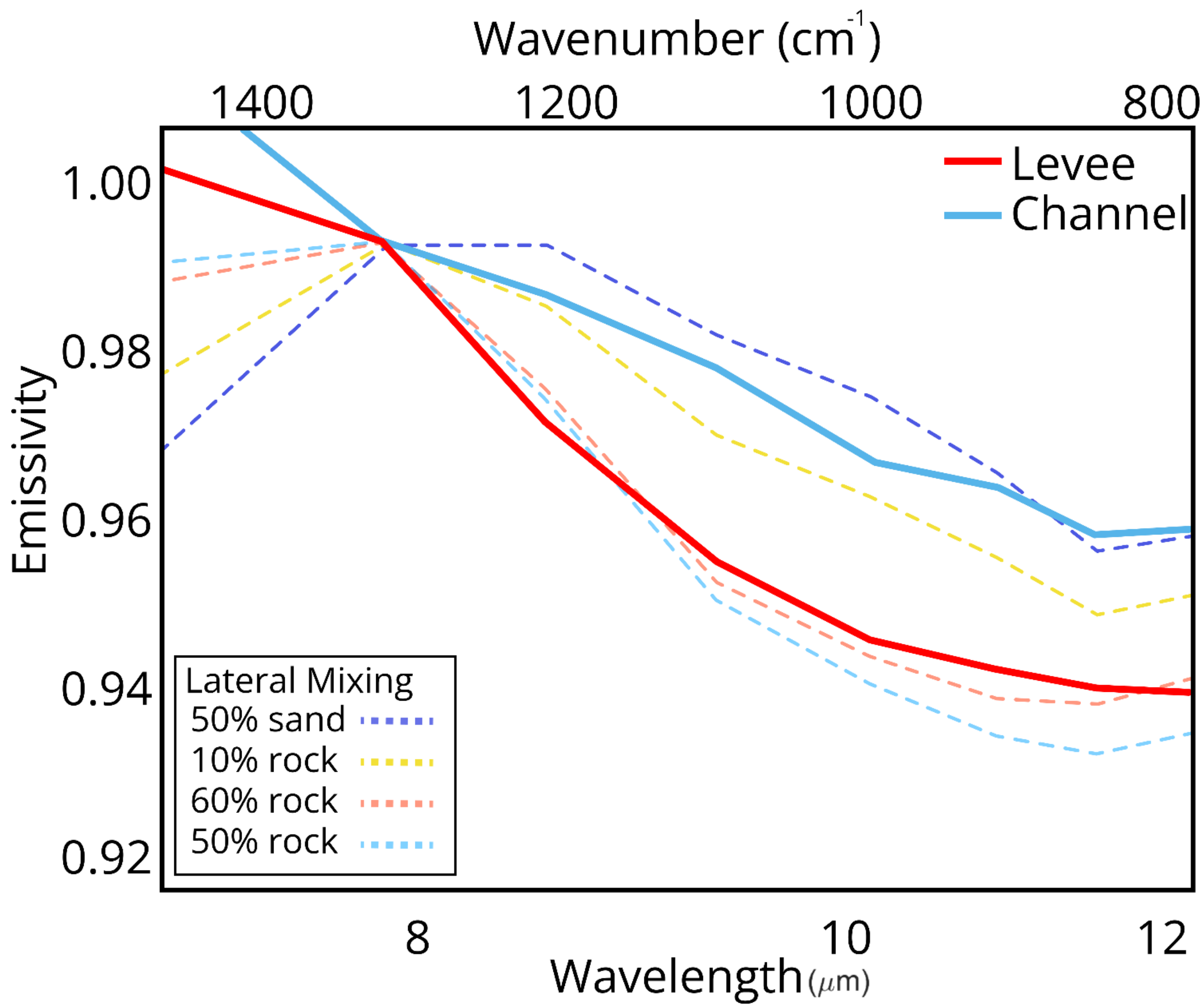

Figure 45. Emissivity spectra were produced from horizontal mixtures of rock and dust or rock and sand (dotted lines) and measured TIR emission spectra from study site 2 (Solid lines).

Emissivity modeling of spectra from the channelized region of the flow indicates a lateral mixture containing 50% sand and 50% dust. These results significantly fit measured emissivity spectra with an RMS error of 0.0018 and a MAD error of 0.0018 (Figure 45). A simulated brightness temperature of 200K is calculated, which closely matches the measured temperature of 204K. Simulated mixtures containing 30-60% rock and their correlating sand component also resulted in model runs falling within the significance window. However, modeled brightness temperatures were ~10-15 K warmer than THEMIS-derived brightness temperatures (Table 13).

CTX image data of this region shows rough levee material with numerous lava outcrops poking above a more uniform surface layer (Figure 46). Material within the central channel material looks smoother. Outcropping material is present; however, it appears muted, potentially indicating the presence of mantling by fine-particle size material.

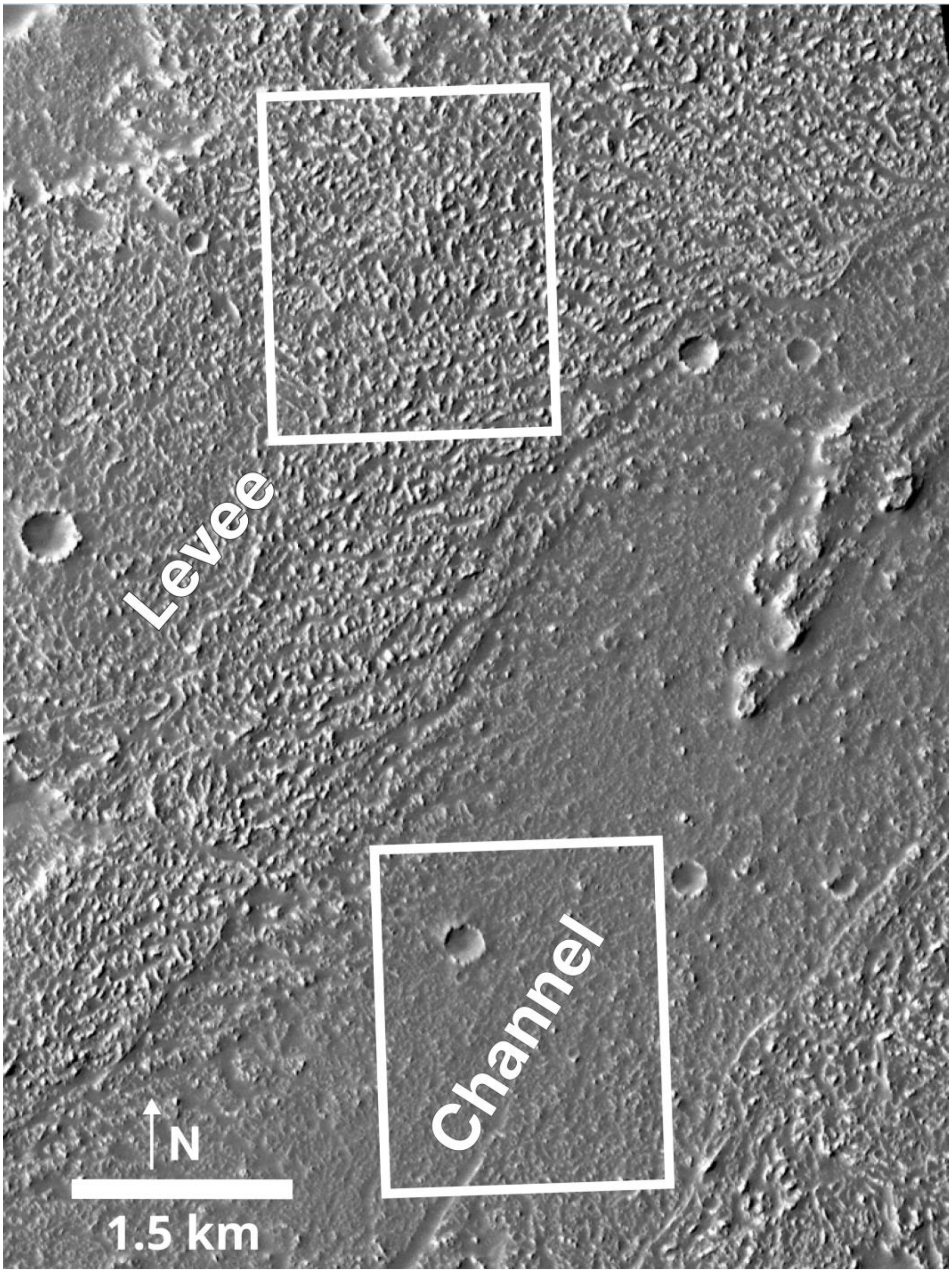

Figure 46. CTX image (F02_036731_1578_XN_22S122W) showing the visibly rough levee and smoother channel. Spectra were acquired and averaged from the regions illustrated in the white boxes.

Table 13. Measured results for the flow channel portion compared to model results from the horizontal mixing model. The black box designates the best model fit.

Model Combination (± 5%)	*Brightness Temperature (± 2K)*	*RMS error*	*MAD error*
Channel	204	N/A	N/A
10/90 Rock and Dust	206	0.0036	0.0028
20/80 Rock and Dust	204	0.0031	0.0030
30/70 Rock and Dust	202	0.0035	0.0033
60/40 Rock and Dust	212	0.0051	0.0048
40/60 Sand and Dust	200	0.0022	0.0021
50/50 Sand and Dust	202	0.0018	0.0018
60/40 Sand and Dust	204	0.0030	0.0025
30/70 Sand and Rock	220	0.0024	0.0020
40/60 Sand and Rock	219	0.0024	0.0018
50/50 Sand and Rock	215	0.0022	0.0020
60/40 Sand and Rock	213	0.0020	0.0018

5.4.3.2 Vertical Mixing

Numerous orbital and in-situ investigations demonstrate that dust layering and coatings are ubiquitous across the Martian surface (Christensen, 1986; Johnson and Christensen, 2002; Kinch et al., 2007; Guzewich et al., 2017; Courville et al., 2021). The analysis of lateral surface mixing reveals the presence of low TI material with variable amounts of outcropping higher TI materials. Thin vertical layering of dust has been shown to affect or mask the base layer (Simurda et al., 2019; Ahern et al., 2021) and may explain some of the differences in brightness temperature observed between the measured and modeled datasets.

At study site 1, flow 1 best matched a 40/60 lateral mixture of rock and dust, overlain by a thin vertical layering of dust 0.3-0.4 mm thick. Simulated emissivity spectra fit the measured spectra with an RMS error value of 0.0015 – 0.0022 and a MAD error of 0.0013-0.0018 (Figure 47, Table 14). The modeled brightness temperature of this mixture is 204K – 206K, producing a better fit than the lateral mixture (50/50 rock and dust), which had a derived brightness temperature of 209 K and an RMS error of 0.0028.

Flow 2 best matches a vertical layering model containing a 0.7-1mm dust mantle over a lateral mixture of 20% rock and 80% dust (Figure 47). These model fits produce an RMS error of 0.0012 – 0.0015 and a MAD error of 0.0011, respectively. Simulated brightness temperatures are 200-201 K, close to the THEMIS-derived brightness temperature of this flow at 203 K. Mixtures containing rock and sand overlain by dust did not produce results consistent with the measured data and fell outside of the RMS significance window. These mixtures resulted in isothermal spectra and brightness temperatures ± 15- 20 K from THEMIS-derived values (Table 15).

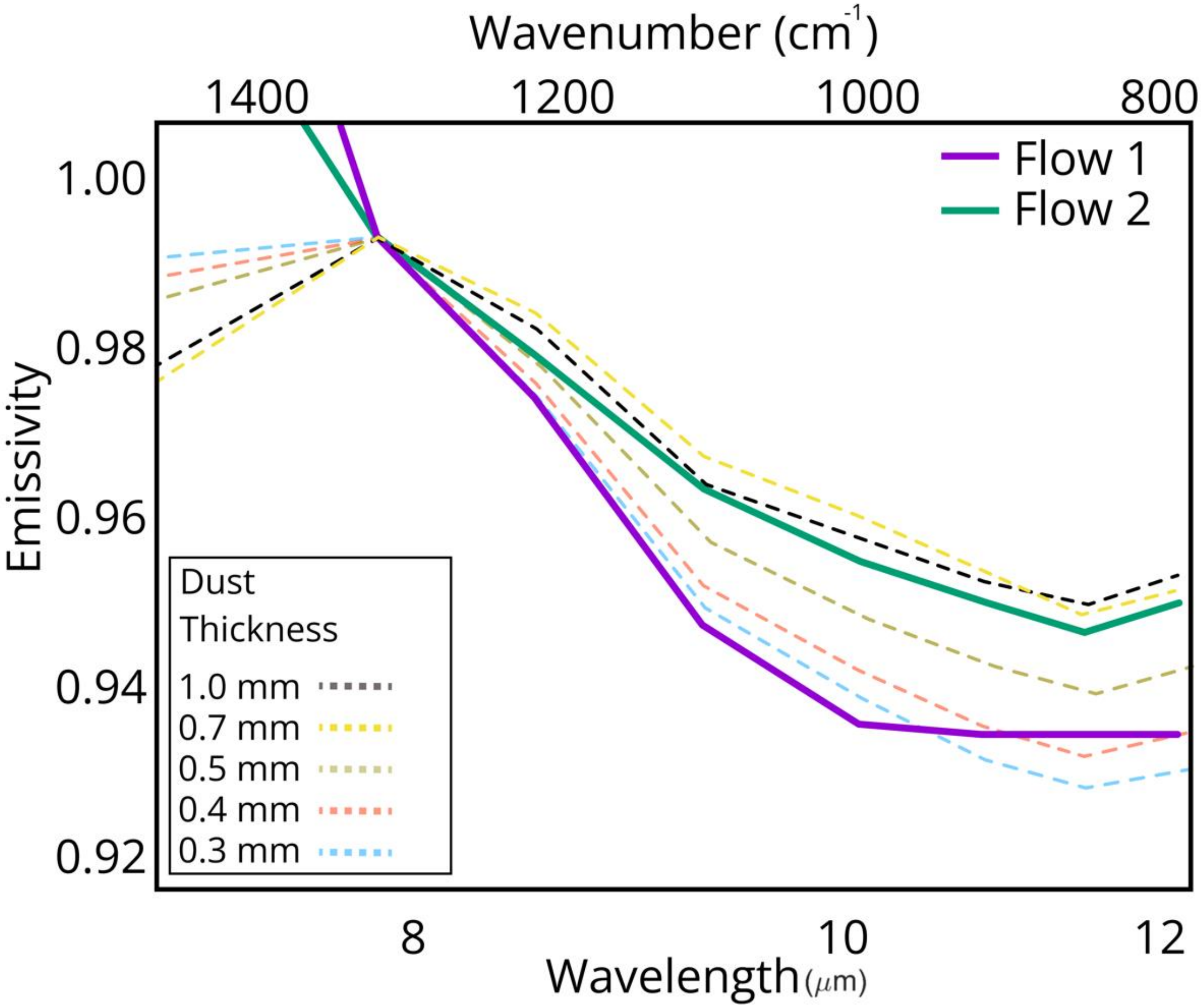

Figure 47. Emissivity spectra produced from the vertical layering model (dotted) compared with the measured TIR emission spectra (solid) from study site 1. Modeled spectra represent variable mixtures of rock and dust with a vertical layer of dust overlain on the horizontal mixture. A horizontal mixture of 60/40 dust and rock is used for these model runs.

Table 14. Measured results for flow 1 compared to model results from the horizontal mixing model overlain by a vertical layer of dust. The black box designates the best model fit.

Model Combination (± 5%)	*Brightness Temperature (± 2K)*	*RMS error*	*MAD error*
Flow 1	189	N/A	N/A
0.3 mm 40/60 Dust and Rock	206	0.0015	0.0013
0.4 mm 40/60 Dust and Rock	204	0.0022	0.0018
0.5 mm 40/60 Dust and Rock	202	0.0033	0.0030
0.7 mm 80/20 Dust and Rock	201	0.0035	0.0032
1.0 mm 80/20 Dust and Rock	200	0.0063	0.0058
1.0 mm 50/50 Dust and Rock	201	0.0065	0.0059
0.5 mm 70/30 Dust and sand	182	0.0118	0.0098
0.7 mm 80/20 Dust and sand	178	0.0066	0.0048

Table 15. Measured results for flow 2 compared to model results from the horizontal mixing model overlain by a vertical layer of dust. The black box designates the best model fit.

Model Combination (± 5%)	*Brightness Temperature (± 2K)*	*RMS error*	*MAD error*
Flow 2	203	N/A	N/A
0.3 mm 40/60 Dust and Rock	206	0.0065	0.0034
0.4 mm 40/60 Dust and Rock	204	0.0060	0.0032
0.5 mm 40/60 Dust and Rock	202	0.0048	0.0032
0.7 mm 80/20 Dust and Rock	201	0.0012	0.0011
1.0 mm 80/20 Dust and Rock	200	0.0015	0.0011
1.0 mm 50/50 Dust and Rock	201	0.0025	0.0020
0.5 mm 70/30 Dust and sand	182	0.0061	0.0048
0.7 mm 80/20 Dust and sand	178	0.0021	0.0018

At study site 2, the measured levee spectrum best matches that of a vertical layering model containing 60% dust and 40% rock, overlain with 0.4 mm of dust (Figure 48). This modeled mixture produces a simulated brightness temperature of 201K at band 9, compared to the measured brightness temperature of 198K at band 9. Linear least squares fitting indicated spectral fits with an RMS error of 0.0023-0.0024. The channel spectrum closely matched the vertical layering model containing 50% dust and 50% rock overlain by 0.7mm of dust. This model produced a spectral fit with an RMS error of 0.0025 and a MAD error of 0.0018 (Table 15). Simulated and THEMIS-derived brightness temperatures matched at 204K. Like site 1, mixtures containing ratios of dust and sand or dust and rock did not produce a significant model fit (Tables 14, 15).

Where dust cover exceeds 0.7mm, the vertical layering model predicts minimal change in spectral slope regardless of the lateral mixture. In other words, where mantled by >0.7mm of dust, the lateral mixture containing 20% rock and 80% dust had a similar modeled spectral slope to one containing 40% dust and 60% rock. However, higher percentages of rock increase the modeled brightness temperature. Additionally, spectral shape is impacted where the lateral mixing ratio is rock dominant. At higher percentages of rock, spectra gain a dominant “bowl-shape” with stronger absorptions between 9-10µm (Figure 49). This is attributed to the increased radiance from the rock component, which exhibits stronger Si-O stretching in the 9-10 µm wavelength region.

Table 16. Measured results for the levee portion of the flow compared to model results from the horizontal mixing model overlain by a vertical layer of dust. The black box designates the best model fit.

Model Combination (± 5%)	*Brightness Temperature (± 2K)*	*RMS error*	*MAD error*
Levee	203	N/A	N/A
0.3 mm 40/60 Dust and Rock	201	0.0024	0.0022
0.4 mm 40/60 Dust and Rock	203	0.0023	0.0020
0.5 mm 40/60 Dust and Rock	200	0.0030	0.0027
0.7 mm 80/20 Dust and Rock	198	0.0050	0.0043
1.0 mm 80/20 Dust and Rock	195	0.0033	0.0031
1.0 mm 50/50 Dust and Rock	200	0.0033	0.0030
0.5 mm 70/30 Dust and sand	180	0.0027	0.0022
0.7 mm 80/20 Dust and sand	176	0.0090	0.0065

Table 17. Measured results for a channelized portion of the flow compared to model results from the horizontal mixing model overlain by a vertical layer of dust. The black box designates the best model fit.

Model Combination (± 5%)	*Brightness Temperature (± 2K)*	*RMS error*	*MAD error*
Channel	204	N/A	N/A
0.3 mm 40/60 Dust and Rock	201	0.0040	0.0035
0.4 mm 40/60 Dust and Rock	203	0.0040	0.0031
0.5 mm 40/60 Dust and Rock	200	0.0030	0.0027
0.7 mm 50/50 Dust and Rock	204	0.0025	0.0018
1.0 mm 60/40 Dust and Rock	201	0.0032	0.0027
1.0 mm 50/50 Dust and Rock	200	0.0051	0.0043
0.5 mm 70/30 Dust and sand	180	0.0041	0.0035
0.7 mm 60/40 Dust and sand	176	0.0090	0.0065

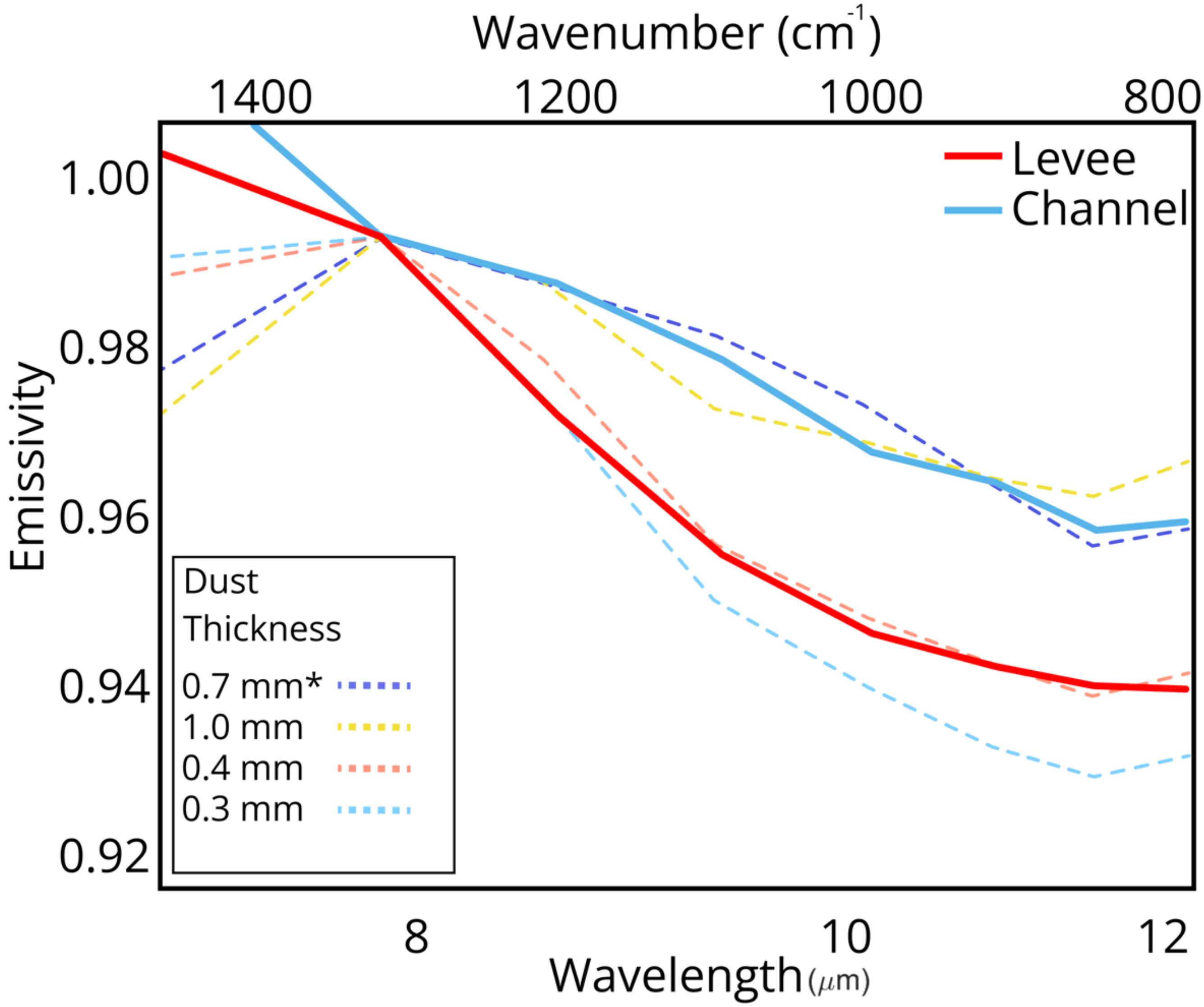

Figure 48. Emissivity spectra produced from the vertical layering model (dotted) compared with the measured TIR emission spectra (solid) from the levee and channelized protion of the lava flow in study site 2. Modeled spectra represent variable mixtures of rock and dust with a vertical layer of dust overlain on the horizontal mixture. The horizontal mixture contains a 60/40 dust-to-rock ratio, except for the 0.7mm model, which utilized a 50/50 mixture of rock and dust, denoted by the (*).

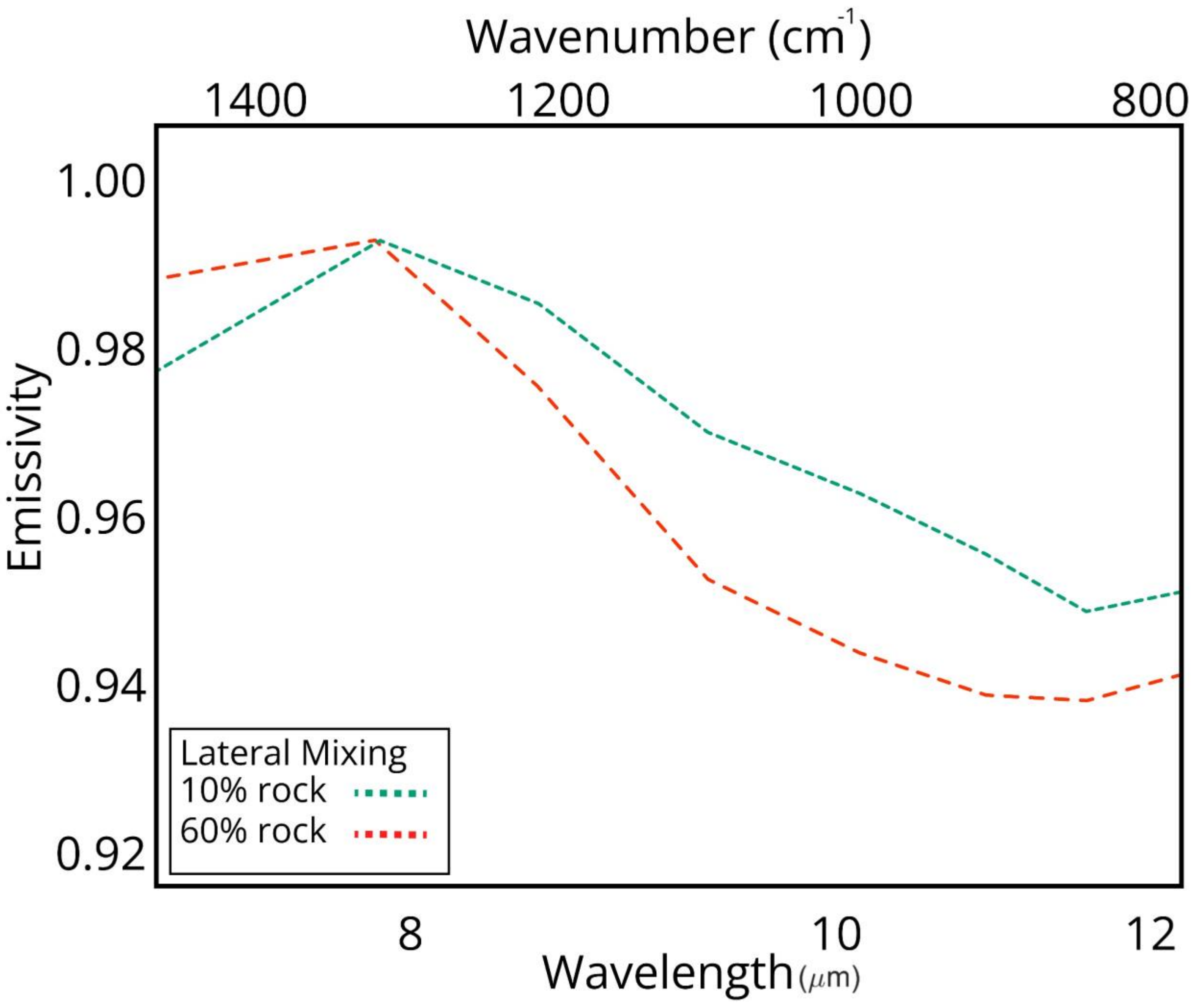

Figure 49. Modeled TIR emission spectra demonstrating the deepening of spectral features in the 8.5-12 μm region with increasing rock abundance. Spectra represent variable mixtures of rock and dust.

5.5 Discussion

Spectral slopes in THEMIS data can be fitted with a single lateral or vertical mixing model, although cases arise where multiple model combinations provide a possible solution. This ambiguity is likely due to surface complexities not fully represented by model conditions. It may result from daily variability or model inputs not representative of actual surface conditions (i.e., incorrect estimates of dust opacity, weather, etc.). For an in-depth discussion on measurement and model sensitivity, see Chapter 4, Section 4.2.

5.5.1 TIR Spectral Slopes

Overall, the nadir viewing geometry produced more negative spectral slopes than the off-nadir geometry, indicating greater subpixel temperature mixing at this viewing angle and local time. This may be a function of spacecraft orientation or solar azimuth. The nadir viewing geometry preferentially sees a greater percentage of rough surfaces at varying angles and azimuth, thus appearing more anisothermal. Off-nadir viewing geometries exhibit warmer brightness temperatures as expected from the slightly earlier overpass time at 17.7 hours versus the nadir overpass at 17.9 hours or from preferentially viewing surfaces facing the sun. Lastly, daytime TIR spectra exhibit only a slight spectral slope at longer wavelengths indicating an isothermal surface, with the minor spectral slope resulting from the composition. Nadir ROTO TIR data from flows 1 and the levee appear more bowl-shaped with absorptions between 8.5-10μm. These spectra appear similar in shape to low albedo surfaces elsewhere on mars that have been linked to basaltic compositions (Bandfield, 2006; McSween et al., 2008; Ferrand et al., 2011; Rogers and Nekvasil, 2015; Crown and Ramsey, 2017).

Interestingly, the 8.5-10μm absorption feature is not present in the off-nadir and daytime data of the same surface. We propose that the absence of these features in off-nadir data results from their lower areal percentage at off-nadir viewing geometry. One possible explanation for this is that off-nadir ROTO data acquired at an emission angle of 28° preferentially observe less rocky material, potentially due to dust mantling or inundation of the lava outcrops by finer particles. Additionally, due to the later overpass time of the nadir ROTO, the warmer rocky materials emit a more significant radiance than smaller sand and dust particles. The greater radiance from rocky materials results in the spectral signature of the lava outcrop dominating the spectrum.

5.5.2 Horizontal and Vertical Mixing

Where solely relying on horizontal mixing, the observed anisothermality can be explained by varied lateral mixtures of rock and dust or rock or dust and sand. The horizontal model indicates that visibly rough flows contain 40-60% rock (Flow 1 and levee) and visible smooth flows constituting 10% rock at Flow 2 and 50% dust and sand in the channel. Alternatively, the vertical layering model provides a different scenario where rough surfaces contain dust and rock in a 60/40 ratio with a thin layering of dust ~0.4-0.5mm thick (Figure 47). In this scenario, the visibly smoother flows exhibit a thicker mantling of dust 0.7-1mm thick and the same 60/40 dust-to-rock ratio. The central channel in study site 2 is an exception, requiring a model containing a lateral mixture of 50% dust and 50% rock overlain by a vertical layer of 0.7mm of dust. In reality, the surface is likely more complex than can be adequately captured in a two-endmember mixing model. Visible image data supports the model predictions, as does independent analysis from Simurda (2019), where a similar lateral mixture was derived but predicted a thinner vertical dust layer of 0.2 mm.

The layering of surface dust affects the thermal signatures of lava flow surfaces significantly more than surfaces composed of sand size particles, as is apparent by the shape of the diurnal curve (Simurda, 2019, Ahern, 2021). The diurnal curve of dust exhibits a significant temperature change throughout the day. Additionally, the diurnal peak is earlier due to the speed at which fine particles gain and lose heat. Rocky material represents the opposite endmember with the least temperature change and the latest peak temperature hour. Sand-sized particles behave more closely to dust than rock and only exhibit a slight change in temperature and shift in peak temperature where mantled by dust. At the time of ROTO acquisition, the depth of the dust thickness has the most significant impact on the sand's temperature compared with any other time throughout the day and can result in up to a 20 K decrease in temperature between bare sand and sand mantled by up 1mm of dust (Figure 50).

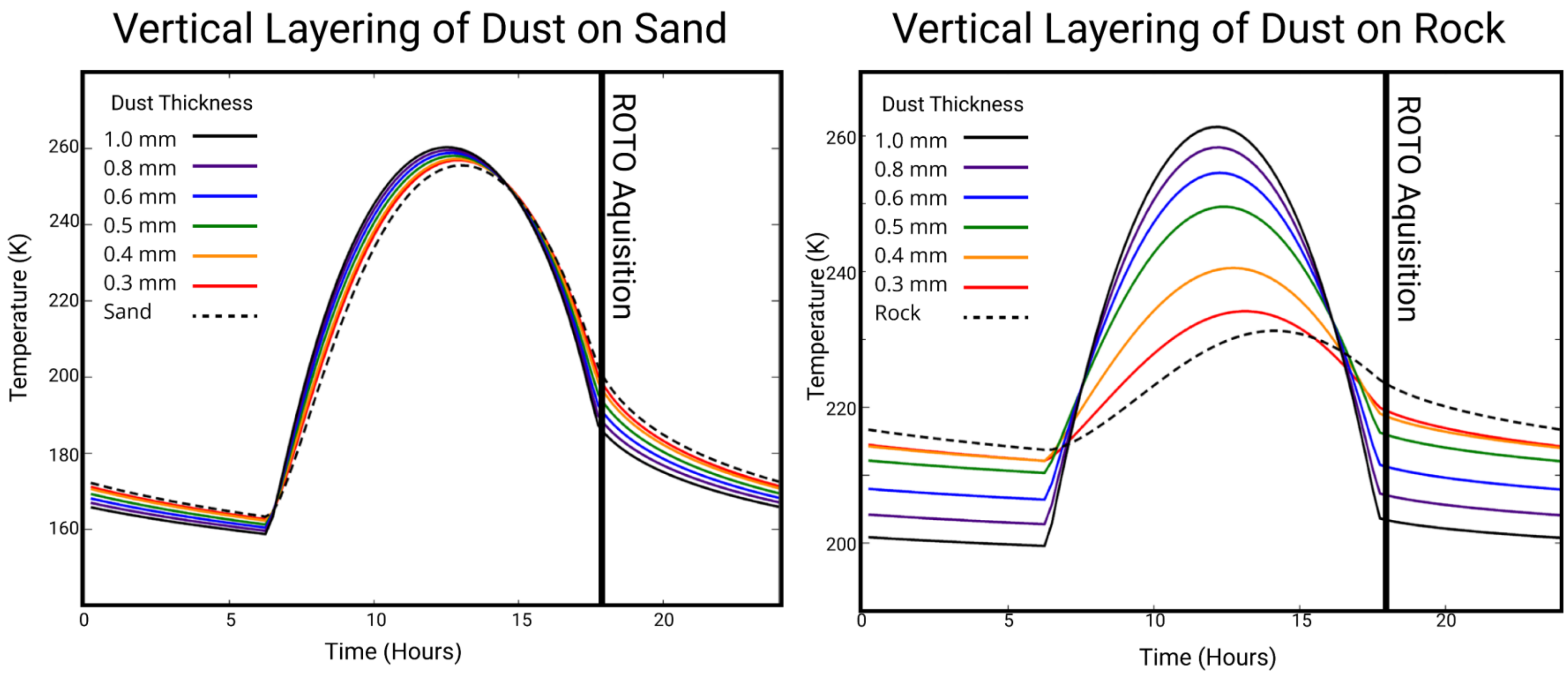

Figure 50. Diurnal curves show the temperature response to dust mantling on sand and rock and the modeled temperatures at the time or spectral acquisition by the ROTO.

5.5.3 Surface Roughness Effects

Although the horizontal and vertical mixing models produced spectral slope matches to the observed data, modeled brightness temperature did not consistently match the measured values. This discrepancy was more pronounced at flow 1 and the levee ROI, which appear visibly rough in HiRISE and CTX data. Furthermore, the off-nadir spectra for study sites 1 and 2 exhibit remarkably similar spectral slopes between flow types and higher brightness temperatures than their nadir counterparts. One explanation for this may be surface roughness effects resulting in variable shadowing conditions between viewing geometries.

This ROTO dataset was collected under near-dusk conditions with off-nadir observations acquired at an L_s of 355.85162° and an overpass time of 17.7 hours, followed by the nadir observation at an L_s of 357.92944° and an overpass time of 17.9 hours. In study area 1, flow 1 shows a decrease in brightness temperature with time, as expected. However, flow 2 exhibits a slight increase in brightness temperature between the off-nadir observation and nadir. Spectral slopes behave similarly. At the off-nadir viewing geometry, flow 1 exhibits little to no change in spectral slope compared to nadir, whereas flow 2 exhibits a slight increase (Figure 40). At the 28° emission angle with the sun illuminating the surface from the west, THEMIS detects the shadowed sides of rock preferentially. This suggests that smoother surfaces with fewer shadows exhibit higher brightness temperatures than more heavily shadowed, rougher surfaces.

Temperature and emissivity data collected at different emission angles can be affected by either surface roughness or thermophysical mixing (Bandfield and Edwards, 2008; Bandfield, 2009; Bandfield et al., 2015; McKeeby et al., 2022). We hypothesize that combining high solar incidence angles with the macroscale topography of rough lava flow produces non-random shadows that can remain in place for an extended time. This may complicate interpretations based on spectral or temperature data (Figure 51). The application of KRC presented here provides insight and constraints pertinent to the mixing of thermophysical distinct surface units. However, further work is needed to fully understand surface roughness's effects. To test this hypothesis and eliminate shadows, additional ROTOs acquired shortly after sunset. However, care must be taken to ensure that surface temperatures have not cooled below atmospheric temperatures. If shadows are eliminated, then any differences in brightness temperature or spectral slopes reflect the presence of distinct thermophysical units and not surface roughness effects. Likewise, a sequence of ROTOs collected earlier in the day with the sun at lower incidence angles could be used to derive surface roughness characteristics based on shadowing, assuming the distribution of shadows is random and follows a Gaussian distribution.

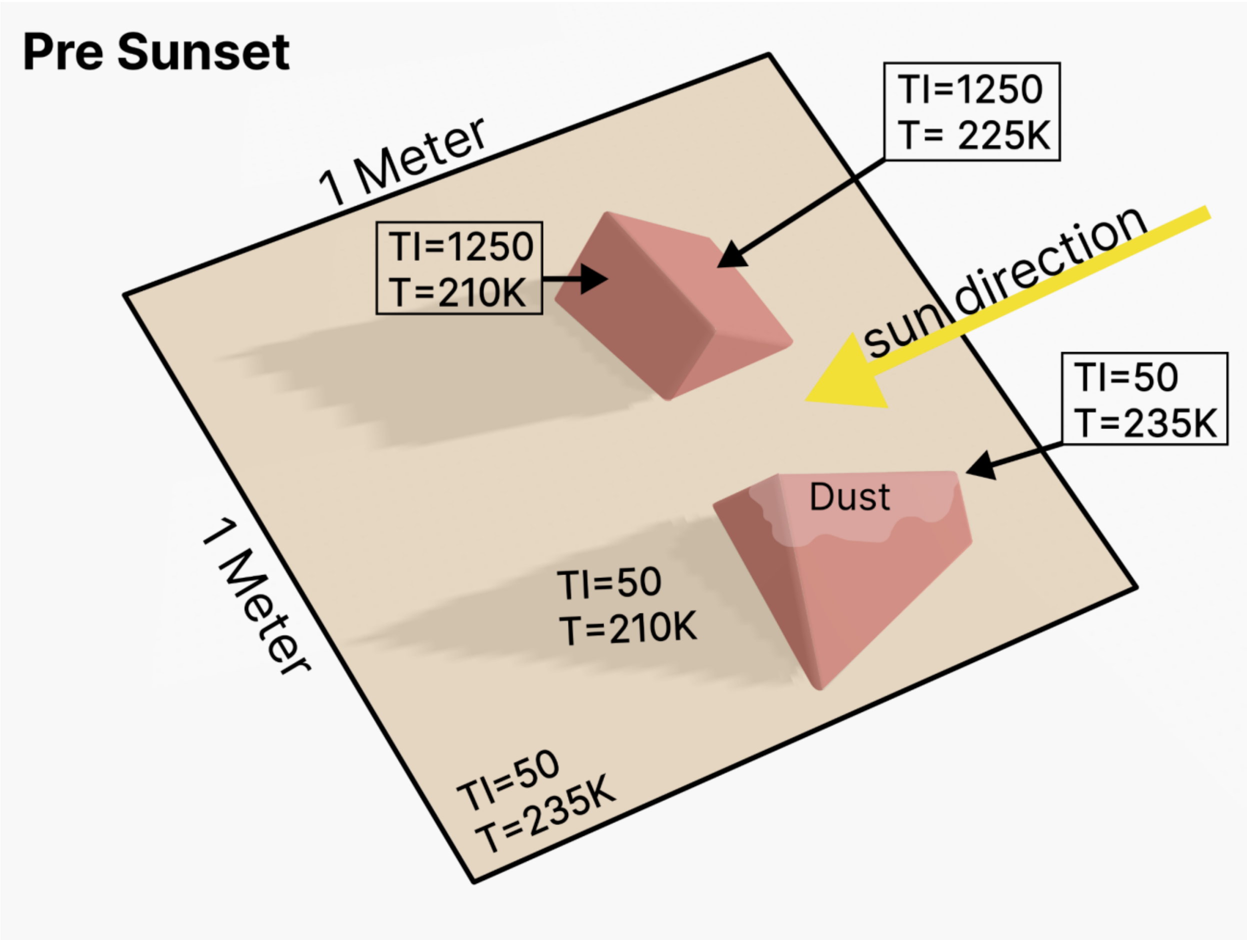

Figure 51. Schematic demonstrating the complexity where surface shadows are combined with surfaces containing sub-meter mixing of units and different thermal inertias values. At high solar incidence angles, objects approaching the meter scale no longer cast random shadows onto the surface.

5.6 Conclusions

The work presented here utilizes TIR spectral slope analysis and quantitative thermophysical modeling to investigate the presence of sub-pixel temperature mixing in relation to rough lava flows in Daedalia Planum. This region represents recent (~100 My) volcanic activity on Mars which may hold the key to understanding the evolution of late-stage volcanism in the Tharsis region (Crown and Ramsey, 2017). The methods described here supplement those of Crown and Ramsey (2017) and Simurda et al. (2019) and support their findings that the Daedalia Planum lava flows contain a checkerboard-like mixture of rock and sand with variable dust mantling. Lastly, this chapter builds upon the work by McKeeby et al. (2022; presented here in Chapter 4), demonstrating the use of TIR spectral slopes to derive vertically layered thermophysical differences and surface characteristics. It estimates dust cover thickness over late Amazonian age lava flows (~100 My, Crown and Ramsey, 2017). As well as, demonstrates that mixing models accounting for the vertical layering of fine materials produce a statistically better model fit than models relying solely on horizontal mixing.

By combining rigorous spectral analysis and thermophysical modeling, I develop a novel approach to quantifying lateral and vertical mixing of distinct thermophysical units using emission spectral slopes. In study region 1, results indicate that both flows contain a lateral mixture of high and low TI surface materials (rock and dust) in a 40/60 ratio. However, the visibly smooth flow exhibits a thicker overlying dust mantle of 0.7-1 mm (± 0.05 mm) versus the rougher surface that is mantled by a 0.4 ± 0.05 mm thick layer. This suggests a change in the aeolian depositional processes as a function of the flow's surface roughness. Visibly smoother lava surfaces contain thicker vertical layers of dust than nearby visibly rougher surfaces. This implies a difference in either deposition or erosional rates over a relatively small area of several kilometers.

Additionally, this work demonstrates the utility of ROTO in investigating complex surfaces. Previously, Daedalia Planum has been considered too dust-covered for any compositional analysis. The presence of basaltic spectral signatures of the rough lava flows shown here contradicts this. These regions can now be targeted for more rigorous spectral analysis to constrain compositional differences between individual flows.

Future ROTOs designed to differentiate the effects of thermophysical mixing and surface roughness should be considered as, ultimately, they may impact the resulting emission spectra similarly. Overpasses performed just after sunset can minimize the spectrum effects of sunlit and shadowed surfaces. However, surface and atmospheric temperature must be considered to avoid competing atmospheric emission effects like those documented in chapter 4. Through careful planning and consideration for season and time of day, ROTO observations may allow for an expansion of Mars TIR spectroscopy into other regions once considered too challenging or difficult to image.

6.0 Concluding Remarks

Interpreting the processes that have affected a planetary surface typically requires detailed multi-instrument analysis in both the visible and TIR wavelength ranges over various spatial scales. The work presented here focuses on combining hyperspectral and multispectral thermal infrared spectroscopy to investigate the effects of sub-pixel thermophysical differences and determine surface topology. Laboratory-based analysis of pahoehoe and a'ā, collected from field campaigns in Mauna Ulu, Hawaii, document a reduction in spectral contrast correlated with increasing micron-scale surface roughness. Increases in micron-scale roughness result in multiple surface reflections that reduce spectral contrast due to a decrease in absorption band intensity (Ramsey and Fink, 1999; Carter et al., 2009, Berger et al., 2020). A reduction in skewness indicated by the surface topographic analysis supports the conclusion of more pits or vesicles where rough surfaces are viewed off-nadir. The three-dimensional surface reconstruction shows an increase of ~5% in variations of micron-scale topography where viewing samples off-nadir. A decrease in spectral contrast, like that observed in the hyperspectral data, is also seen at THEMIS resolution. Additionally, a disproportionate change in the depth of spectral features at long and short wavelengths is observed for smooth and rough surfaces where viewed from nadir and off-nadir. The change in depth of spectral features may indicate an increase in silica alteration products visible in the off-nadir viewing geometry.

Directional heating of pahoehoe and a'a samples resulted in emissivity slopes that trend negatively towards longer wavelengths off-nadir viewing geometries. Spectral slopes arise from the incorrect assumption of a uniform surface temperature across a pixel. Where surface temperatures vary at the sub-pixel scale, the surface no longer behaves in a Planck-like manner with respect to wavelength and temperature. In the absence of a homogenous pixel temperature, the Planck radiance function can only match the measured radiance at a single wavelength, resulting in an emission spectrum with negatively trending slopes towards longer wavelengths (Bandfield, 2009; Rose et al., 2014; Bandfield et al., 2015). Spectral slopes may complicate subsequent compositional analysis resulting in the over or under estimation of components during spectral mixture analysis (Ramsey and Christensen, 1998; Pan et al., 2015). In the laboratory study presented here, pronounced spectral slopes are visible at off-nadir viewing geometries, with the pahoehoe sample exhibiting a more significant negative spectral slope than the a'ā sample. Spectral slopes become more apparent where hyperspectral data is down-sampled to the THEMIS resolution multispectral data.

The effects of sub-pixel temperature mixing are further explored in chapters 4 and 5 using ROTO of the Mars Odyssey spacecraft. ROTO data provide a novel approach to examining sub-pixel thermophysical properties of the surface. Acquired are under similar diurnal and seasonal conditions, ROTOs differences in surface characteristics at variable emission angles and viewing geometry. Here, changes in brightness temperature and emission spectra are examined to determine the presence of thermophysical variation related to the distribution of dust, sand, and rock in Apollinaris and Arsia Mons. At Apollinaris mons, ROTOs collected over a full suite of emission angles from -31 to +33 revealed differences in rock abundance six times greater than published results relying on nadir data only.

Additionally, high-resolution visible images captured using the HiRISE instrument indicate a mixture of surface units from boulders to dunes, providing credence to the model. This allows us to better understand these two study sites' depositional and erosional processes. For instance, although sand ripples are present in HiRISE image data, the TI mixing model suggests the presence of dust and rock only. This may indicate that a vertical layering scenario is present and demonstrates that sand deposition and ripple formation are not currently active.

In regions where surface temperatures did not allow for the use of emissivity data, brightness temperature provides a viable alternative. Both surface emissivity and brightness temperature modeling demonstrate methods to derive thermophysical differences in surface cover. However, roughness derived from spectral emissivity modeling provides greater leverage of the complete data and a more accurate rock abundance estimation.

Chapter 5 investigated Daedalia Planum Lava flows associated with Arsia Mons volcanism by implementing a horizontal mixing model with a vertical layering component. Individual lava flows south of Arsia Mons exhibit unusual thermophysical variation (Ramsey and Crown, 2010; Crown and Ramsey, 2017; Simurda et al., 2019), with some flows displaying typical diurnal temperature changes and others showing no degree of variation. This has led to the conclusion that these flows exhibit exposed lava outcrops inundated by sand with a variable dust mantle up to ~0.2mm in thickness (Crown and Ramsey, 2017; Simurda et al., 2019; Simurda, 2019). Geologic mapping constrains the flow ages to ~100 My (Crown et al. 2015, 2017). Building upon these interpretations, we utilize THEMIS ROTO data collected at nadir and 25° off-nadir to investigate negatively sloped TIR emission spectra from visibly rough and smooth lava flows. Using a thermophysical model, I quantify the areal abundance of horizontally mixed rock, sand, and dust.

In addition, investigation reveals the presence of vertical layering combined with horizontal mixing of surface units. Model results indicate that the visibly rough flow best matches a horizontal mixture of 60% dust and 40% rock mantled by a vertical layer of dust ~0.4 mm thick (Figure 48). In contrast, the smooth flow best matches a model fit containing a horizontal mixture of 10% rock and 90% dust without a vertically layered dust mantle or a horizontal mix of 40% rock and 60% dust layered by a vertical 0.7mm thick (Figure 48). This flow (Flow 2) appears visibly smooth in HiRISE image data with much less visible lava outcropping than the visibly rough flow (Flow 1). This provides credence to the results of the vertical layering model (Figure 41).

Thermophysical modeling of the channelized flow reveals a central channel with a 50/50 ratio of rock and dust overlain by 0.7 mm of dust (Figure 49). CTX image data supports these findings and shows a smooth surface with some visible rock outcropping (Figure 47). The levees of this channel best match a model fit containing 40% rock and 60% dust with a 0.4mm vertical dust mantle (Figure 49). This model suggests a more significant amount of rock outcropping in the central channel than the levee, which is not supported by the visible data. At the late time of the ROTO overpass, vertical layers of dust greater than 0.7mm thick produced little change in the slope of the TIR spectrum. The model fit presented here was chosen as it contained the closest brightness temperature and spectral slope to the measured data. Rock percentages lower than 50% resulted in brightness temperatures colder than the measured values. A similar result is seen where the model contained sand instead of rock. Two potential explanations exist for this. The central channel structure may contain smoother lava flows (more akin to terrestrial pahoehoe) mantled by thick dust.

In contrast, the levees contain blockier flows that create a more significant vertical relief and a reduction in dust mantling. This explains the visibly "smooth" central channel observed in CTX image data and the more significant rock content suggested by the model. The second possibility is that the "rocky" channel material has a TI greater than sand (214 TIU) but lower than rock (1200 TIU), which suggests the presence of a more vesicular material or even a regolith-like material within the central channel that is below the detection limit of CTX. These implications are two-fold: smoother lava flow morphologies imply specific rheological properties, most notably a range of values for flow viscosity, gas contents, and crystal fraction that provide insights into eruptive conditions. Secondly, the potential presence of regolith speaks to the surface processes active post-flow deposition. Regolith production can be facilitated by both mechanical and chemical erosion of the crustal rocks. The rate of regolith production is a function of the time-averaged rates of erosional processes, surface age, duration of exposure, and geologic characteristics of the unit. As these flow ages have been constrained to the last 100 My (Crown and Ramsey, 2017), insights into the current regolith, dust, and rock abundances provide constraints on local surface processes and overall surface evolution

These scenarios highlight the weakness of a two-endmember model. Subpixel mixtures of materials can result in surface complexity, complicating the interpretation of TI data acquired from orbital instruments. This is particularly the case where low temporal data are used or if factors such as shadowing play a role in surface temperatures. The reduction of spectral slopes in the daytime TIR data suggests that shadowing caused where rough surfaces are viewed at high solar incidence angles impacts surface temperatures. This is the case in the visibly rough Arsia Mons lava flows and therefore needs to be accounted for where utilizing surface temperature to interpret surface characteristics.

Dust mantling provides another challenge in interpreting TIR emission spectra. The mantling of dust on the Martian surface is likely noncontiguous despite the similar age of lava flows. Rougher surfaces may provide low-lying regions (i.e., between blocks) that provide sheltered traps for dust and limit its removal by aeolian processes. Where dust thickness is below the remote sensing instrument's optical penetration depth, the underlying surface's spectral features are present in the emission spectra. This is observed at the visibly rough flow (flow 1) and the levee at Daedalia Planum. Linear deconvolution may allow the removal of the dust signature from the composite emission spectrum providing a means to target the underlying flow. Chapter 5 provides the groundwork for this by identifying specific flows and flow regions where the underlying lava signature might be extracted.

The work presented here demonstrates a multifaceted approach to investigating sub-meter thermophysical properties on Mars. Comprehensive spectral analysis, combined with high-resolution surface topographic characterization, allows for an intimate investigation of surface characteristics and their interaction with emitted energy. Furthermore, by combining TIR spectral slope analysis with thermophysical modeling and high-resolution image data, planetary surfaces can be characterized on a scale previously achievable only through in-situ investigation. These methods have applications to a wide number of planetary bodies furthering exploration across our solar system.

Appendix A Surface Roughness Analysis MATLAB code

```
%% create Average Heights and RMS plots like Figure 3 & 4
z=smoffnadir;  %%input dataset
z=table2array(z).

z=changem(z,[44.83],[-9999]); %%remove any holes in data

%%
PixelWidth=.0001; %%set window size
[n,m] = size(z);
x = linspace(0,(m-1) * PixelWidth , m);
y = linspace(0,(n-1) * PixelWidth , n);
[X,Y] = meshgrid(x,y);
z=z-44.83; %%subtract mean surface height
zx=detrend(z);
%%

figure1 = figure('WindowState','maximized');
axes1=axes('Parent',figure1);
hold(axes1,'on');

%create mesh
mesh1=mesh(X,Y,zx,'Parent',axes1);

xlim([0.03 .64]);
 ylim([0.1 .7]);

 % Create ylabel
ylabel('Sample Width (cm)','FontSize',24,'Rotation',-22);

% Create xlabel
xlabel('Sample Length (cm)','FontSize',24,'Rotation',12);
set(axes1,'FontSize',24)
view(axes1,[-35 54]);
grid (axes1,'on');
hold (axes1,'off');

c=colorbar
colormap Parula
title('Elevation (\mum)','Fontsize',32);
c.Label.String = 'Elevation (\mum)';
c.FontSize=(24)

%%
 abz=abs(zx);
```

```
q=movmean(abz,3,1);
g=movmean(abz,3,2);


zx2=(q+g)/2;
subplot2 = subplot(2,2,2);

figure2 = figure('WindowState','maximized');
axes2=axes('Parent',figure2);
hold(axes2,'on');

mesh2=mesh(X,Y,zx2);
imagesc(x,y,zx2); axis xy;

xlim([0.03 .64]);
 ylim([0.1 .7]);


  % Create ylabel
ylabel('Sample Width (cm)','FontSize',16);

% Create xlabel
xlabel('Sample Length (cm)','FontSize',16);
% Create colorbar
c=colorbar
colormap (flipud(parula(200)))
c.Label.String = 'Average height (\mum)';
title('Average Surface Topography','Fontsize',24);
c.FontSize=(16)

% Create textbox
annotation(figure2,'textbox',...
    [0.754515625 0.0162037037037032 0.1224375 0.061],...
    'String',{'* Note: Average heights limited to a maximum of 25 \mum to highlight small scale topography'},...
    'FitBoxToText','off');


w = sqrt(movmean(abz.^2,3,1));
R = sqrt(movmean(abz.^2,3,2));

H=(w+R)/2;

figure3 = figure('WindowState','maximized');
axes3=axes('Parent',figure3);
hold(axes3,'on');


mesh3=mesh(X,Y,H)
```

```
imagesc(x,y,H); axis xy;

% Create mesh
xlim([0.03 .64]);
 ylim([0.1 .7]);

  % Create ylabel
ylabel('Sample Width (cm)','FontSize',16);

% Create xlabel
xlabel('Sample Length (cm)','FontSize',16);
% Create colorbar
c=colorbar
colormap (flipud(parula(200)))
caxis([0 300])
c.Label.String = 'Average height (\mum)';
title('RMS of Surface Topography','Fontsize',24);
c.FontSize=(16)
c.Limits=([2 300]);
```

Appendix B Endmembers Used in TES atmospheric correction

Table 18. These are endmembers used in the TES atmospheric correction.

ASU ID	***Mineral Name***
55	Quartz BUR-4120
5	Albite WAR-0244
22	Oligoclase WAR-0234
1	Andesine BUR-240
63	Labradorite WAR-4524
177	Bytownite WAR-1384
178	Anorthite BUR-340
28	Actinolite HS-116.4B
30	Enstatite HS-9.4B
6	Bronzite BUR-1920
36	Diopside BUR-1820
164	Augite DSM-AUG01

147	Augite NMNH-119197
145	Hedenbergite manganoan DSM-HED01
8	Forsterite BUR-3720A
38	Forsterite AZ-01
167	Fayalite WAR-RGFAY01
KI 3115	Fo68 Olivine
KI 3362	Fo60 Olivine
KI 3373	Fo35 Olivine
KI 3008	Fo10 Olivine
25	Biotite BUR-840
29	Phlogopite HS-23.3B
	K-rich Glass
14	Serpentine HS-8.4B
211	Illite granular IMt-2 - 60% blackbody
193	Hectorite solid SCHa-1

197	Ca-montmorillonite solid STx-1
50	Hematite BUR-2600
119	Calcite C40
110	Dolomite C20
81	Anhydrite ML-S9
82	Gypsum ML-S6
	Average high albedo surface
	Average low albedo surface

Appendix C Custom Davinci Code

Appendix C.1.1 Create slope and azimuth table to predict surface temperatures

```
#!/mars/common/bin/davinci -fq -v0
#run the process input on sourcing
oldverbose=verbose
verbose=0
krc_master=krc_process_input($DV_KRC_HOME+"/run/master.inp",usage=1)
global(krc_master)
verbose=oldverbose
```

##creates an array with the proper size. This should be formatted to the user in the format "out=create(j,k,1,format=float)".

##In this example there would be 46 x 37 combinations of k since j will have 46 values from 0-90 n steps of 2 and k will have 37 values from 0 to 360 in steps of 10.

```
out=create(46,37,1,format=double)
out[]=0
##counter for array
i = 0;
jj=1
kk=1
if($ARGC == 0) {
  ##iterates over possible j values
  for(j = 0; j <= 90; j+=2)  {
    ##iterates over possible k values
    for (k = 0; k <= 360; k+=10) {
      printf("Output Coordinates: %i %i \n",jj,kk)

            ##calls KRC and stores values in array
      outtmp = krc(lat=18.4873, lon=77.54395, INERTIA=190.0, hour=18.7, ls=80, SLOPE=j, SLOAZI=k);
      out[jj,kk,]=outtmp.tsurf
      #i++; ##adds one to array counter
      i=i+1
 kk=kk+1
      write(outtmp.tsurf,"krc_loop_output_tmp.csv",csv,force=1)   ##outputs average temperature of all possible combinations
    }
    jj=jj+1
    kk=1
  }
write(out,"krc_loop_output.csv",csv,force=1)  ##outputs table at each slope/azimuth combination
}
```

Appendix C.1.2 KRC Vertical mixture model

```
nadir=read("nadir") ## read in data

r4mm=   krc(lat=-23.273,   lon=237.233,   INERTIA=50,INERTIA2=2500,thick=0.0004,hour=17.950052,ls=357.93)
##runs KRC with desired input parameters

dust= krc(lat=-23.273, lon=237.233, INERTIA=50,ls=355.85162)  ##input 100% dust endmember
rock= krc(lat=-23.273, lon=237.233, INERTIA=2500,ls=355.85162)  ##input 100% rock endmember
dust4mm=bbrw(wv,214.4004) ##use KRC output temperature from model to derive blackbody curve

r1d=dust4mm*.1
r2d=dust4mm*.2
r3d=dust4mm*.3
r4d=dust4mm*.4    ##creates library with relative abundances vertical mixture
r5d=dust4mm*.5
r6d=dust4mm*.6
r7d=dust4mm*.7
r8d=dust4mm*.8
r9d=dust4mm*.9
rock_dust4mm={r10=r1d,r20=r2d,r30=r2d,r40=r4d,r50=r5d,r60=r6d,r70=r7d,r80=r8d,r90=r9d}


d60r40=dust.d60+r4d ##create radiance mixtures based on user defined inputs, in this case 60% dust + rock with dust
layer 0.4mm thick


md60r40=thm.themis_emissivity(d60r40,b1=3,b2=3,max_emiss=0.993) ##convert to emissivity
pplot({flow1[,,2:9],md60r40.emiss[,,2:9]},xaxis=thm_full[,2:9,],themis=1,emiss=1,wave=1,
ylabel="Emissivity",linespoints=3) ##plot desired data
```

Bibliography

Ahern, A. A., Rogers, A. D., Edwards, C. S., & Piqueux, S. (2021). Thermophysical properties and surface heterogeneity of landing sites on Mars from overlapping Thermal Emission Imaging System (THEMIS) observations. Journal of Geophysical Research: Planets, 126(6), e2020JE006713.

Armstrong, J. C., Titus, T. N., & Kieffer, H. H. (2005). Evidence for subsurface water ice in Korolev crater, Mars. Icarus, 174(2), 360-372.

Aufaristama, M., Höskuldsson, Á., Ulfarsson, M. O., Jónsdóttir, I., & Thordarson, T. (2020). Lava Flow Roughness on the 2014–2015 Lava Flow-Field at Holuhraun, Iceland, Derived from Airborne LiDAR, and Photogrammetry. Geosciences, 10(4), 125.

Bandfield, J.L., (2009), Effects of Surface Roughness and Graybody Emissivity on Martian Thermal Infrared Spectra, Icarus, 202,414-428, https://doi.org/10.1016/j.icarus.2009.03.031.

Bandfield, J. L. (2006). Extended surface exposures of granitoid compositions in Syrtis Major, Mars. Geophysical research letters, 33(6).

Bandfield, J. L. (2008). High-silica deposits of an aqueous origin in western Hellas Basin, Mars. Geophysical Research Letters, 35(12).

Bandfield, J.L., & C.S. Edwards, (2008). Derivation of Martian surface slope characteristics from directional thermal infrared radiometry, Icarus, 10.1016/j.icarus.2007.08.028.

Bandfield, J. L., & Feldman, W. C. (2008). Martian high latitude permafrost depth and surface cover thermal inertia distributions. Journal of Geophysical Research: Planets, 113(E8).

Bandfield, J. L., & Rogers, A.D., (2020). Thermal infrared spectral modeling, In: J. Bishop, J. Moersch, and J. F. Bell III (Eds.) Remote Compositional Analysis, Cambridge University Press, Cambridge, 10.1017/9781316888872.

Bandfield, J. L., & Smith, M. D. (2003). Multiple emission angle surface–atmosphere separations of Thermal Emission Spectrometer data. Icarus, 161(1), 47-65.

Bandfield, J. L., Christensen, P. R., & Smith, M. D. (2000). Spectral data set factor analysis and end-member recovery: Application to analysis of Martian atmospheric particulates. Journal of Geophysical Research: Planets, 105(E4), 9573-9587.

Bandfield, J.L., P.O. Hayne, J.-P. Williams, B.T. Greenhagen, D.A. Paige, (2015). Lunar surface roughness derived from LRO Diviner Radiometer observations, Icarus, 10.1016/j.icarus.2014.11.009.

Bandfield, J. L., Rogers, D., Smith, M. D., and Christensen, P. R. (2004). Atmospheric correction and surface spectral unit mapping using Thermal Emission Imaging System data, Journal of Geophysical Research, 109, E10008, doi:10.1029/2004JE002289.

Beddingfield, Chloe B., Jeffrey E. Moersch, and Harry Y. McSween Jr. "Investigating crater rim thermal inertia variations on Mars: A case study in Tisia Valles." Icarus 314 (2018): 345-363.

Beddingfield, Chloe B., Jeffrey E. Moersch, and Harry Y. McSween Jr. "The relationship between thermal inertia and degradation state of craters in areas of low surface dust cover on Mars." Icarus 370 (2021): 114678.

Bradley, B. A., Sakimoto, S. E., Frey, H., & Zimbelman, J. R. (2002). Medusae Fossae Formation: New perspectives from Mars Global Surveyor. Journal of Geophysical Research: Planets, 107(E8), 2-1.

Burr, D.M., Enga, M.-T., Williams, R.M.E., Zimbelman, J.R., Howard, A.D., Brennand, T.A (2009). Pervasive aqueous paleoflow features in the Aeolis/Zephyria Plana region, Mars, Icarus, 200(1), 52-76

Campbell, B. A., & Shepard, M. K. (1996). Lava flow surface roughness and depolarized radar scattering. Journal of Geophysical Research: Planets, 101(E8), 18941-18951.

Carter, A.J., Ramsey, M.S., Durant, A.J., Skilling, I.P., Wolfe, A.L., (2009) Micron-scale roughness of volcanic surfaces from thermal infrared spectroscopy and scanning electron microscopy, Journal of Geophysical Research, 114, B02213, doi:10.1029/2008JB005632.

Christensen, P. R. (1986), The spatial distribution of rocks on Mars, Icarus, 68, 217– 238, doi:10.1016/0019-1035(86)90020-5.

Christensen, P. R., Jakosky, B. M., Kieffer, H. H., Malin, M. C., McSween, H. Y., Nealson, K., ... & Ravine, M. (2004). The thermal emission imaging system (THEMIS) for the Mars 2001 Odyssey Mission. Space Science Reviews, 110(1), 85-130.

Chuang, F. C., Crown, D. A., & Berman, D. C. (2019). Geology of the northeastern flank of Apollinaris Mons, Mars: Constraints on the erosional history from morphology, topography, and crater populations. Icarus, 333, 385-403.

Cowart, J. C., & Rogers, A. D. (2021). Investigating Sources of Spectral Olivine Enrichments in Martian Bedrock Plains Using Diurnal Emissivity Changes in THEMIS Multispectral Images. Journal of Geophysical Research: Planets, 126(11), e2021JE006947.

Crown, D. A., & Ramsey, M. S. (2017). Morphologic and thermophysical characteristics of lava flows southwest of Arsia Mons, Mars. Journal of volcanology and geothermal research, 342, 13-28.

Davidsson, B. J., Rickman, H., Bandfield, J. L., Groussin, O., Gutiérrez, P. J., Wilska, M., ... & Mueller, T. G. (2015). Interpretation of thermal emission. I. The effect of roughness for spatially resolved atmosphereless bodies. Icarus, 252, 1-21.

Edwards, C. S., Bandfield, J. L., Christensen, P. R., & Fergason, R. L. (2009). Global distribution of bedrock exposures on Mars using THEMIS high-resolution thermal inertia. Journal of Geophysical Research-Planets, 114, 18. E11001, doi: 10.1029/2009je003363

Ewing, R. C., Lapotre, M. G. A., Lewis, K. W., Day, M., Stein, N., Rubin, D. M., ... & Fischer, W. W. (2017). Sedimentary processes of the Bagnold Dunes: Implications for the eolian rock record of Mars. Journal of Geophysical Research: Planets, 122(12), 2544-2573.

Fergason, R.L., (2014) Thermal Inertia Mosaic Quantitative Map from 30S to 240E, USGS Astrogeology Science Center.

Fergason, R. L., P. R. Christensen, and H. H. Kieffer (2006a), High-resolution thermal inertia derived from the Thermal Emission Imaging System (THEMIS): Thermal model and applications, Journal of Geophysical Reseach, 111, E12004, doi:10.1029/2006JE002735.

Fergason, R. L., Christensen, P. R., Bell III, J. F., Golombek, M. P., Herkenhoff, K. E., & Kieffer, H. H. (2006b). Physical properties of the Mars Exploration Rover landing sites as inferred from Mini-TES–derived thermal inertia. Journal of Geophysical Research: Planets, 111(E2).

Gillespie, A. R., A. B. Kahle, and R. E. Walker (1986), Color enhancement of highly correlated images: I. Decorrelation and HIS contrast stretches, Remote Sensing of the Environment, 20, 209– 235.

Howard, A. D. (1981). Etched plains and braided ridges of the south polar region of Mars: Features produced by basal melting of ground ice? Reports of Planetary Geology Program, 286-288.

Hynek, B. M., Phillips, R. J., & Arvidson, R. E. (2003). Explosive volcanism in the Tharsis region: Global evidence in the Martian geologic record. Journal of Geophysical Research: Planets, 108(E9).

Jakosky, B. M., Finiol, G. W., & Henderson, B. G. (1990). Directional variations in thermal emission from geologic surfaces. Geophysical Research Letters, 17(7), 985-988.

Jones, E., Caprarelli, G., and Osinski, G. R. (2016), Insights into complex layered ejecta emplacement and subsurface stratigraphy in Chryse Planitia, Mars, through an analysis of

THEMIS brightness temperature data, Journal of Geophysical Research: Planets, 121, 986– 1015, doi:10.1002/2015JE004879.

Kerber, L., & Head, J. W. (2010). The age of the Medusae Fossae Formation: Evidence of Hesperian emplacement from crater morphology, stratigraphy, and ancient lava contacts. Icarus, 206(2), 669-684.

Kieffer, H. H. (2013). Thermal model for analysis of Mars infrared mapping. Journal of Geophysical Research: Planets, 118(3), 451-470.

Kieffer, H. H., Martin, T. Z., Peterfreund, A. R., Jakosky, B. M., Miner, E. D., and Palluconi, F. D. (1977), Thermal and albedo mapping of Mars during the Viking primary mission, Journal of Geophysical Research, 82 (28), 4249– 4291, doi:10.1029/JS082i028p04249.

Kieffer, H. H., Christensen, P. R., & Titus, T. N. (2006). CO 2 jets formed by sublimation beneath translucent slab ice in Mars' seasonal south polar ice cap. Nature, 442(7104), 793-796.

King, P. L., P. F. McMillan, and G. M. Moore (2004), Infrared spectroscopy of silicate glasses with application to natural systems, in Infrared Spectroscopy in Geochemistry, Exploration Geochemistry, and Remote Sensing, Mineral. Assoc. of Can. Short Course Ser., vol. 33, edited by P. L. King, M. S. Ramsey, and G. A. Swayze, pp. 93–133, Mineral. Assoc. of Can., Ottawa.

Logan, L. M., Hunt, G. R., Salisbury, J. W., & Balsamo, S. R. (1973). Compositional implications of Christiansen frequency maximums for infrared remote sensing applications. Journal of Geophysical Research, 78(23), 4983-5003.

Lane, M. D., & Christensen, P. R. (1998). Thermal infrared emission spectroscopy of salt minerals predicted for Mars. Icarus, 135(2), 528-536.

Mandt, K. E., de Silva, S. L., Zimbelman, J. R., & Crown, D. A. (2008). Origin of the Medusae Fossae Formation, Mars: Insights from a synoptic approach. Journal of Geophysical Research: Planets, 113(E12).

McEwen, A. S., Eliason, E. M., Bergstrom, J. W., Bridges, N. T., Hansen, C. J., Delamere, W. A., ... & Weitz, C. M. (2007). Mars reconnaissance orbiter's high resolution imaging science experiment (HiRISE). Journal of Geophysical Research: Planets, 112(E5).

McKeeby, B.E. and Ramsey, M.S., (2020) Spectral anisothermality: A two-look approach to thermal infrared data analysis of planetary basaltic surfaces, 51st Lunar Planetary Science Conference, abs. #2083.

McKeeby, B.E., and Ramsey, M.S., (2021) Deriving planetary surface roughness: Combining digital photogrammetry and thermal infrared spectroscopy. 52nd Lunar Planetary Science Conference, abs. #1957.

Mellon, M.T., Jakosky, B.M., Kieffer, H.H., Christensen, P.R., (2000) High-Resolution Thermal Inertia Mapping from the Mars Global Surveyor Thermal Emission Spectrometer, Icarus, 148 (2), 437-455, https://doi.org/10.1006/icar.2000.6503.

Mellon, M. T., and N. E. Putzig. "The apparent thermal inertia of layered surfaces on Mars." Lunar and planetary science conference. No. 1338. 2007.

Mustard, J. F., and T. D. Glotch (2019), Theory of Reflectance and Emittance Spectroscopy of Geologic Materials in the Visible and Infrared Regions, In: J. Bishop, J. Moersch, and J. F. Bell III (Eds.) Remote Compositional Analysis, p21-41, Cambridge University Press, Cambridge, doi:10.1017/9781316888872.004.

Palluconi, F.D., & Kieffer, H.H. (1981). Thermal Inertia Mapping of Mars from 60 deg S to 60 deg N, Icarus, 45, 415-426.

Putzig, N.E., Mellon, M.T., Kretke, K.A., Arvidson, R.E., (2005) Global Thermal Inertia and Surface Properties of Mars from the MGS mapping Mission, Icarus, 173 (2), 325-341.

Ramsey, M.S., and Fink, J.H., (1999) Estimating silicic lava vesicularity with thermal remote sensing: A new technique for volcanic mapping and monitoring, Bulletin of Volcanology, 61, 32-39.

Rose, S.R., Watson, W., Ramsey, M.S., Hughes, C.G., (2014) Thermal Deconvolution: Accurate retrieval of Multispectral Infrared Emissivity from Thermally Mixed Volcanic Surfaces, Remote Sensing of the Environment, 140, pp 690-703. https://doi.org/10.1016/j.rse.2013.10.009.

Ruff, S. W., Christensen, P. R., Barbera, P. W., & Anderson, D. L. (1997). Quantitative thermal emission spectroscopy of minerals: A laboratory technique for measurement and calibration. Journal of Geophysical Research: Solid Earth, 102(B7), 14899-14913.

Sanchez-Vahamonde, C. R., & Neish, C. (2021). The Surface Texture of Martian Lava Flows as Inferred from Their Decimeter-and Meter-scale Roughness. The Planetary Science Journal, 2(1), 15.

Scott, D. H., & Tanaka, K. L. (1986). Geologic map of the western equatorial region of Mars.

Shepard, M. K., Campbell, B. A., Bulmer, M. H., Farr, T. G., Gaddis, L. R., & Plaut, J. J. (2001). The roughness of natural terrain: A planetary and remote sensing perspective. Journal of Geophysical Research: Planets, 106(E12), 32777-32795.

Simurda, C. M., Ramsey, M. S., & Crown, D. A. (2019). The unusual thermophysical and surface properties of the Daedalia Planum lava flows. Journal of Geophysical Research: Planets, 124(7), 1945-1959.

Smith, M. D., Bandfield, J. L., & Christensen, P. R. (2000). Separation of atmospheric and surface spectral features in Mars Global Surveyor Thermal Emission Spectrometer (TES) spectra. Journal of Geophysical Research: Planets, 105(E4), 9589-9607.

Smith, M. D., J. L. Bandfield, P. R. Christensen, and M. I. Richardson (2003), Thermal Emission Imaging System (THEMIS) infrared observations of atmospheric dust and water ice cloud optical depth, Journal of Geophysical Research, 108(E11), 5115, doi:10.1029/2003JE002115.

Tanaka, K. L. (2000). Dust and ice deposition in the Martian geologic record. Icarus, 144(2), 254-266.

Titus, T. N., Kieffer, H. H., & Christensen, P. R. (2003). Exposed water ice discovered near the south pole of Mars. Science, 299(5609), 1048-1051.

Voigt J.R.C., Hamilton C.W., (2021a). Facies map for the 2014–2015 Holuhraun eruption in Iceland. In: University of Arizona, Department of Planetary Sciences, Lunar and Planetary Laboratory. https://doi.org/10.25422/azu.data.12971129.v3

Voigt, J. R., Hamilton, C. W., Steinbrügge, G., & Scheidt, S. P. (2021b). Surface roughness characterization of the 2014–2015 Holuhraun lava flow-field in Iceland: implications for facies mapping and remote sensing. Bulletin of Volcanology, 83(12), 1-14.

Whelley P.L., Garry W.B., Hamilton C.W., Bleacher J.E. (2017), LiDAR-derived surface roughness signatures of basaltic lava types at the Muliwai a Pele Lava Channel, Mauna Ulu, Hawai'i. Bulletin of Volcanology, 79(11):75

Whelley P.L., Glaze L.S., Calder E.S., Harding D.J. (2014), LiDAR-derived surface roughness texture mapping: application to Mount St. Helens Pumice plain deposit analysis. IEEE Transactions Geoscience Remote Sensing, 52(1):426–438

Whitney, M. I. (1985). Yardangs. Journal of Geological Education, 33(2), 93-96.

Williams, R. M. E., & Edgett, K. S. (2005). Valleys in the Martian rock record. Lunar and Planetary Science 36, abs#1099.

Zimbelman, J. R., & Griffin, L. J. (2010). HiRISE images of yardangs and sinuous ridges in the lower member of the Medusae Fossae Formation, Mars. Icarus, 205(1), 198-210.

Zimbelman, J.R., and Scheidt, S.P., (2018). Geologic maps of Mars quadrangles MC-23 NW and MC-16 NW. Scientific Investigations Map, scale 1:2M, U.S. Geological Survey.